Study of soft magnetic thin films and patterned devices with MOKE imaging technique

Doctor of Philosophy

Xiangyu Zheng

University of York

Electronics Engineering Department

April 2021

Abstract

While the conventional microelectronic integrated circuits based on the electron charge are approaching the theoretical limitation in foreseeable future, next generation nonvolatile logic units based on electron spin have potential to build logic networks of low-power consumption. Central to this work is to investigate the magnetic properties of soft magnetic materials and develop a method for in-memory computing based on patterned soft magnetic materials logic units.

The mainly result were carried out by Magneto-optical Kerr effect (MOKE) microscopy. By inverting the growth order, the amount of defects can be artificially tuned, and skyrmions are shown to be preferentially formed in samples with more defects. The stable region and the density of the skyrmions can be efficiently controlled in the return magnetization loops by utilizing first-order reversal curves (FORCs). The major contribution of these findings establish a general internal link from sample preparation to skyrmion generation and provides a general method for controlling skyrmion density. Next, the temperature-dependent magnetic properties of MgO/CoFeB/Ta thin films have been investigated. The perpendicular magnetic anisotropy (PMA) gradient in MgO/CoFeB/Ta thin films via the temperature gradient generation sample stage has been studied. This study provides a new easy method to create PMA gradient that will contribute to the simplification of field-free spintronic devices. Eventually, Y-shaped NiFe nanowire has been investigated. The quasi-static micromagnetic simulations correspond to the experimental results and reveal the principle of device operations. The use of programmable logic units and potential applications for in-memory computing have been further extended based on this nanostructure. The major contribution of this part proposes a feasible paradigm for in-memory computing programmable logic gate, which can significantly reduce the complexity of conventional logic circuits. The results conclusion and discussion for the future works are proposed in the final chapter.

List of Contents

List of Figures

Chapter 1

List of Tables

Chapter 2

List of Publications

1. Xiangyu Zheng, Junlin Wang, Guanqi Li, Xianyang Lu, Wenjia Li, Yichuan Wang, Li Chen, Haihong Yin, Jing Wu, and Yongbing Xu. "Paradigm of Magnetic Domain Wall-Based In-Memory Computing." *ACS Applied Electronic Materials* (2020).
2. Haihong Yin, Xiangyu Zheng, Junlin Wang, Yu Zhou, Balati Kuerbanjiang, Guanqi Li, Xianyang Lu et al. "Defect-Correlated Skyrmions and Controllable Generation in Perpendicularly Magnetized CoFeB Ultrathin Films." *Applied Physics Letters* 119, 062402 (2021).
3. Wang, J., Xia, J., Zhang, X., Zheng, X., Li, G., Chen, L., ... & Xu, Y. (2020). Magnetic skyrmionium diode with a magnetic anisotropy voltage gating. Applied Physics Letters, 117(20), 202401.
4. Li, G., Zheng, X., Wang, J., Lu, X., Wu, J., Cai, J., ... & Xu, Y. (2020). Timescales and contribution of heating and helicity effect in helicity-dependent all-optical switching. *Phys. Rev. B*, under review. arXiv preprint arXiv:2009.12816. First co-author.
5. Yu Yan, Xianyang Lu, Bo Liu, Xiaoqian Zhang, Xiangyu Zheng, Hao Meng, Wenqing Liu et al. "Element-specific spin and orbital moments and perpendicular magnetic anisotropy in Ta/CoFeB/MgO structures." *Journal of Applied Physics* 127, no. 6 (2020): 063903.

Acknowledgements

First of all, I would like to express my sincere gratitude to my supervisor Prof. Yongbing Xu. His professional guidance and continues encouragement paved a way for my Ph.D. research.

With many thanks to my second supervisor Dr. Jing Wu for her guidance during this research. And I'm grateful to my colleague Dr. Junlin Wang for his mircomagneic simulation results in this work. I'm also grateful to Mr. Guanqi Li, visiting scientist Prof. Haihong Yin, Mr. Wenjia Li, Mr. Xianyang Lu, Mr. Yichuan Wang, Mr. Yu Yan and Mr. Kunpeng Zhang for their help during my research.

I would like to thank Dr. Iain Will and Mr. Charan Panesar for their kindly help and training with various equipment and facilities in the clean room. I would also like to thank the collaborators Dr. Balati Kuerbanjiang and Prof. Vlado K. Lazarov who's complete the STEM measurement in this work. I'd also like to thank Dr. Kelvin Elphick for his help in MFM measurements and VSM training.

I would like to thank Dr. Li Chen for his top quality of fabrication nanostructure. And I'm grateful to the collaborators Mr. Yu Zhou and Prof. Jianwang Cai for their training for magnetron sputtering and help in samples preparing.

Finally, I would like to say special thanks to my parents for their encouragement and financial support. And I'm deeply grateful to my wife Wei Zhang for her love, support and understanding during my whole Ph.D. research.

Xiangyu Zheng
York, UK
28 April 2021

Declaration

I declare that this thesis is a presentation of original work and I am the sole author. This work has not previously been presented for an award at this, or any other, University. All sources are acknowledged as References.

Where the thesis is based on work done by myself jointly with others, I have made clear exactly what was done by others and what I have contributed myself.

Part 1 Literature review

Chapter 1-Introduction

1.1 Overview of Spintronics

Electron spin is a quantum property of electrons. Like charge and rest mass, spin is a fundamental, unvarying property of the electron. While the conventional microelectronic integrated circuits (ICs) based on complementary metal-oxide-semiconductor (CMOS) which use of the charge property of the electron are experiencing its bottleneck. The number of transistors on the Si-based processors doubles every two years, though the cost of computers is halved, a trend known as Moore's law. This law foresaw the rapid development of semiconductors and also declared the limits of semiconductors. On contrast, Spintronics, which has a high potential to work alongside with CMOS in heterogeneous system, is rapidly evolving due to various breakthroughs in the study of spin quantum phenomena as well as huge industry demand in the last a few decades[1]. The commercialized spintronic devices, such as magnetic recording, magnetic sensor, nonvolatile memories are proving very useful in real-world applications.

The milestone discovery in the field of spintronics, giant magnetoresistance (GMR) was first observed in metallic multilayers (001)Fe/(001)Cr[2]. This spin-dependent electron transport technique makes the high-density hard disk drive (HDD) into our daily lives and deeply affect our world. GMR-based spin valves and magnetic tunnel junctions (MTJs) have been used for large-scale commercial applications, such as magnetic read heads, sensors and biomedical devices. Another breakthrough in spintronics was the discovery of tunnel magnetoresistance (TMR). This effect was realized and studied recently at room temperature[3, 4], although it was discovered earlier than the GMR effect[5, 6].

1.2 Advancement in Spintronics

1.2.1 Magnetoresistive Random Access Memory (MRAM)

CMOS is currently the dominating technology for logic circuits, allowing for fast and powerful microprocessors [7]. However, it is quickly approaching its scaling limits due

to increased problems with power dissipation at scaled technology nodes. In this context, the next-generation memory device is required allowing for continued scaling with improved energy efficiency by eliminating static power dissipation. The integration of a fast, energy-efficient non-volatile memory technology with CMOS can help alleviate this problem [8].

The most important three kinds of memories in the memory hierarchy are static random-access memories (SRAM), dynamic random-access memories (DRAM) and NOR Flash. SRAM, though it's the fastest among three device, it's volatile with a very low density. DRAM has a higher density compared with SRAM, but it is also volatile and needs periodic refresh, which results in power consumption. The NOR flash memories have the highest density in these memories and are non-volatile. However, the quite slow write speed and the problem of endurance limited it applications.

Spintronic devices, which exploit the exchange interaction of the electron spins, where magnetic and transport properties are coupled, are strong candidates for non-volatile memory due to the inherent hysteresis in ferromagnetic materials, and the compatibility of some of these materials with the standard CMOS process [9-11]. Magnetoresistive RAM (MRAM) has exhibited significant advantages as a fast, fairly low-power, high-endurance, radiation-resistant non-volatile memory, which can be integrated into the CMOS as a back-end of line (BEOL) process [12]. The read-out process of the MRAM bits is reliably performed via the tunnelling magnetoresistance (TMR) effect [13, 14] in magnetic tunnel junctions (MTJs).

The concept for magnetic random-access memories technology which replacing the toroid of core memory with magnetoresistive elements can be traced back to 1960s[15]. After over half a century of exploration, the spin-transfer torque (STT) and spin–orbit torque (SOT) and giant tunnel magnetoresistance (TMR) in MgO-based MTJs were discovered and investigated by researchers one after another. All these outstanding discovery has led to the development of scalable nonvolatile magnetic random-access memories.

Generally speaking, the MRAM, which combing many advantages, will eventually become a dominant type of memory or potentially even becoming a universal memory in the future. Nowadays, many MRAM devices were mostly made from CoFeB which provide many useful advantages in magnetic memory.

The anisotropy of magnetic material are basic theory in significant applications of magnetic device, especially for memory and storage. A new idea of PMA spin-transfer-torque magnetic random access memories (STT-MRAM), which based on CoFeB/MgO out-of-plane MTJs, was reported in 2010 [16]. Comparing with in-plane anisotropy MTJ structure, perpendicular magnetic anisotropy MTJ usually requires less threshold current.

The first observation of TMR effect at room temperature in alumina based MTJs [3, 4], attracting many researcher dedicate to investigate the next generation memory based on the effect of TMR. In MRAM, the information is coded as parallel="0", antiparallel="1" based on orientation of magnetization. MTJ, which is called magnetic

tunnel junctions, is the storage unit. The different magnetoresistance can be read which imply different information. Figure 1.1 represent the history of the hierarchy of MRAM.

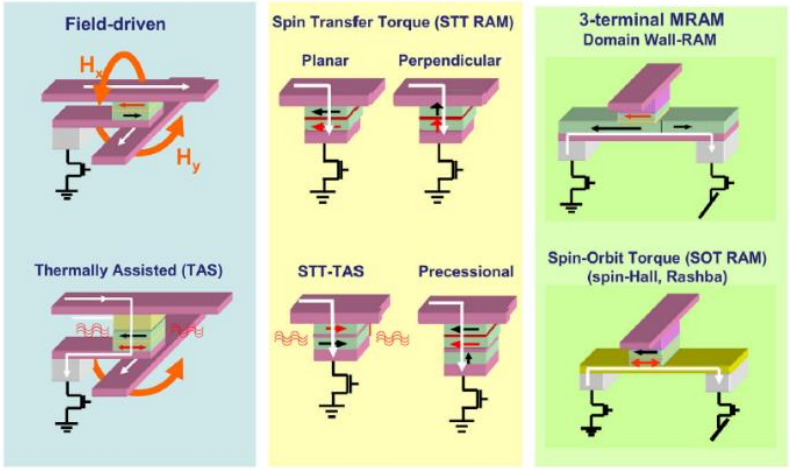

Figure 1.1 Various hierarchy of MRAM in the history of applications or research. Left hand picture shows the first MRAM utilized field writing. Center picture shows major design of STT-MRAM with in-plane and out-of-plane, thermal assistance (TAS) and orthogonal polarizers. Right hand picture exhibits 3-terminal MRAM and spin-orbit-torque (SOT) MRAM which use current induced domain wall motion. [17]

The first generations of MRAM utilized the Oersted fields generated by running currents in adjacent conducting lines of memory cells to switch the magnetization. However, the large current for generating a write field is around 10mA, which means the structure cannot be downscaled below 90nm technology node.

Thermal assistance (TAS) was proposed to solve this problem [18, 19]. In this technique, a pulse current is induced into MTJ which heat the storage layer for short time. This heating decrease the energy barrier letting magnetization switching more easily, which required lower magnetic fields than with toggle MRAM. However the limitation of this device is field generation in the word lines restricted by the electronmigration.

The discovery of STT switching was first reported in metallic Co/Cu/Co nanopillars in 2000 [13]. This new phenomena change the scientist' understanding of the MRAM. The magnetization can be switched not only by external magnetic field, but also by current. As shown in the center of figure 1.1, STT-RAM structure consists of a pinned (fixed) layer and a free layer that can have two states (parallel or antiparallel). The two layers are separated by a tunneling oxide layer, which is usually made for MgO or AlO [12, 20]. The writing process is performed by passing a spin-polarized current, which transfers some of its momentum crossing the insulation layer, inducing a torque that can result in switching depending on the direction of the current.

The most recently research of MRAM are based on Spin-orbit torque (SOT). According to the Spin Hall effect (SHE)[21], the spin polarized current generated in the heavy metal accumulate at the interface between the heavy metal (HM) layer and ferromagnetic material (FM) layer. The injected polarized current can reverse the magnetization of FM. This newest spintronic device has two independent read and write paths, which significantly improves the reliability of reading[22]. The required write current is much lower, and the write time is supposed to be much faster.

1.2.2 Skyrmions racetrack memory

Magnetic skyrmion are topologically protected chiral quasiparticles that exhibit the potential ability for transportation and storage of information. The size of skyrmion in many materials can scale down to a few nanometers, which can be used to make and design high density memory. This particle-like spin textures can be describe as counterpart of topologically protected electronic states. Recently, most advance research prove the probability of controlling nanoscale skyrmion, including creation, detection, manipulation and deletion. These research open a new field of spintronic devices, such as magnetic memories and logic gates. From material perspective, the skyrmion has been observed in many magnetic materials, such as ultrathin (a few nanometers) transition metal films and B20 materials.

The first observation of nanoskyrmion in ferromagnetic thin films at ultra-low temperature, which one monolayer hexagonal Fe film grow on one-atomic-layer thickness Ir(111) surface, proposed by Stefan Heinze in 2011[23]. By using the spin-polarized scanning tunneling microscopy (SPSTM), the clearly nano-skyrmion lattice is separated from the underlying atomic lattice. This kind of skyrmion is a much smaller magnetic unit only down to 1nm, which generated at ultra-low temperature without external applied magnetic field. Latterly, the skyrmion generated at room temperature has been discovered in various material system[24] [25, 26].

Since the generation and manipulation could be achieved by voltage or current, the spintronic devices of skyrmion-based with high density and more stable endurance have attracted researcher to investigate. The skyrmions memory device was subsequently designed which opens up a new branch of spintronics. Guoqiang Yu et al. [27] proposed a new design which may open the way for the SKS (skyrmions) non-volatile memory device. This new concept is represented in figure 1.2, which has the possibility to made for in-memory computing unit.

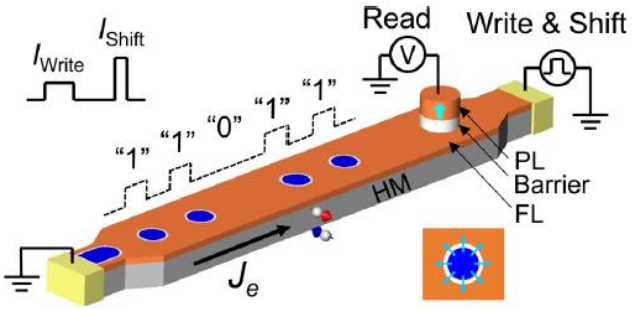

Figure 1.2 Schematic diagram of SKS memory device design. The blue circles represent the skyrmions in CoFeB layer. The left hand side electrode can generate skyrmion by current-induced SOT. The write and shift operating use different current magnitude[27].

Over the past few years, many properties of shyrmions have been studied and some functionalities proposed. Observing, writing, deleting, manipulating of single skyrmion have been realised[26, 27]. The skyrmion can be operated at room temperature and with low or even without external magnetic fields. However, the properties of the skyrmion dynamic motion, edge effect, impact of anisotropy in materials still need to be investigated, especially to progress the work on skyrmions towards real applications.

1.2.3 In-memory computing

Conventional microelectronic integrated circuits (ICs) based on complementary metal-oxide-semiconductor (CMOS) are experiencing its bottleneck. On contrast, Spintronics, which could replace CMOS or work alongside it in heterogeneous system, is rapidly evolving due to various breakthroughs in the study of spin quantum phenomena as well as huge industry demand in the last a few decades[1]. Motivated by this, a variety of concepts and spintronic devices have been proposed to overcome the limitation, knows as the memory wall, in which computation and storage are physically separated[28]. Instead of re-optimizing conventional integrated circuits, in-memory computing, which is a new revolutionary concept, aims to subvert the von Neumann architecture by *in-situ* calculations, where the data are located[29]. This new architecture, which has become the most attractive hot topic in the last decade, provides a straightforward advantage by totally eliminating the latency and energy burdens of memory wall[28]. Without any separation between the memory and computation, in-memory computing approach is very similar to the operation method of the human neurons networks[30].

Various in-memory computing schemes have been proposed in both analogue and digital spaces[28] and these new architectures require capability that can compute and store data at the same time. The emerging nonvolatile computational memory techniques, such as resistance switching RAM (RRAM)[31], phase change memory (PCM)[32], magnetoresistive RAM (MRAM)[33], and ferroelectric RAM

(FeRAM)[34], which have unique storage strategic rather than based on electronic charge, push the in-memory computing one step forward by reducing the 'distance' between computing and the data[35]. Digital computing by bipolar resistive switching[36] based on spintronic memory device offers several advantages over the nanomagnets[37] and quantum cellular automata [38-40] for in-memory digital computing. Analogue computing with crosspoint arrays is also applying computational memory technique such as RRAM[41] or PCM[42] to implement the in-memory computing. Another branch of in-memory computing is investigating a magnetic logic architecture, referred to as "domain-wall logic" (DWL), where data are encoded along the magnetic nanowires. The DWL based on soft magnetic material such as Permalloy (NiFe) has been investigated for decades which has a strong potential to replace present logic gate [43-46].

1.3 Aims of this PhD work

For development of hardware spintronic devices, this thesis is to provide the understanding of sample fabrication of skyrmion based device, perpendicular magnetic anisotropy gradient induced, and domain-wall logic based in-memory computing. Most of the works in this thesis were based on the MOKE imaging system, which has advantage of real-time domain structure observation.

Magnetron sputtering is one of the main methods for the preparation of coating, microelectronic devices processing via various materials. The multilayer of MTJs prepared by magnetron sputtering has become the mainstream method. The influence of magnetron sputtering on the growth order of soft magnetic multilayers has been reported, however, there is no relevant research on the effect of the growth order of soft magnetic multilayers on skyrmion. Therefore, the understanding of fabrication of skyrmion based device made by soft magnetic material is important. In this study, the relationship between the growth order of CoFeB based sample series and skyrmion generation has been studied by MOKE imaging system. We aim to provide a general method for sample preparation of favorable skyrmion generation. On the other hand, the density of skyrmion in soft magnetic material determines the storage capacity of the device. In this thesis, we aim to provide a general method to find an appropriate range of higher density of skyrmion under an external field.

In additional, the temperature is a key parameter which will impact the performance of electronic device. In spintronic device, the usage of thermal effect can improve the performance. There is much research about the thermal effect of soft material, however, rare study of perpendicular magnetic anisotropy gradient induced by thermal gradient has been reported. In previous research, the realization of perpendicular magnetic anisotropy gradient, which can construct filed or current free spintronic devices, requires complex preparation process. Therefore, we aim to investigating the temperature dependent perpendicular magnetic anisotropy and offer a simple method for solving the perpendicular magnetic anisotropy gradient creation.

Moreover, magnetic domain-wall logic (DWL) based on magnetic shape anisotropy

is an important branch of spintronic devices. This DWL can achieve logic function based on electrons' spin. Many researchers are committed to using DWL to simplify the existing complex logic architecture. However, previous studies only focused on the logic functions of DWL, but did not make use of the nonvolatile memory capacity of spintronic devices. In this thesis, we aim to design a new type of DWL that combines computation and memory function to achieve in-memory computing which providing a new development direction for DWL.

1.4 Thesis outline

In Chapter 2, the basic theoretical background related to this work and the major discovery and innovation device of spintronics based on the magnetic material NiFe and CoFeB are documented.

All the experiment techniques used for Chapter 5-6 are discussed in detail in Chapter 3. The collaborating works' techniques are listed without further discussion.

In Chapter 4, the 'Defect-Correlated Skyrmions and Controllable Generation in Perpendicularly Magnetized CoFeB Ultrathin Films' is reported. The Scanning transmission electron microscopy (STEM) indicates that the defects introduced by the growth order affect the perpendicular anisotropy of the CoFeB which supported by the theoretical and simulations results. A series of vary thickness and growth order of CoFeB samples are investigated by First order reversal curves (FORC) based on wide-field Magneto-optical Kerr effect (MOKE) imaging system. With the FORC technique, the return magnetization can trap and stabilize skyrmions in these potential wells, and thus the skyrmion density and the stable region can be efficiently controlled.

In Chapter 5, the temperature-dependent magnetic properties of MgO/CoFeB/Ta thin films were investigated via the wide-field magneto-optical Kerr effect (MOKE) image system and VSM. Based on the previously research and our experimental data analysis, the saturation magnetization and perpendicular magnetic anisotropy (PMA) is correlated with temperature. We observed the PMA gradient in MgO/CoFeB/Ta thin films via the temperature gradient generator sample stage. Those studies provide well understanding of the magnetic properties of CoFeB PMA system and to guide the design of structures for various applications.

Chapter 6 demonstrate the basic function of a transistor logic unit with patterned Y-shaped NiFe nanowires by gate-controlling domain wall pinning and depinning which proved a paradigm of magnetic domain wall based in-memory computing. Magnetization analysis was performed with the wide-field magneto-optical Kerr effect (MOKE) image system. The corresponding simulation results explain the magnetic principle behind this nanostructure. Based on the observed transistor-like phenomenon, a feasible programmable spin-based logic gate, including OR, NAND, XOR gates were proposed. The operating and potential application for in-memory computing were discussed in the end.

Finally, the results in Chapter 4-6 are summarized and the future perspectives are discussed in the Chapter 7.

The diagram illustrated below concludes the logic of thesis.

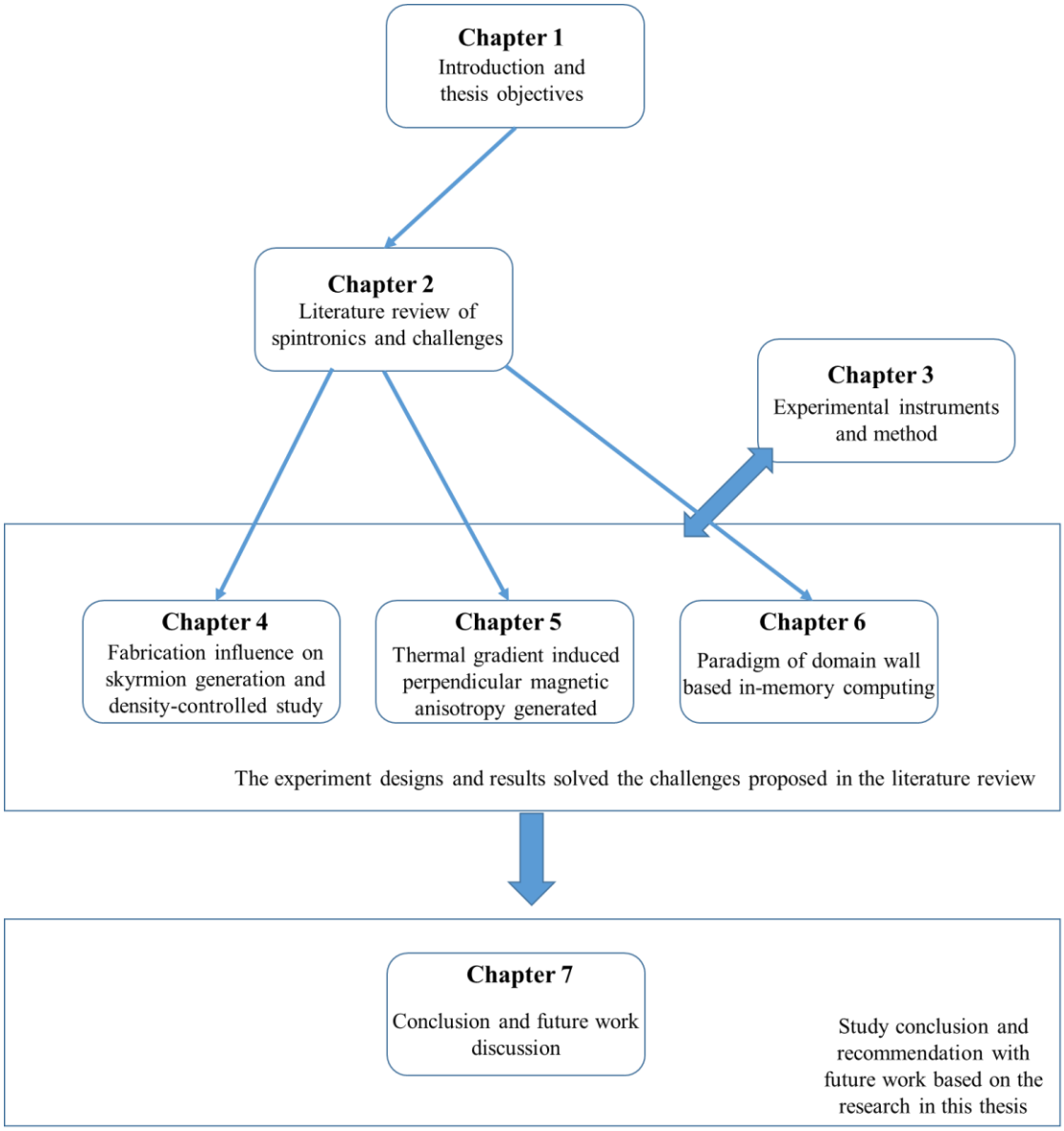

Figure 1.3 Diagram of the thesis logic outline.

Chapter 2 - Magnetic properties and spintronics applications

2.1 Introduction

Spintronics based on the electrons' spin factor is making rapid progress in both basic research discoveries and industrial applications in the past few decades. Magnetic recording, magnetic sensor, nonvolatile memories are providing more convenient for our life in real world. The discovery of physical phenomena, such as GMR (giant magnetoresistance), TMR (tunnel magnetoresistance), STT (spin-transfer torque), SOT (spin-orbital torque), propel the progress of basic physics. These outstanding phenomena could be observed owing to the advance of growth magnetic multilayer films and nanopattern for building the nanostructure technique.

This chapter aims to provide the background concerning the understanding of the works presented in this thesis. Firstly, a brief introduction and theory development of ferromagnetism will be presented. Subsequently, the magnetic anisotropy and domain wall will be discussed. The previously research for spintronic applications based on soft magnetic material CoFeB have been introduced. The research of temperature dependent magnetic properties of CoFeB and the creation and driven of skyrmion via thermal gradient are reported lately. The principle of skyrmion and its applications in PMA CoFeB are illustrated. The defect correlated skyrmion generation has been discussed. Eventually, the previous research of domain-wall logic based on the soft magnetic material NiFe are concluded. The challenges and problems have been discussed in the end of each subsection.

2.2 Ferromagnetism

The various magnetic materials are traditionally classified according to their bulk susceptibility χ. There are three typical groups' magnetic material: diamagnets, paramagnets and ferromagnets. For small and negative susceptibility (such as $\chi = -10^{-5}$), these materials called diamagnetic which the magnetic response opposes the applied magnetic field. Second group of materials called paramagnets, which the susceptibility is small but positive and typically $\chi = 10^{-3}\ to\ 10^{-5}$. The most well studied magnetic materials is the ferromagnetic solids, such as iron, cobalt and nickel. The susceptibility for ferromagnets is positive and much greater than 1, and can have values $\chi = 50\ to\ 10000$.

Under the relatively low values of external magnetic field H at constant temperature, the susceptibilities of diamagnets and paramagnets are constant. These materials exhibit 'linear' characteristic, that is the magnetization M is proportional to magnetic field H. The formula can be written

$$M = \chi H \tag{2.1}$$

The corresponding magnetization curves for diamagnets and paramagnets (or antiferromagnets) are shown in the Figure 2.1 (a) and (b) respectively[47].

As far as we know, the most significant group of magnetic materials is the ferromagnets including the ferrimagnets. The most common way to represent the magnetic properties of ferromagnets is by a plot of the magnetization M against magnetic field H, called Hysteresis loop. As shown in the Figure 2.1 (c)[47], the curve represents nonlinear compared with diamagnets and paramagnets, that is the permeabilities of the ferromagnet is not constant.

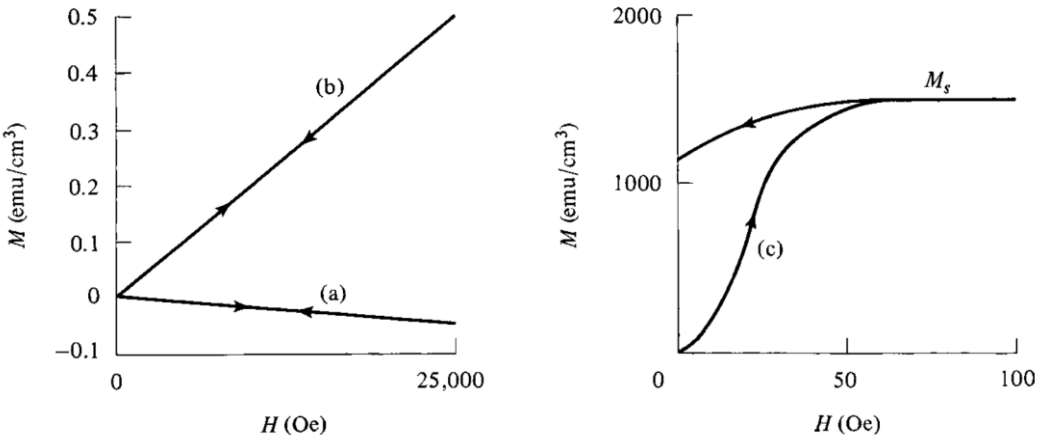

Figure 2.1 Typical magnetization curves of (a) a diamagnetic; (b) a paramagnetic or antiferromagnetic; and (c) a ferromagnetic or ferrimagnetic.[47]

These empirical facts were known long but not real progressed in understanding

ferromagnetism until Pierre Weiss in 1906 advanced his hypothesis. The Weiss theory contains two essential assumptions: (1) spontaneous magnetization; and (2) division into domains. Weiss first assumed that there is a molecular field, which strong enough to magnetize the substance to saturation without applied field, acts in a ferromagnets below its Curie temperature. For solving the demagnetized state problem, Weiss proposed second postulate that in unmagnetized condition the ferromagnet is divided into number of small pieces called domains. The magnetization within the domains is almost saturated (Ms), however, the direction of domain is random result in the specimen as a whole has no net magnetization. Under the external field, the multi-domain state will transfer to single domain and finally the magnetization direction is parallel to external field. This process is illustrated in Figure 2.2.

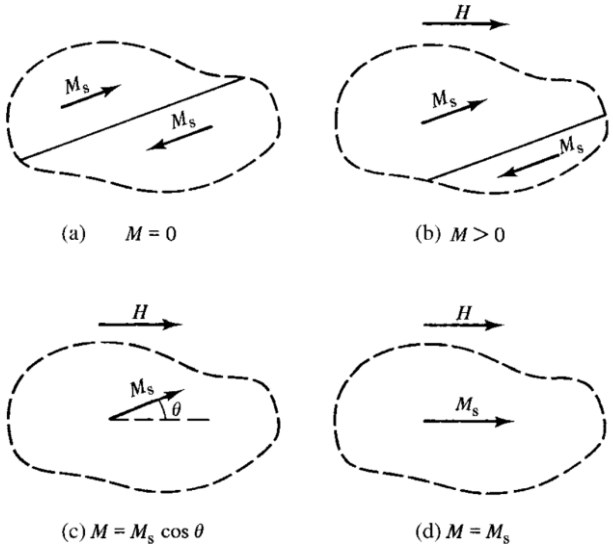

Figure 2.2 The magnetization process in a ferromagnet[47]

Weiss concluded this molecular field as the formula below:

$$H_m = \gamma M \tag{2.2}$$

The molecular field H_m proportional to the bulk magnetization *M*, where the γ is the molecular field coefficient.

Although the Weiss molecular field theory made a great advance on the explanation of magnetism, the physical origin of this field was not understood until 1928, when Heisenberg showed that it was caused by quantum-mechanical exchange forces. The term ‘exchange’ arises in the following way. When we consider the two atoms, which electron moving about proton, are adjacent, we cannot slight the possibility that two electrons exchange places due to electrons are indistinguishable. This consideration introduces the exchange energy into the expression for the total energy of two atoms. Heisenberg showed that the exchange energy forms an important part of the total energy in ferromagnetism. If two atoms i and j have spin angular momentum $S_i h/2\pi$ and

$S_j h/2\pi$, then the exchange energy between them can be given by

$$E_{ex} = -2J_{ex}S_iS_j = -2JS_iS_j \cos\phi \tag{2.3}$$

Where J_{ex} is a particular integral, called the exchange integral, which occurs in the calculation of the exchange effect, and ϕ is the angle between the spins. Based on equation 2.16, if J_{ex} is positive, E_{ex} is a minimum when the spins are parallel ($\cos\phi = 1$). When J_{ex} is negative, the lowest energy state results from antiparallel spins ($\cos\phi = -1$). It is obvious that a positive value of the J_{ex} is necessary condition for ferromagnetism to occur.

2.3 Magnetic anisotropy

2.3.1 Introduction

The term ‘magnetic anisotropy’ simply means that the magnetic properties depend on the direction in which they are measured. One factor of magnetic anisotropy is that it may strongly affect the shape of the hysteresis loop. There are several kinds of anisotropy classified: magnetocrystalline anisotropy, shape anisotropy, stress anisotropy and exchange anisotropy.

The crystal anisotropy, dependent on the crystal structure, including uniaxial anisotropy, or formally called magnetocrystalline anisotropy is due mainly to spin-orbit coupling. It is intrinsic to the material and determines the magnetic easy or hard axis hard axis within this system. The exchange interaction between two neighboring spins as a spin-spin coupling can be very strong and acts to keep neighboring spins parallel or antiparallel. But the exchange energy is isotropy, the spin-spin coupling cannot contribute to the crystal anisotropy. The orbit-lattice coupling is also strong which means the orientations of the orbits are fixed very strongly to the lattice. There is a coupling between the spin and orbital motion of each electron. When the spin and orbit tend to be reoriented by the applied field, the orbit is strongly coupled to the lattice which resists to reorient the spin axis. Therefore, the energy required to redirection the spin system, which called anisotropy energy, is just the energy required to break the spin-orbit coupling. This coupling is relatively weak. The existence of the spin-lattice coupling is that the lattice consists of a number of atomic nuclei surrounding cloud of orbital electrons arranged in space. And this coupling is also weak. The figure 2.3 illustrated these several relationships.

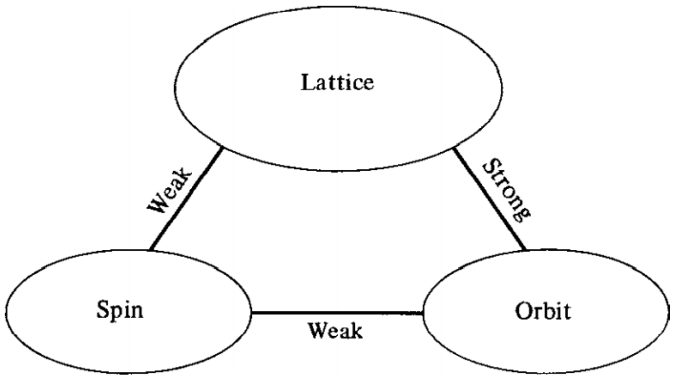

Figure 2.3 Spin-lattice-orbit interactions.[47]

The existence of magnetostriction can induced a new source of magnetic anisotropy by applying mechanical stress, which called stress anisotropy. Although the magnetostrictive strain is usual small in most magnetic materials, the applied mechanical stress can alter the domain structure and induced the anisotropy direction we need.

The exchange bias, which is usually characterized by an asymmetry along the field axis of a hysteresis loop, arises due to a surface or interfacial exchange anisotropy. The idea of a surface exchange anisotropy was proposed due to the regions of antiferromagnetic coupling to generally ferri-or ferromagnetic regions.

2.3.2 Surface magnetic anisotropy

The expression for the dominant anisotropy energy in thin film is given

$$E = -Kcos^2\theta \tag{2.4}$$

where E is the orientation-dependent energy of the magnetization, K is an anisotropy constant, and θ is the angle between the magnetization and the normal of the film[48]. The easy magnetization prefers to perpendicular to the plane of thin films when the K take positive value. To distinguish the contributions of different anisotropy energy competed in the thin films, we define the K_s as surface anisotropy energy while the K_v as bulk anisotropy energy. For a thickness of thin films is t which is much smaller than its exchange length, the average magnetic anisotropy energy can be written[16]

$$K_{eff} = K_v + \frac{2K_s}{t} \tag{2.5}$$

where Keff is the effective anisotropy energy in thin films. The parameters of K_s and K_v can be obtained by plotting the product K_t versus thickness t [16]. In the range of specific magnetic film thickness, the contribution of surface anisotropy exceeds that of the bulk anisotropy which result in perpendicular easy axis. The perpendicular magnetic

anisotropy of CoFeB studied in this thesis is attributed to the surface anisotropy[16].

2.3.3 Shape anisotropy

When consider a nonspherical magnetic system, the applied field will easier magnetize it along a long axis than along a short axis. The reason for this is that the demagnetizing field along a long axis is weaker than along a long axis. The external field along a short axis then must be stronger to produce the same true field inside the specimen. Therefore, shape alone can be a source of magnetic anisotropy, also we called shape anisotropy.

For further understanding the shape anisotropy quantitatively, we consider a specimen in the shape of a prolate spheroid with long axis c and short axis a as shown in the figure 2.4.

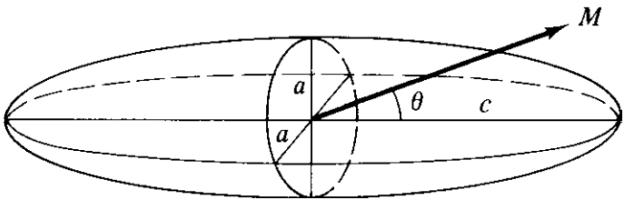

Figure 2.4 Prolate ellipsoid[47]

The applied magnetic field M at an angle θ to c. Then, taking components of M parallel and perpendicular to c, we have

$$E_{ms} = \frac{1}{2}[(M\cos\theta)^2 N_c + (M\sin\theta)^2 N_a] \tag{2.6}$$

Where N_c and N_a are demagnetizing coefficients along the c and a axis, respectively. This equation can be simplified as

$$E_{ms} = \frac{1}{2}M^2 N_c + \frac{1}{2}(N_a - N_c)M^2\sin^2\theta \tag{2.7}$$

This magnetostatic energy expression has an angle-dependent which exactly has same form as uniaxial crystal anisotropy energy. The shape-anisotropy constant K_s is given by

$$K_s = \frac{1}{2}\mu_0(N_a - N_c)M^2\ J/m^3 \tag{2.8}$$

As the equation shows, the 'strength' of shape anisotropy depends both on the axial ratio c/a of the specimen, which determines $(N_a - N_c)$, and on the magnitude of the magnetization M. According to the characteristic of shape anisotropy, it could be useful

to design nanostructures, such as nanowire, nanopillar, which advanced the development of spintronics. The Y-shaped nanowire studied in this thesis use a large axial c/a ratio to create strong shape anisotropy.

2.4 Magnetic domain and domain wall

2.4.1 Introduction

In 1906, the two great concepts of the domain hypothesis and the molecular field which introduced by Weiss. However, only latter concept was stressed by himself. Latterly in 1935, Landau and Lifschitz show the existence of domains is a consequence of energy minimization. A single domain specimen has associated with it a large magnetostatic energy. But that breakup of the magnetization into domains, providing for flux closure at the ends of the specimen, reduces the magnetostatic energy. Providing that the decrease in magnetostatic energy is greater than the energy needed to form magnetic domain walls then multi-domain specimens will arise. The direct experimental evidence for the domain structure of a real material was not found until 1949. Since that time, domain theory has become central to any discussion of magnetization processes.

2.4.2 Domain wall

Domain walls are interfaces between regions in which the spontaneous magnetization has different directions. If the neighboring atoms abruptly change their spin direction $180°$, a huge exchange energy associated with it, because the spins adjacent to the wall are antiparallel. But if this spin direction changed gradually over N atoms, the required exchange energy could be less. However, the spins within the wall are pointing away from easy directions, so that the crystal anisotropy energy within the wall is higher than it is in the adjoining domains. The anisotropy energy tends to make the wall thin, in order to reduce the number of spins pointing in no easy directions. Simultaneously, the exchange energy tries to make the wall as wide as possible, in order to make the angle between adjacent spins as small as possible. The result of this competition yields the wall has a nonzero width and a definite structure.

To calculate the energy and structure of a domain wall, we replace the exchange energy for a pair of atoms of the same spin S by using a continuum model

$$E_{ex} = -2JS^2 \cos\phi \tag{2.9}$$

with a continuum expression

$$E_{ex} = -2A\cos\left(\frac{d\phi}{dx}\right) \tag{2.10}$$

where $A = (nJS^2/a)$ is called the exchange stiffness or the exchange constant and ϕ is the angle between two spins. Here n is the number of atoms per unit cell, and a is the lattice parameter. It is usually estimated from the Curie temperature as $J \approx 0.3kT_c$. By simplifying the series expansion of $\cos\phi$, we have

$$E_{ex} = A\left(\frac{d\phi}{dx}\right)^2 \tag{2.11}$$

The anisotropy energy is given in the general case by

$$E_K = g(\phi) \tag{2.12}$$

where ϕ is measured from the easy axis. For uniaxial anisotropy, $g(\phi) = K_u\sin^2\phi$.

The wall energy is given by the sum of the exchange and anisotropy energies, integrated over the thickness of the wall:

$$\sigma_{wall} = \sigma_{ex} + \sigma_K = \int_{-\infty}^{\infty}\left[A\left(\frac{d\phi}{dx}\right)^2 + g(\phi)\right]dx \tag{2.13}$$

It seems conceptually and mathematically easier to think in terms of the torque acting on local magnetization. The torque resulting from the exchange energy is

$$L_{ex} = \frac{dE_{ex}}{d\emptyset} = A\frac{\partial(\partial\emptyset/\partial x)^2}{\partial\emptyset} = 2A\frac{\partial\emptyset}{\partial x}\frac{\partial(\partial\emptyset/\partial x)}{\partial\emptyset} = 2A\frac{\partial\emptyset}{\partial x}\frac{\partial^2\emptyset}{\partial x^2}\frac{\partial x}{\partial\emptyset} = 2A\frac{d^2\emptyset}{dx^2} \tag{2.14}$$

If the angle between neighboring spins is constant, the exchange torque acting on each spin will be equal and opposite, cancelling to zero. The torque resulting from an anisotropy energy is

$$L_K = \frac{dE_K}{d\emptyset} = \frac{\partial g(\emptyset)}{\partial\emptyset} \tag{2.15}$$

At equilibrium, these torques must be equal and opposite, giving zero net torque, at each point in the domain wall. After mathematical calculation and approximation, we have

$$A\left(\frac{d\phi}{dx}\right)^2 = g(\phi) \quad (a)$$
$$\frac{d\phi}{dx} = \frac{\sqrt{g(\phi)}}{\sqrt{A}} \quad (b) \tag{2.16}$$
$$dx = \sqrt{A}\int \frac{d\phi}{\sqrt{g(\phi)}} (c)$$

We can rewrite the equation 2.13 as

$$\sigma_{wall} = \sigma_{ex} + \sigma_K = \int_{-\infty}^{\infty} 2g(\phi)\, dx \tag{2.17}$$

And from the equation 2.29 (c)

$$\sigma^{180} = 2\sqrt{A}\int_0^{\pi} \frac{g(\phi)}{\sqrt{g(\phi)}} d\phi = 2\sqrt{A}\int_0^{\pi} \sqrt{g(\phi)} d\phi \tag{2.18}$$

For uniaxial anisotropy, $\sqrt{g(\phi)} = \sqrt{K_u}\sin\phi$, giving

$$\sigma_{uniaxial}^{180} = 2\sqrt{AK_u}\int_0^{\pi} \sin\phi\, d\phi = 4\sqrt{AK_u} \tag{2.19}$$

Various methods have been applied to the measurement of the wall energy. For example, the equilibrium spacing of domain walls in a sample of known geometry depends directly on the wall energy, if there are no barriers to wall nucleation and motion. In the research of skyrmion, it is a common method to estimate the DMI factor by using the domain wall energy[49, 50]. In this thesis, we first measured the uniaxial domain wall energy and then estimated the DMI value in perpendicular magnetic anisotropy CoFeB.

As illustrated in the figure 2.5(a), the Bloch wall, which would have its magnetization normal to the plane of the material, causes a large demagnetization energy. The Neel wall, in which the moments rotate within the plane of the specimen, as shown in the figure 2.5(b), results in a lower energy. The Neel wall do not occur in bulk specimens because they yield a rather high demagnetization energy within the volume of the domain wall. This energy becomes lower than the demagnetization energy of the Bloch wall, which leading the appearance of Neel wall, only occurred in thin films.

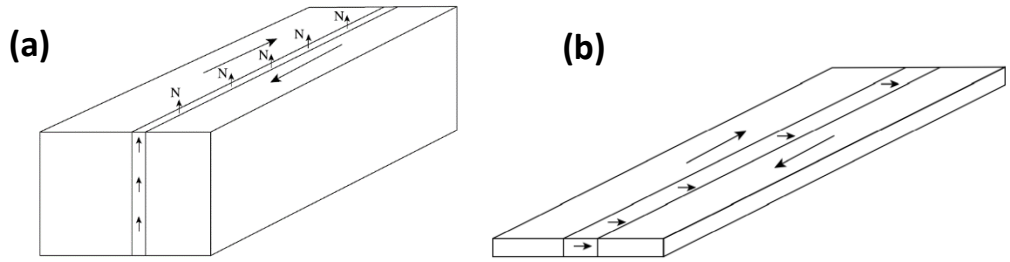

Figure 2.5 Schematic diagram for (a) Bloch wall, (b) Neel wall[47]

2.4.3 Domain processes

The changes in magnetization under applied magnetic field to a ferromagnet can be either reversible or irreversible depending on the domain processed involved. The definition of reversible or irreversible is weather the magnetization returns to its original value after application and removal of a magnetic field. More often both reversible and irreversible changes occur together, so that the magnetization usually does not return to its initial state after affected by external field.

The domain mechanisms are rotation and wall motion. Both processes contain either reversible or irreversible mechanisms, and the amplitude of the magnetic field determine the transition from reversible or irreversible.

Wall motion includes two distinct effects: bowing of domain walls and translation. The domain wall bowing is reversible process at low-field induced, and transfer to irreversible when the domain wall is sufficiently deformed. The translation of domain wall is usually irreversible unless the material is sufficiently pure.

Rotation of magnetic moments within a domain is also reversible under low-filed amplitudes. The occur of irreversible mechanism within the domain under high-field amplitudes when the field energy overcomes the anisotropy energy. Once the magnetic moments within the domain have rotated into a different easy axis the moments remain within the potential well surrounding this easy axis.

The whole magnetization processes usually contain both mechanisms of rotation and wall motion. A hysteresis curve contains the domain wall process and corresponding domain images showing in figure 2.6. Wall motion is the main process at the beginning of the magnetization. The steep forward branch of the magnetization curve is caused by domain wall motion (a-c), while inhomogeneous rotational process are responsible for the curved edge half loop (d-k).

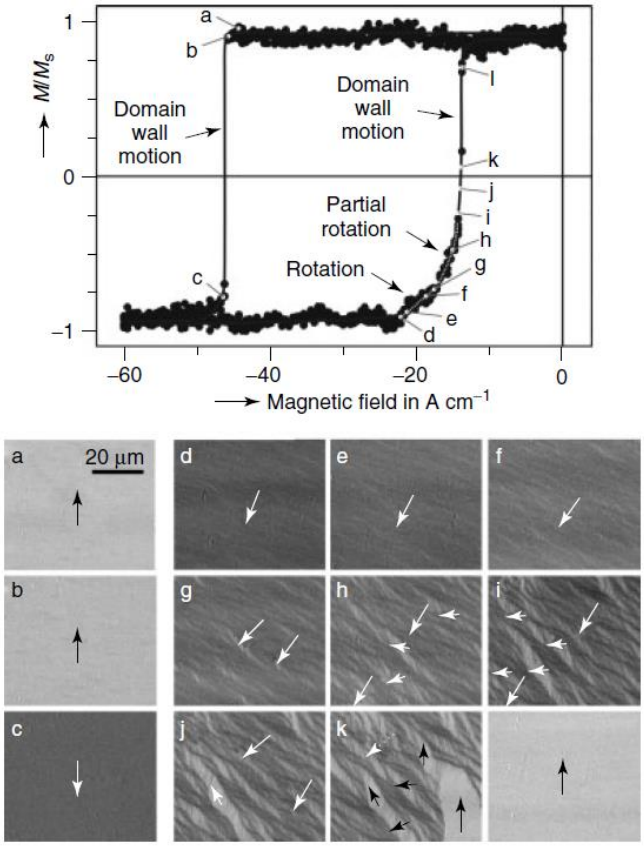

Figure 2.6 Magneto-optical hysteresis curve measured by wied-field Kerr microscope, together with domain images on a CoFe(20nm)/IrMn(10nm) bilayer film[51].

Evidently real materials contain crystal imperfections or impurities, or generally called defects. The investigations of Becker, Kersten and Neel have served to clarify the process taking place on the domain when a domain wall interacts with defects. They realized that the coercivity is corelated with the density of defects. The existence of defects truly impacts the magnetic properties.

2.5 CoFeB soft magnetic material

2.5.1 Introduction

Soft magnetic material refers to when the magnetization occurs in Hc is not greater than 1000 A/m, such a material is called soft magnet. For typical soft magnetic materials, the maximum magnetization can be achieved with the minimum external magnetic field. Soft magnetic materials are magnetic materials with low coercivity and high permeability, such as FeSi, FeNi, FeCo alloy.

Recently, the soft magnetic material amorphous CoFeB based spintronic devices

have attracted great attentions. Perpendicular magnetic anisotropy (PMA) was discovered in metal/oxide interfaces in 2002 [52], which is thought to be the result of electronic hybridization between the oxygen and the magnetic transition metal orbit across the interface [53]. This PMA phenomena has been observed in variety of amorphous CoFeB based thin films with crystalline oxides, including AlO_x, MgO, TaO_x etc[54, 55]. In 2010 a new type of memory device, STT-MRAM based on PMA material (CoFeB/MgO/CoFeB), was proposed [16], which has many advantages, such as low energy consumption and high thermal stability. Very recently, the skyrmion become a hot topic [56, 57]. The existence of skyrmions as particle-like was first studied theoretically by Bogdanov et al [58, 59]. Many scientists are working on it from understanding the basic theory of skyrmion to fabricating the next generation memory devices. The skyrmion could also be generated in CoFeB based ultrathin films[26, 60].

2.5.2 Development of perpendicular anisotropy in CoFeB/Oxide

Perpendicular magnetic anisotropy at Ta/CoFeB/MgO thin films, when it was first observed in 2010 [16], achieve applying into out-of-plane MTJ is a milestone. The reason why researcher have just found PMA at CoFeB recently since the PMA was first discovered at metal/oxide in 2002, it's that the presence of B at CoFeB/MgO interface weak the Fe-O bonding. Interfacial perpendicular magnetic anisotropy between the Fe/MgO is predicted to result from hybridization of Fe 3d and O 2p orbitals[61]. The key to PMA generated at CoFeB/MgO interface is preventing the B diffusion to the interface upon the annealing. Thanks to the Ikeda et al. replay the Pt by Ta, which is known to attract the B, can draw B out from the CoFeB/MgO interface during the annealing. And the interfacial perpendicular magnetic anisotropy in CoFeB/MgO via various buffer layers has been investigated in the following years[62]. On the other hand, the first-principles investigation of the PMA at Fe/MgO and Co/MgO interfaces indicated that the Co-rich at MgO interface will also lower the PMA value[63]. This agrees with experimental findings that Fe-rich $Co_xFe_{1-x}B$/MgO structures have lager PMA[64].

Meanwhile, Worledge et al. [54, 55]from IBM also discovered the same strong PMA phenomena from Ta/CoFeB/MgO. In their research, various of buffer layers have been investigated such as Cr, Ta, Ru, V, Ti, Al, Mg, W. These samples are made for buffer/CoFeB (tnm)/MgO (0.9nm)/Fe (0.3nm)/TaN (5nm) with t ranging from 0.3-1.6nm. These samples were annealing at 240℃ for 1 hour. From their results, the strongest perpendicular anisotropy was obtained for the Ta buffer, which the interfacial anisotropy is 1.8mJ/m^2. The perpendicular anisotropy energy of Ru/CoFeB/MgO only has 0.5mJ/m^2, which is much smaller comparing with buffer Ta. This result indicates that the Ta as a good getter for B than another metal buffer.

The perpendicular anisotropy of CoFeB/MgO based structure has been investigate in various buffer and capping layers. Ta as a usual buffer layer has been used in PMA CoFeB structure, however, has several drawbacks: it forms a dead layer at the interface of CoFeB and cause a greatly increase in Gilbert damping in structure of

Ta/CoFeB/MgO [16]; Ta also diffuses into CoFeB toward the MgO layer as annealing temperatures over 300℃ [16]. Thus, other buffer layer Hf has been tried recently by Liu, Cai, and Sun [65], which observed a 35% increase in PMA at the MgO interface. Hf can providing a smooth surface for CoFeB contact layer because it is low roughness. In 2014, they replace the Hf to Mo and build Mo/CoFeB/MgO structure which has better thermal endurance [66].

Another efficiency method to avoid the disadvantage of Ta buffer layer is insert a TaO thin film which the structure is Ta/TaO/Ta/CoFeB/MgO/W stacks. The process of Ta diffused into CoFeB layer has been decreased by the presence of TaO when annealing at 350℃ [67]. Because of the presence of TaO, the Ta who used to diffuses into MgO, now tend to stay where they are.

Several groups research the impact of capping layer on magnetic anisotropy and damping in MgO/CoFeB/capping layer structures [68, 69]. They found that the V could be the better capping layer for CoFeB/MgO or MgO/CoFeB structure. First, the reduced Gillbert damping coefficient, which agree with previously research in FeV alloys that exhibit low Gilbert damping [70]. Second, there is no appearance of dead layer occur at CoFeB/V interface [68].

In conclusion, the discovery of perpendicular magnetic anisotropy at transition metal (TM)/oxide brings us a good way to design better spintronic device such as STT-MRAM based on MTJ. For building a more efficiency device, the research of PMA among the TM/oxide is crucial. From the Pt/Co/AlOx to the CoFeB/MgO, researcher is working on finding a better PMA structure to make better applications. As previously discuses, the CoFeB PMA structure still has room to be improved, such as combing with different buffer or capping layer. The perpendicular magnetic anisotropy for repeated multilayer CoFeB structure is also a worth topic which should be investigated in future. And the application of PMA based on CoFeB is still worth us to study.

2.5.3 CoFeB-based spintronic devices

MRAM based on Perpendicular magnetic anisotropy CoFeB

MTJ based on PMA ferromagnetic material with low current-induced and high thermal stability for magnetization switching is attracted many researchers to study and manufacture it. Among many of PMA material, such as (Co, Fe)-Pt alloy, Co/(Pd, Pt) multilayer, none of them sufficient high thermal stability and low current at same time to achieve the high TRM ratio for downscale dimension. However, in 2010, S. Ikeda et al.[16] proposed a PMA MTJ which meet these conditions within one structure at first.

First of all, the factor of thermal stability is E/k_BT, for non-volatility recording layer, this value should larger than 40 [71] where $E= M_SH_KV/2$ is the energy barrier, k_B is Boltzmann constant and T the temperature, M_S is the saturation magnetization, H_K is the anisotropy field and V is the volume of ferromagnetic layer (sometime also write as $V = A \times t$, where A is the area and t is the thickness of ferromagnetic layer). The anisotropy energy density $K= M_SH_K/2$ should be high enough to overcome the problem

of thermal stability caused by reducing dimension in nanoscale. The threshold current for perpendicular magnetic reversal based on LLG equation express as

$$I_{C0} = \alpha \frac{\gamma e}{\mu_B g} M_s H_K V = 2\alpha \frac{\gamma e}{\mu_B g} E \tag{2.20}$$

where α is the magnetic damping constant, γ the gyromagnetic ratio, e is the elementary charge, μ_B is the Bohr magnetron and g is a function of the spin polarization of the tunnel current and the angle between the magnetizations of the free and the reference layers [72, 73]. Similar equation as we discussed above for in-plane anisotropy which the E should be replaced by E_{demag} resulting in large E, which is the reason a lower critical current is required for perpendicular anisotropy. This function indicates that as a given E, the low damping α can cause low switching current.

The main result they obtained for 40-nm-diameter MTJ based on PMA CoFeB/MgO is showing in the figure 2.7, which shows clear switching between high- and low-resistance states corresponding to antiparallel and parallel in the R-H curve. In their works, the results of the magnetoresistance changing by applying out-of-plane magnetic field or critical current induced are obtained by measurements. From the linear fitting, they can obtain I_{C0} =49 μA and E/k_BT =43. J_{C0} against $\ln(\tau_p/\tau_0) = 0$ plot in figure 2.7, where τ_0=1ns is the inverse of the attempt frequency. The value of E/k_BT is large enough that the information can store more than 10 years. From these results, the equation (2.20) consistent with the values derivate from α, K and Ms which indicate this formula agrees with this MTJ.

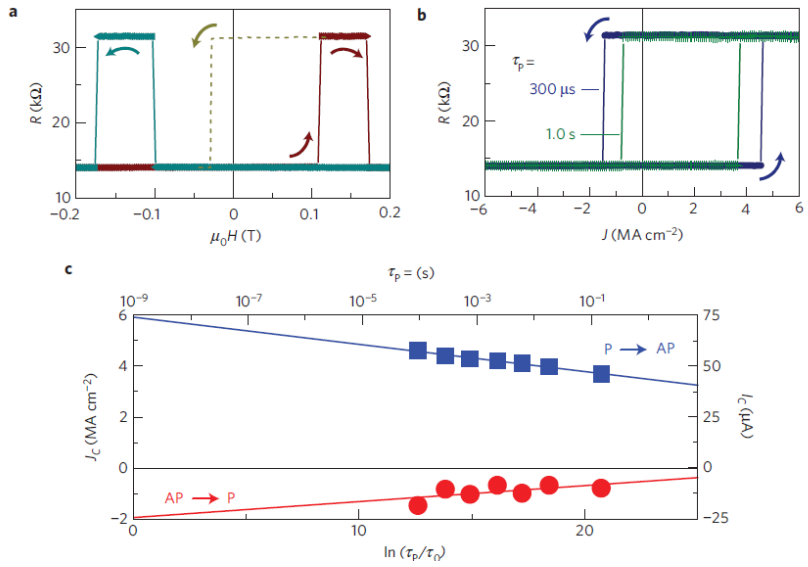

Figure 2.7 (a) R-H curve of PMA MTJ. (b) Result based on equation (2.33) with different current pulse duration. (C) J_c as a function of $\ln(\tau_p/\tau_0) = 0$which E/k_BT and J_{C0} are determined.[16]

Temperature dependence of perpendicular magnetic anisotropy in CoFeB

A CoFeB-MgO based MTJ with a perpendicular easy axis (p-MTJ) is becoming the most popular structure for MRAM fabrication. CoFeB/MgO heterostructures are a promising candidate for an integral component of spintronic devices due to their high magnetic anisotropy and low Gilbert damping. However, the thermal fluctuations is one of the inevitable problems in electronic or spintronic devices. The temperature difference can significantly affect the magnetic properties of the material and even the performance of the whole device. Therefore the study of thermal effect on magnetic material is essential.

A lot of work and progress have been made in the research field of the effect of thermal on magnetic properties of CoFeB system. The energy barrier E that determines the thermal stability factor of CoFeB-MgO based p-MTJ as a function of temperature has been reported[74]. E with the decrease of MTJ size, the influence of temperature will increase. When the MTJ diameter scalar down to 33nm, the E and anisotropy energy take about the same value and show similar temperature dependence[74]. The experimental results are showing in the figure 2.8.

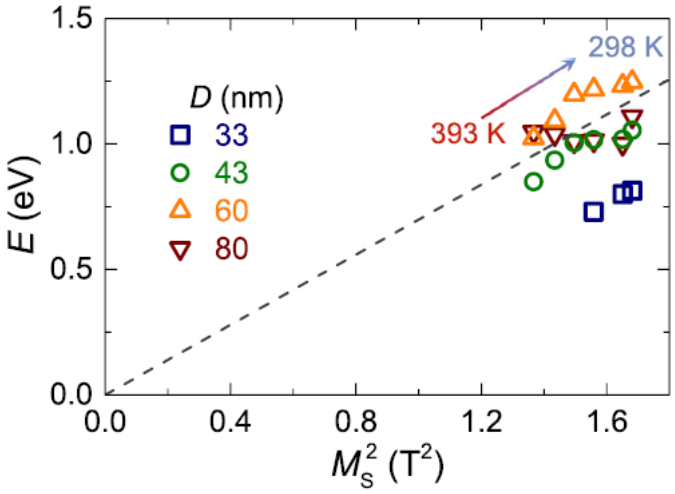

Figure 2.8 Energy barrier E plotted against the square of spontaneous magnetization Ms for MTJ with different diameter size measured at different temperature T. Dashed lines are the linear fit for the diameter lager 43nm[74].

H. Sato et al have proposed that the thermal fluctuations are different between the bulk and interface magnetization[75].

In addition to the influence of thermal fluctuations on the magnetic properties of materials, how to make good use of heat has become a major research direction. One of the most outstanding approaches is heat-assisted magnetic recording (HAMR)[76, 77], and the commercial products have been launched by Seagate most recently. The principle of HAMR devices is suppressing the superparamagnetic limit and the shape or crystal anisotropy enhances the magnetic switching fields (and therefore the coercivity), while a heating laser pulse that decreases coercivity for a short period of

time is used to allow for a magnetic bit writing process. The highly anisotropic FePt based HAMR devices achieved 1.4 Tb in^{-2} at laboratory environment in the early report[78].

While the HARM technique basically relies on induced magnetic switching at elevated temperature pulse, temperature gradients were also found to generate numerous spin-caloritronic effects. The research field of spin-caloritronic[79] is seeking a fundamental understanding of the interplay between charge, spin and heat. The classical thermoelectric effects in ferromagnetic material systems are well-understanding. The spin-dependent Seebeck effect has been observed in anisotropy magnetoresistance (MR)[80, 81], giant MR[82, 83], and tunnel MR[84, 85] regimes. The spin-Seebeck effect (SSE)[86, 87], which the occurrence of spin currents or spin accumulation in a ferromagnet due to a temperature gradient, is current under intense investigation.

The most recently research on temperature gradient creation and manipulation for skyrmion has provide a new way to driven the domain phase[88]. Their result shows clearly evident for thermally induced skyrmion motion which exhibited in figure 2.9.

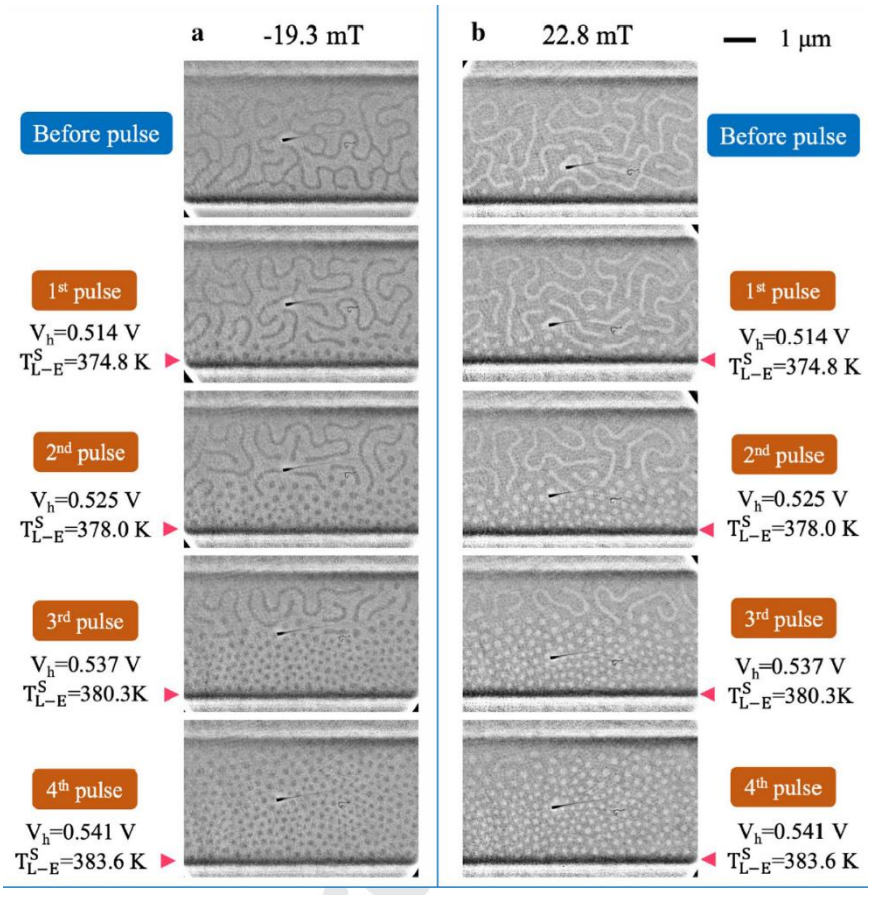

Figure 2.9 Skyrmion generations and propagation in the [Ta/CoFeB/MgO]15 multilayer by using the lower heater.[88]

This effect can be attributed to a combination of repulsive forces between the skyrmions, entropic forces, magnonic spin torque and thermal SOTs. The thermal generation and

manipulation could possibly trigger future discoveries in skyrmionics and spin caloritronics[88].

In conclusion, many good designs of MRAM based on CoFeB has been proposed in recent years. Moreover, the commercial STT-MRAM based on the in-plane CoFeB has been published most recently by many corporations. The STT-MRAM based on PMA CoFeB has the advantages of highest TMR among the many others and low power consumption, which has a potential to becoming the main memory devices in the future. The hot topic of SOT-MRAM, comparing with STT-MRAM, has the advantages of high response speed and low energy consumption. The usage of thermal effect can assist us construct spintronic devices with better performance, such as HARM. However, the relevant thermal research and industrialization are still in the early stage. Although the thermal gradient induced to spintronic devices has been investigated, the anisotropy gradient generated in the devices have not been studied systematically. In the previous research, the anisotropy gradient, which can realize field or current free spintronic devices[89], usually be induced by complex fabrication, such as photolithography. Therefore, a simple and general method without sample fabrication to induced anisotropy gradient is a big challenging.

2.6 Skyrmion

2.6.1 Introduction

Magnetic skyrmions are chiral quasiparticles and topologically regions, in which the spins point in all of the directions wrapping a sphere. Because of their topologically nontrivial spin textures, magnetic skyrmions exhibit many fascinating features, including emergent electromagnetic dynamics[90], and topological Hall effects[91, 92]. Magnetic skyrmions were first experimentally observed in B20 noncentrosymmertic crystals at low temperatures and low fields[93-97] and subsequently detected in ferromagnetic (FM)/heavy-metal (HM) thin films with perpendicular magnetic anisotropy (PMA) at room temperature[98-101]. Magnetic skyrmions can stabilize in ferromagnetic interface by Dzyaloshinskii–Moriya (DM) interaction energy, which, at the atomic scale, is defined as E_{DMI} = D(S1 x S2), where D is the DM vector and S1 and S2 are two coupled spins. The interaction between two magnetic atoms adsorbed on a non-magnetic substrate exhibiting large spin–orbit coupling (SOC). The interaction between the two atoms (red and green) is mediated by conduction electrons that scatter at a substrate atom (grey) (as shown in the figure 2.10), resulting in a Heisenberg-like exchange interaction (J) and in a DM interaction (D) between S1 and S2. D is oriented perpendicular to the triangle defined by the two magnetic atoms and the substrate atom. Comparing with RKKY interaction and atomic-scale DM interaction [102], the magnitude of them are quite similar. This large DM interaction energy allowed the formation of the smallest period of three atomic unit cells' spin spirals. A sizable DM interaction energy is also at the base of the small unit cell of the skyrmion lattice. In summary, the DM interaction is dominantly responsible for the intriguing physics of skyrmions and for their exciting potential applications in spintronic devices.

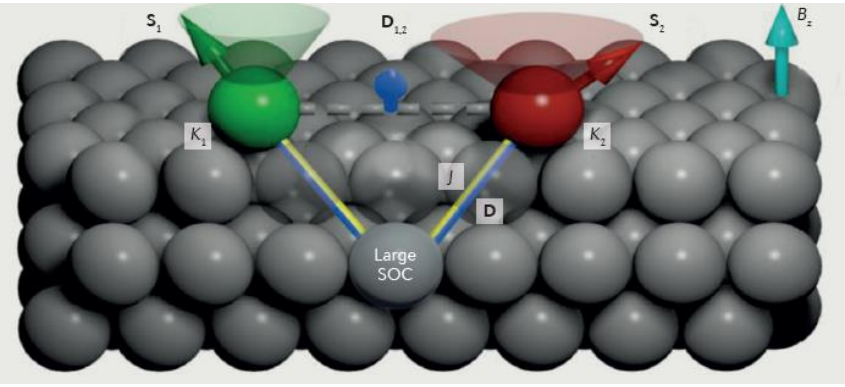

Figure 2.10 Schematic diagram of the Dzyaloshinskii–Moriya interaction [56].

Generally, there are two main types of magnetic skyrmions, including Bloch-type and Neel-type skyrmions, depending on the material properties, which illustrated in figure 2.11. The different of fundamental physical mechanism of hosting skyrmions,

the different types of skyrmions would be generated, which date back to the recent development of the fabrication of nanoscale magnetic materials. Specifically, the bulk DMI in B20-type materials supports the Bloch-type chiral skyrmion and takes the structural form shown in figure 2.11(a), whereas the interfacial DMI supports the Neel-type hedgehog skyrmion as shown in figure 2.11(b)[56, 103].

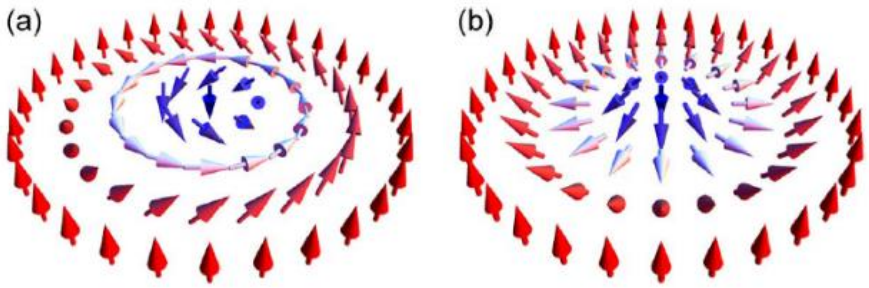

Figure 2.11 Bloch-type and Neel-type skyrmions. (a) In a Bloch-type skyrmion, the spins rotate in the tangential planes, that is, perpendicular to the radial directions, when moving from the core to the periphery. (b) In a Neel-type skyrmion, the spins rotate in the radial planes from the core to the periphery [57].

In recent years, magnetic skyrmions have been observed in several systems with broken crystal inversion symmetry, such as metallic, semiconducting and insulating materials. Most of significant experiment of skyrmion in ferromagnetic material are summarized in table 2.1.

Systems	Temperature (K)	Magnetic field (mT)	Skyrmion size (nm)
Ultrathin epitaxial films and multilayers			
1-ML Fe/Ir(111)	11	0	1
1-ML Fe/Ir(111)/YSZ/Si(111)	26.4	0	1
1-ML Pd/1-ML Fe/Ir(111)	2.2	1,500	3
3-ML Fe/Ir(111)	7.8	2,500	~3
2–3-ML Fe/2-ML Ni/ 5–15-ML Cu/15-ML Ni/Cu(001)	300	0	~400
Sputtered multilayers			
[Ta(5)/CoFeB(1.1) /TaO_x(3)]	300	0.5	700–2,000
$[Pt(3)/Co(0.9)/Ta(4)]_{15}$	300	0–2	400–500
$[Pt(4.5)/CoFeB(0.7)/MgO(1.4)]_{15}$	300	0–2	400–500
$[Ir(1)/Co(0.6)/Pt(1)]_{10}$	300	0–80	40–90
Nanostructured sputtered multilayers			
$[Pt(3)/Co(0.9)/Ta(4)]_{15}$	300	0–2	400–500
$[Ir(1)/Co(0.6)/Pt(1)]_{10}$	300	8	50–90
Ta(3)/Pt(3)/Co(0.5–1)/MgO_x/Ta(1)	300	0–4	70–190

ML, monolayer; YSZ, yttria-stabilized zirconia.

Table 2.1 Summary of experiment results of skyrmion generated in ferromagnetic martials[56]. The magnetic field illustrated here is referred to out-of-plane magnetic field.

To date, Néel-type has been observed at room temperature, and a prototype device has been implemented[104, 105].

2.6.2 Investigation of Skyrmion in CoFeB based nanostructure

Because of the scale and properties of skyrmion, the spintronic devices of skyrmion-based with high density and more stable endurance has attracted more researchers to investigate. First of all, controlling the number of skyrmion generated in memory liked trace is important. Wanjun Jiang et al. [26] are designing a structure that can generate a series skyrmion bulbs driven by induced current. The nanostructure is showing in the figure 2.12. This structure is made of Ta (5 nm)/$Co_{20}Fe_{60}B_{20}$ (1.1 nm)/TaO_x(3 nm) multilayer.

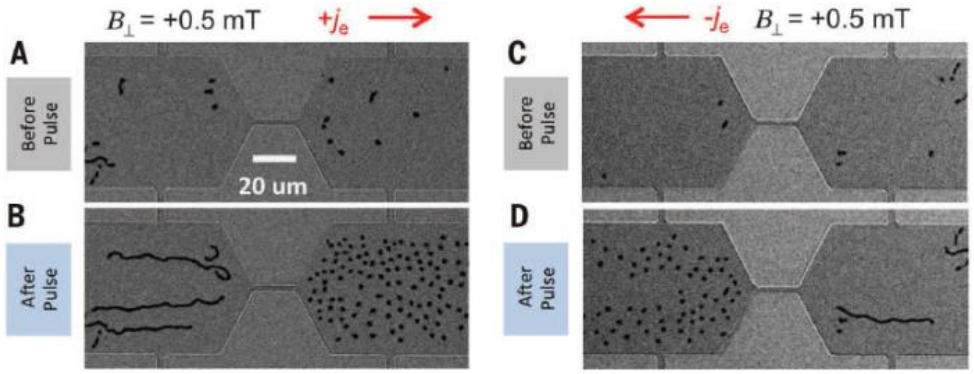

Figure 2.12 Nanostructure design of Ta (5 nm)/$Co_{20}Fe_{60}B_{20}$ (1.1 nm)/TaO_x(3 nm) multilayer. A perpendicular magnetic field is applied to these samples with B=+0.5mT. (A)(B) illustrate a changing when passing a 1 second duration current of $J = 5 \times 10^5 A/cm^2$ (normalized by the width of the device: 60 μm). In contrast, when adding a current of $J = 5 \times 10^5 A/cm^2$, the left hand side fill with the skyrmion bubbles [26].

As a result, they investigate the skyrmion generated influence by applying different current magnitude. The threshold current which can push the chiral domain passing the narrow constrict becoming skyrmions is $J = 6 \times 10^4 A/cm^2$.

Although skyrmions are topologically protected which means they can remain stable under changing external conditions, their formation still needs certain conditions to be met. Guoqiang Yu et al.[60] design a Engineered Asymmetry structure to induce a H_k gradient. They found that the skyrmion can only exist in certain region under specific external magnetic field and perpendicular magnetic anisotropy. When the perpendicular magnetic anisotropy is greater than a certain threshold, no skyrmion can be created by the external field regardless of conditions. The result is showing in figure 2.13.

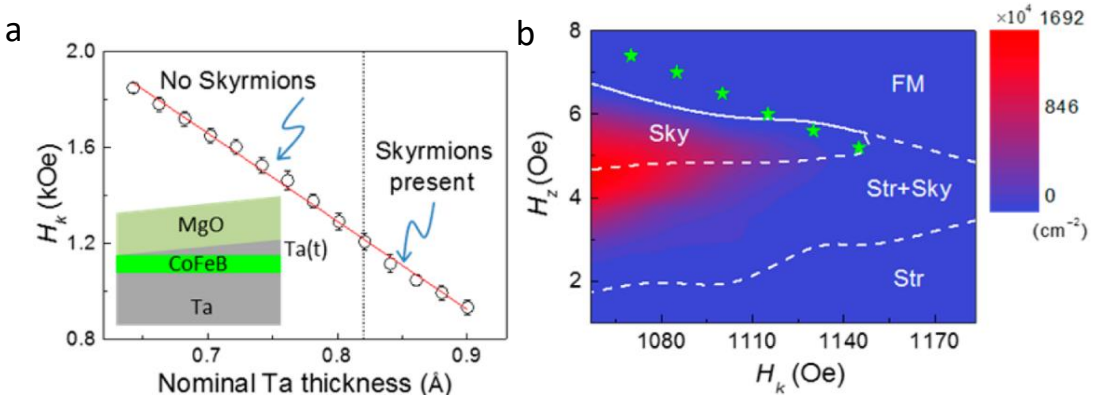

Figure 2.13 a, The measured perpendicular magnetic anisotropy as a function of the inserted Ta thickness. In the medium (strong) anisotropy regime, skyrmions can (cannot) be observed when a proper H_z is applied. The inset shows the sample structure. b, Phase diagram in the H_z and H_k plane. The color represents the skyrmion bubble density measured in a 233 μm × 174 μm area.[60]

The application of skyrmion based devices has been investigated in last decade. The topological protected skyrmion has the advantages of stability and long exit during. Therefore, the practicable skyrmion based spintronic devices is becoming the hot research topic. The skyrmion generation, motion and deletion in different material and scale has also been reported in others research[27, 106, 107].

2.6.3 Defect-skyrmion investigation

The defects correlate skyrmion investigation has been proposed most recently. The impact and usage of defects studies can provide a guidance of device fabrication and performance enhancement. The magnetic domain is randomly generated in the external magnetic field, and skyrmion is no exception. Therefore, clarifying the relationship between the skyrmion generation and structure defects offer a method to control the creation region of skyrmion. Based on this research pathway, the controlled individual skyrmion nucleation at artificial defects was proposed[108]. By using of ion irradiation, the artificial defects were induced into Co/Pt multilayer (as shown in the figure 2.14).

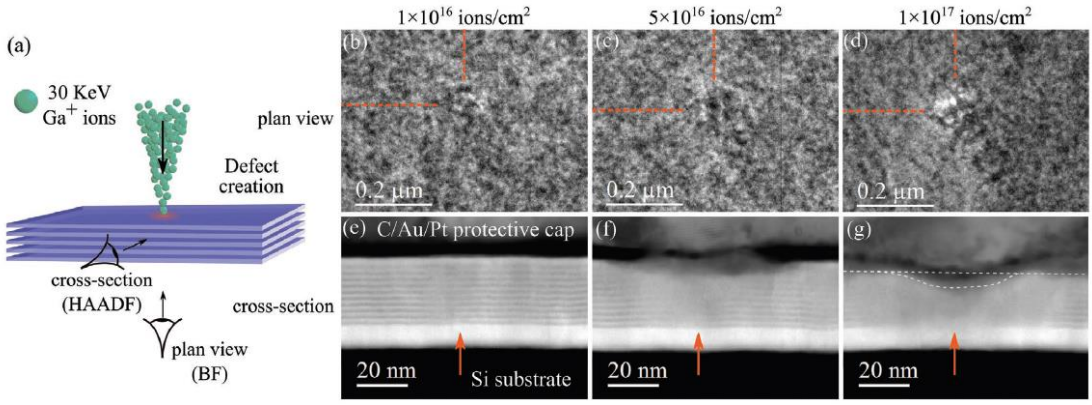

Figure 2.14 (a) Schematic of FIB defect creation. (b) to (d) bright field images of the defects in plane view. (e) to (g) looking straight down on the sample and high angle annular dark field images of defects in cross-section[108].

A Fresnel image showing in the figure 2.15, exhibits patterned with an array of 250nm diameter defects. Strikingly, single skyrmion can be observed at many of defect sites.

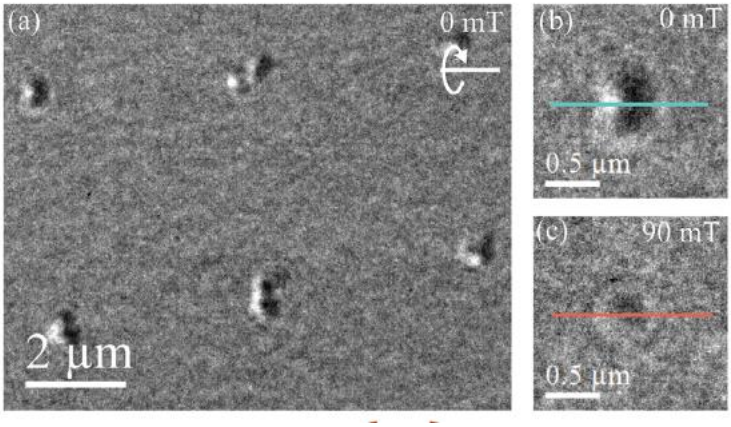

Figure 2.15 (a) Fresnel image of extended defects with ion dose (b) Enlarged image of a defect with skyrmion for comparison with (c) enlarged image of a saturated defect[108].

Moreover, defect-skyrmion phenomenon has been discovered and studied in many materials[109, 110]. The research use this skyrmion favor defect generation to create a defect track to control skyrmion motion direction[109]. Noticeable, most of the research in defect-skyrmion were based on crystal alloy magnetic materials. The defect-skyrmion in amorphous magnetic materials is still worthy of our study.

In conclusion, the skyrmion operate becoming easier from ultra-low temperature and high magnetic field applied to room temperature and with low or even without external magnetic field. However, the skyrmion research is still at a relatively earlier stage. More specifically, in the absence of a general guiding principle [98, 100, 111, 112] the applied magnetic field that produces skyrmions was previously determined empirically, and it is interesting that their hysteresis loops are so similar that rounded

loops are essential for skyrmion generation, even though the samples are very different[100, 104, 111, 113-115]. Rounded hysteresis loops are typical manifestations of multiple intermediate states during magnetization, correlating with material features such as defects. In general, the properties of materials are mainly determined during sample preparation, so the hysteresis loops with skyrmion generation imply a general relationship between fabrication, microstructure, magnetization, and the existence of skyrmions.

Importantly, clarifying the relationship can provide a comprehensive perspective on magnetic skyrmions and enable to establish principles for guidance from sample preparation to skyrmion generation and control. With a view to developing potential memory device, the method of controlling and enhancing the density of skyrmion is also worth studying. The skyrmion motion, edge effect and impact of anisotropy in materials still need us to investigate the basic physic behind these phenomena, particularly to progress from fundamental physics to.

2.7 NiFe based magnetic domain wall logic

The domain wall logic (DWL) based on soft magnetic material such as Permalloy (NiFe) has been investigated for decades which has a strong potential to replace present logic gate [43-45, 116]. Many important and basic studies of permalloy provide a very useful overview of magnetic domain generation and dynamic motion within the nanostructure due to the shape anisotropy. A. Hirohata, and Y. B. Xu, et al.[117] investigated various nanostructure based on the permalloy. Their works laid the foundation for the development of DWL. Parts of their designs are illustrated in the figure 2.16 which shows interesting nanostructure correlated domain formation.

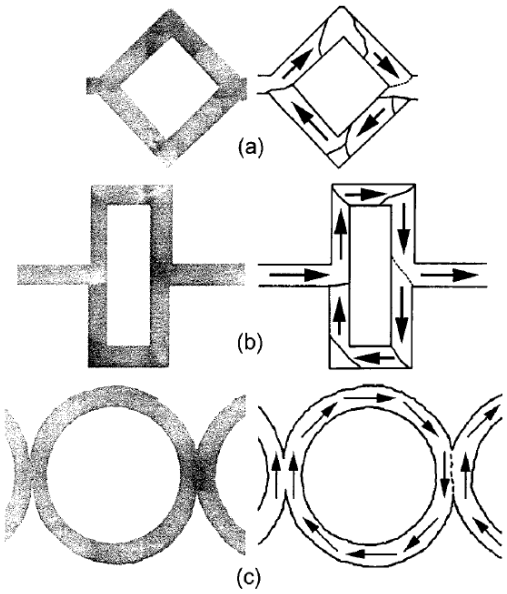

Figure 2.16 MFM images associated with schematic magnetic domain configurations of permalloy chain structures: (a) diagonal square (rhombus) chain (w = 1 and side length s = 10 m), (b) rectangular chain with wire (w = 1, longer side length l = 10, shorter side length l = 5and wire length l = 5 m) and (c) ring chain (w = 1 and outer diameter r = 10 m) in the demagnetized states.[117]

Based on previous research, early domain-wall logic gates was achieved by controlling the domain wall motion within well design nanostructure. Ferromagnetic NOT gate and shift register based on the DWL was proposed by R. P. Cowburn et al.[118]. Figure 2.17 exhibits domain-wall propagate along the wire under the rotating in-plane magnetic field within Y-shaped nanowire. By detecting two positions showing in the figure 2.18, the output represents not gate logic function. The success of this DWL makes spintronics more practical.

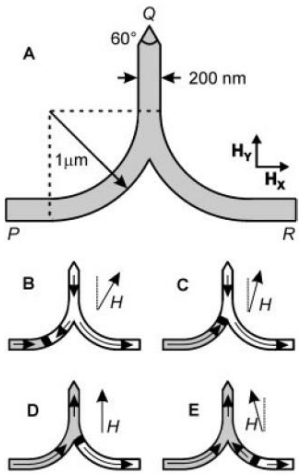

Figure 2.17 (A) Schematic of an all-metallic ferromagnetic NOT gate and directions of elliptical magnetic field components, Hx and Hy. (B to E) Diagrams describing the operating concept of NOT-gate magnetization reversal by illustrating successive magnetization directions (arrows) and domain wall positions (thick line) within a NOT gate that undergoes domain wall injection and is subject to a rotating magnetic field.[118]

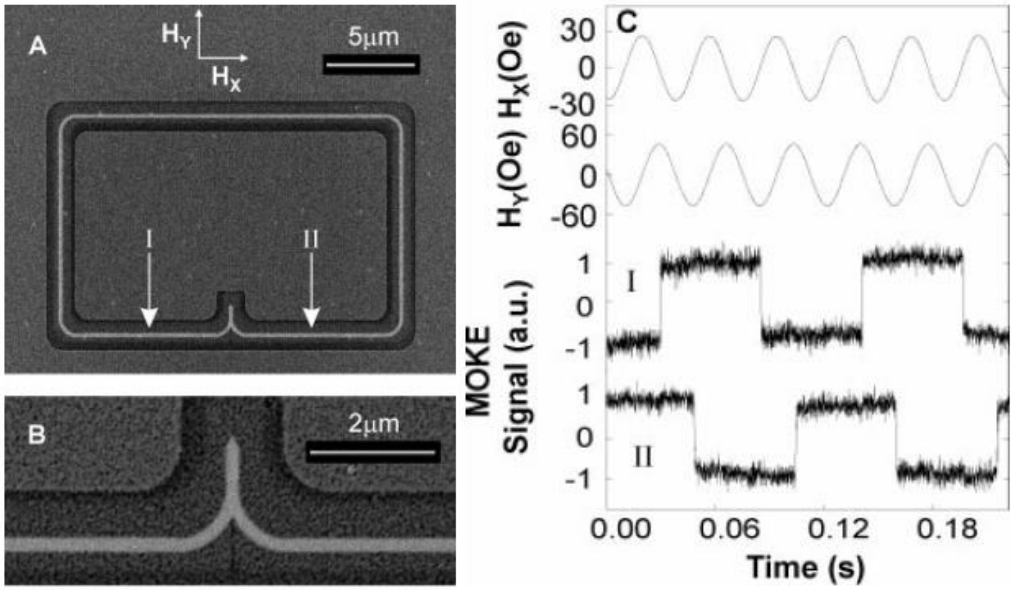

Figure 2.18 (A) FIB image of magnetic ring, including one NOT junction. Only the bright white shade corresponds to the magnetic material. (B) High-magnification FIB image of a magnetic NOT junction. (C) MOKE traces from the input (trace I) and output (trace II) of the NOT junction [indicated in (A)] within a counterclockwise rotating magnetic field (H_x=25 Oe and H_y=46 Oe).[118]

A bright idea comes out that they fabricated a magnetic ring structure containing a chain of these magnetic NOT gates to achieve a magnetic shift register. A fully flexible magnetic logic architecture must be able to process data flowing in different directions. The initial magnetic field input the domain wall into first NOT gate, and the domain

wall around the central NOT gate is bended or split in which the geometry of a domain wall breaks down. The continuously rotating magnetic field push the domain wall into second NOT gate and first gate magnetization was rewritten by different directions of external field. Thus, the complete design of this magnetic shift register contains 6 shift data in on direction and 5 shift data in the other direction as shown in figure 2.19(a). After testing the repeated operation of this shift register, the result of strong MOKE signal shows the operations performed correctly in the figure 2.19(b).

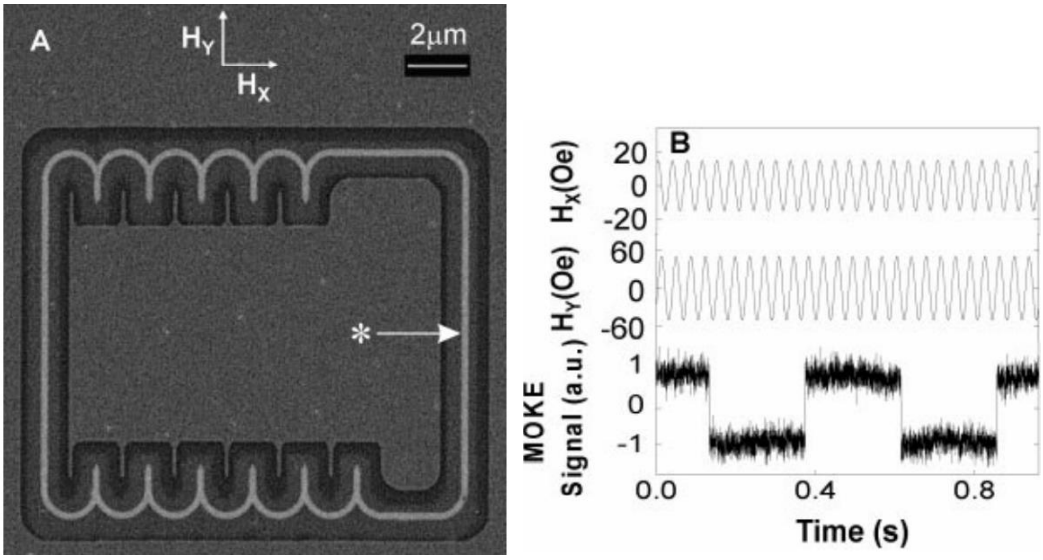

Figure 2.19 (A) FIB image of magnetic ring including 11 NOT junctions, with the asterisk indicating the position of subsequent MOKE analysis. The directions of elliptical magnetic field components, H_x and H_y, are also indicated. (B) MOKE analysis of an identical structure within a clockwise-rotating magnetic field (H_x=15Oe and H_y=50Oe).[118]

Most recently, a new design of chirality encode domain wall logic has been proposed which use the vertex direction to represent different data. Two type of vertex called clockwise and anticlockwise represent to ‘1’ or ‘0’. The basic geometry of the DWL in the chirality-encoded logic architecture is illustrated schematically in figure 2.20.

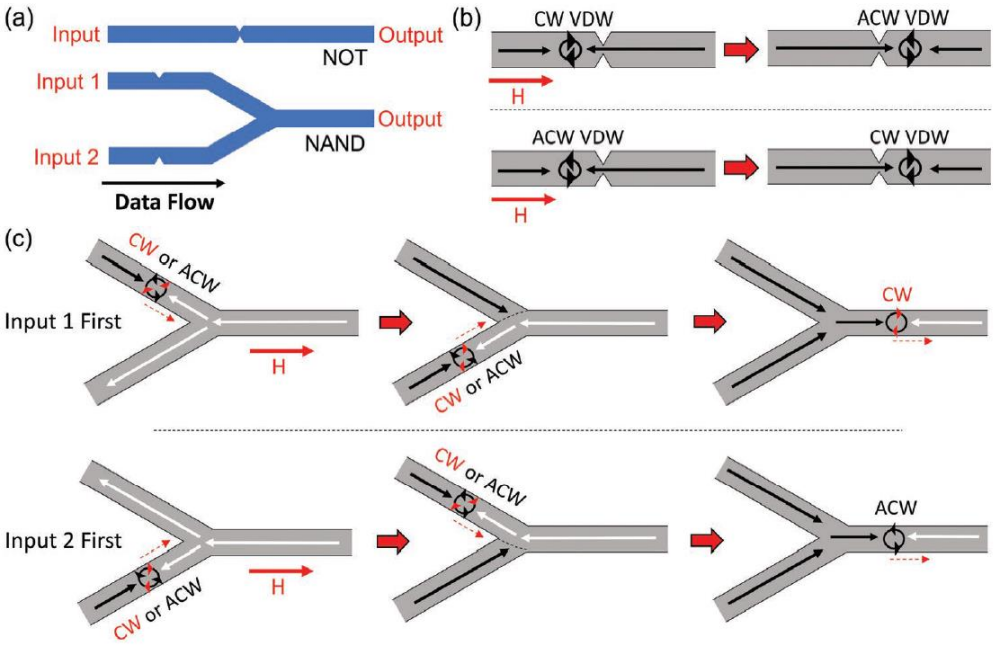

Figure 2.20 (a) Schematic diagrams illustrating the geometry of NOT and NAND gates in chirality-encoded DWL schemes. (b) Illustration of the operating principle of the NOT gates; as the DWs pass through the double notch their chiralities are inverted. (c) Illustration of the operating principle of the 2-in- 1-out junctions in AND/NAND/OR/NOT gates; the chirality of the DW in the output wire is determined by the switching order of the input nanowires.[116]

Based on this idea, two different domain-wall logic gates have been investigated. To test the feasibility, the experimental details of NOT gate and NAND gate are exhibiting in figure 2.21 and figure 2.22, respectively[116]. The behavior of the device illustrated in figure 2.21 was characterized using Magnetic Transmission X-ray Microscopy (MTXM), which allowed their magnetization configurations to be imaged in the presence of in situ applied magnetic fields. The figure 2.21(b) presents anticlockwise domain structure transfer to clockwise by passing the artificial notched region, which indicated the NOT gate function achieved.

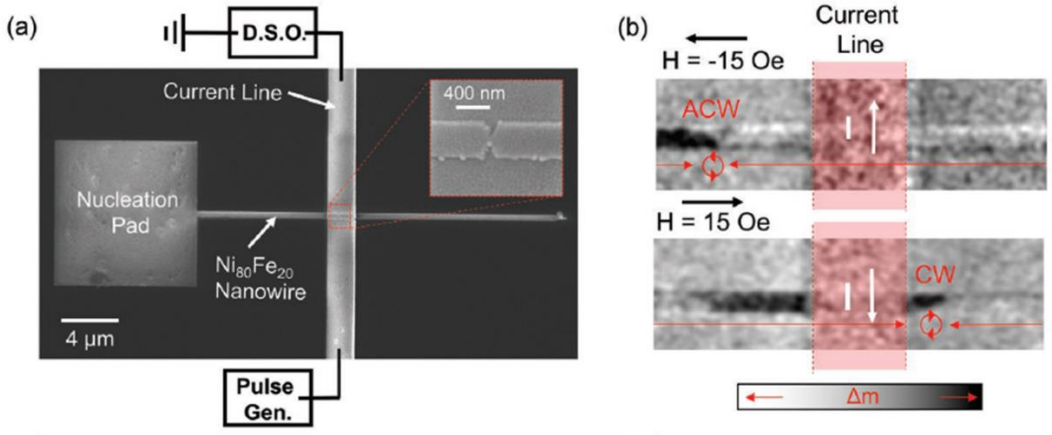

Figure 2.21 (a) SEM image of the NOT gate device. The inset figure shows an expanded image of the notched region (viewed through the gold current line). (b) MTXM images showing an ACW VDW being inverted to CW chirality on being passed through the double notches. The shaded red region represents the location of the current line, which obscures magnetic contrast.[116]

To demonstrate the magnetic NAND gate, the nanowire device of the design shown in figure 2.22(a). This device consisted of 2-in-1-out junctions with nucleation pads attached to each of the input nanowires to act as sources of domain-walls. One of the input arms induced notch and double notches were placed on the output arm. The figure 2.22(b) presents the results of domain-wall formation and motion which has the same function illustrated in the figure 2.20(c).

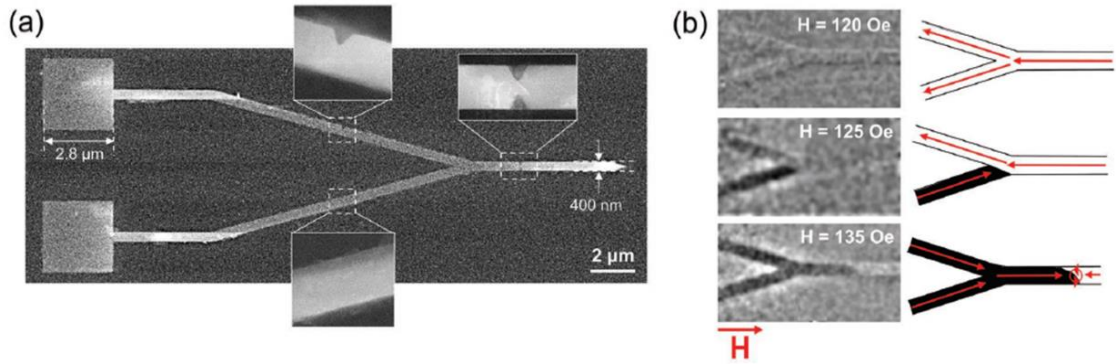

Figure 2.22 (a) SEM images showing one of the 2-in-1-out junctions measured in this article. The inset figures show the notched regions of the nanowires in detail. For the device shown only the top of the two input nanowires contained a notch. (b) Example MTXM images showing the switching of a 2-in- 1-out junction as the applied field was ramped. In this case, the bottom input switched first, followed by the top input, resulting in an ACW VDW at the output notches.[116]

The quasi-static micromagnetic simulations of junctions in 40nm thick, 400nm wide nanowires, as shown in figure 2.23, which are in a good agreement with experimental result gives the insight mechanical of the domain wall generation and propagation within this magnetic logic gate.

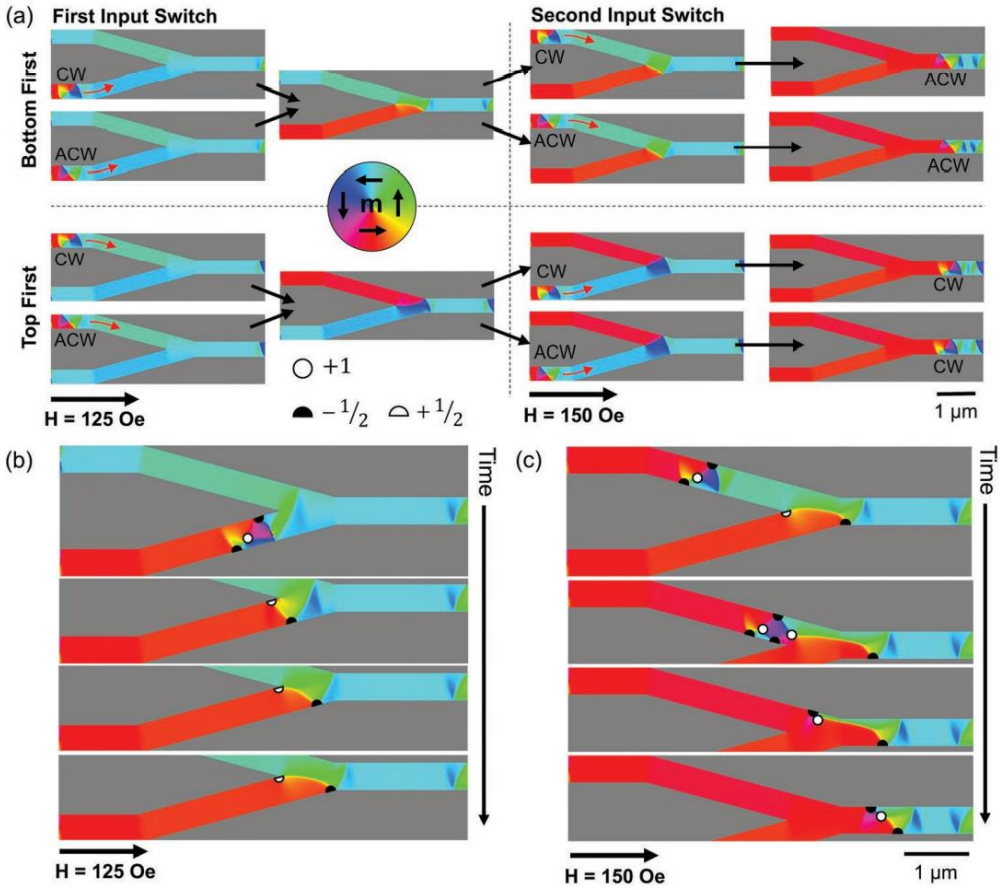

Figure 2.23 (a) Results of quasi-static micromagnetic simulations showing the various switching paths available for a 2-in-1-out junction. [116]

Beside the magnetic field as the input, the current induced domain wall motion in NiFe-based nanowire has been investigated for a few decades. The direct observation of domain wall scattering in patterned NiFe by current-voltage measurements was investigated by S. Lepadatu and Y. B. Xu[119]. They have measured the resistance versus applied current for samples with notch widths varying from 50nm to 250nm. The nanostructure of notched NiFe nanowire is showing in the figure 2.24.

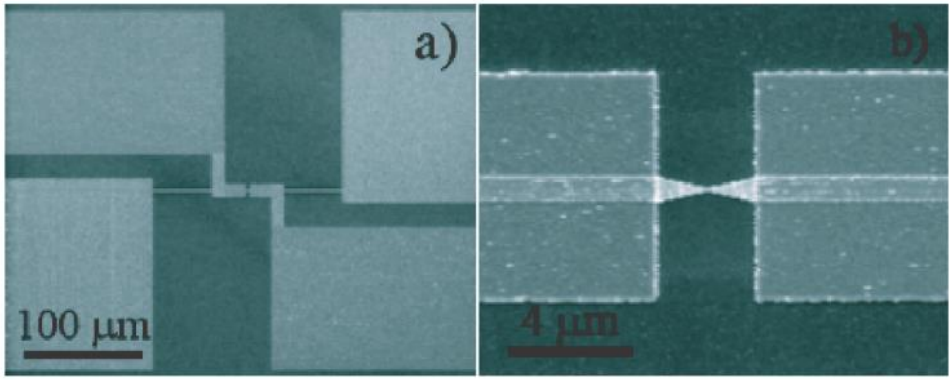

Figure 2.24 SEM images of (a) measurement pads geometry and (b) necked NiFe wire with 50 nm constriction width.[119]

Figure 2.25 presents the resistance versus applied current for the notched permalloy wires with notch widths ranging from 50nm to 250nm. A clearly abrupt drop in resistance is observed for the notched wire with notch widths in the range 50nm to 250nm, as the current exceeds a critical current and pushes DW motion in the direction of the current flow.

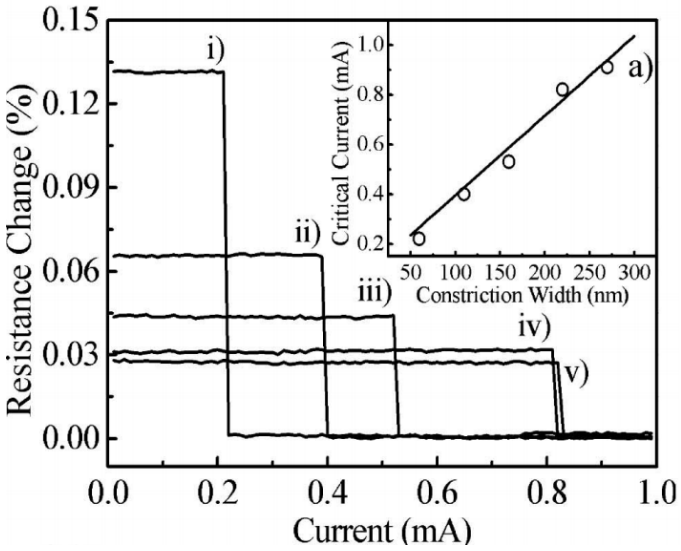

Figure 2.25 I-V measurements for necked NiFe wires with constriction widths of (i) 50nm. (ii)100nm, (iii) 150nm, (iv)200nm, (v) 250nm. In the insets, the average critical current density is plotted as a function of constriction width for NiFe.[119]

The discovery that domain walls can be pushed from such constrictions by a sufficiently large current has attracted considerable attention from researchers working on both theoretical investigation and potential applications[119-121]. The Invar nanocontacts designed by Peng Xu, et al.[122] exhibit a sharp drop in resistance with increasing bias voltage at room temperature without applied magnetic field. Moreover, it is possible to achieve logical NOT operations when combined two nanocontacts in comparison circuit.

In conclusion, the DWL based on soft magnetic material such as Permalloy (NiFe) has been investigated for decades and is believed to have a potential to replace present logic gate [43-46]. In conventional DWL, however, a continuous rotation magnetic field is applied on logic units [43, 123] and output detection method based on MOKE signal is hard to integrate for in-memory computing. The chirality-encoded architecture has been proposed most recently[46] which has big advance on spin logic where data is encoded within the structures and carried by continuous stream. The limitation of this chirality-encoded architectures, however, is that the output chirality was not totally correlated to the input switching order[46]. Previous research on DWL just focus on the function of the logic gate, and there is rare investigation of the combination of magnetic logic unit and memory. Therefore, combination of logic function and memory will be one of the important development prospects of spintronic devices based on permalloy.

Chapter 3-Experimental Techniques

3.1 Magnetron Sputtering

The methods of vacuum coating roughly include evaporation, ion plating, sputtering and gas phase reaction, among which sputtering is closely related to large-scale industrial production. It refers to bombarding the surface of the target material with ions accelerated by an electric field, causing the atoms of the material to escape from the surface, and then depositing on the substrate to form a thin film. Compared with other methods, the target material is generally larger, so the sputtering method can produce a large-area thin film with uniform thickness. In addition, this method does not need to increase the temperature of the target material. On the basis of ordinary two-pole sputtering, adding a magnetic field orthogonal to the electric field can achieve high-speed sputtering, which is called magnetron sputtering. The schematic diagram is shown in the figure 3.1.

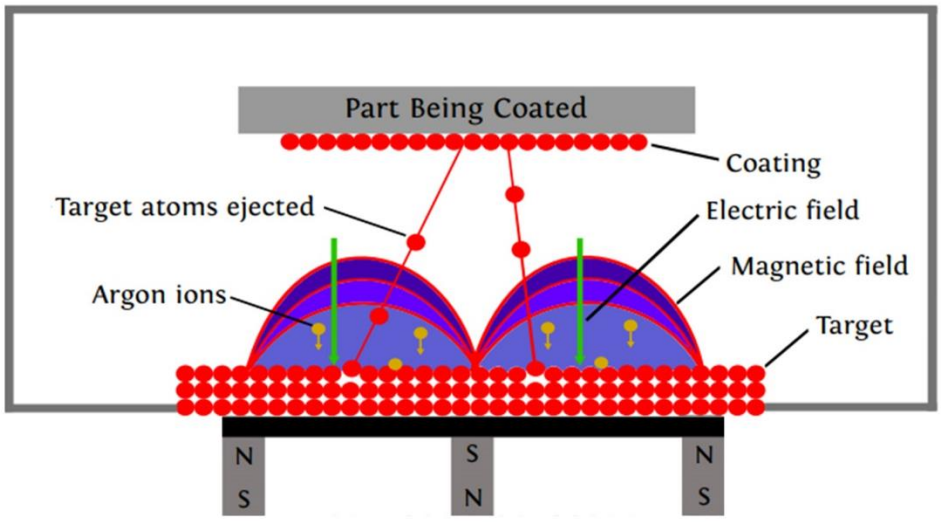

Figure 3.1 Schematic diagram of magnetron sputtering[124]

Magnetron sputtering is a kind of physical vapor deposition (PVD). The general sputtering method can be used to prepare metals, semiconductors, insulators and other materials, and has the advantages of simple equipment, easy control, large coating area and strong adhesion. Magnetron sputtering developed in the 1970s has achieved high speed, low temperature and low damage. Because of the high speed sputtering at low pressure, the ionization rate of gas must be effectively improved. Magnetron sputtering increases the sputtering rate by introducing a magnetic field on the surface of the target cathode and using the magnetic field to restrict the charged particles. Mgnetron sputtering consists in using two permanent magnets of opposite polarity located below the target used in this thesis. These magnets create a strong magnetic field (1000Oe-2000Oe) parallel to the target surface and orthogonal to the electric field used to ionize the Ar atoms. The accelerated Argon ions Ar+ will bombard the target which increases

the efficiency of the sputtering process and improves the quality of coatings.

In addition to the DC magnetron sputtering, there is also the radio frequency (RF) sputtering, which this RF sputtering was developed for sputtering the insulation material. When the RF power is changed to DC power, the surface of the insulator is covered by the positive charge carried by the ions flowing in, thus the potential difference between the surface of insulator and plasma is equal to 0. When the discharge stops, the sputtering also stops, so direct current cannot sputter the insulation target.

In order to further understanding of this problem, suppose a rectangular wave voltage V_M is applied to the target electrode. During the positive half cycle, when the insulator contacts the electrode, the surface will immediately gather electrons, and the outer surface V_S will become the same potential as the plasma (The capacitor between the potential surface formed by V_S and V_M will be charged). In the next negative half cycle, V_S changes to a negative potential. During this half cycle, ions flow in for sputtering, due to the ions are heavy and difficult to collect (the mobility is small), however, the potential on the insulator surface gradually approaches to the Plasma potential (the charged capacitor will slowly discharge through electrons). The same process (charging) repeated for the next half-wave. As a result, the sputtering of the insulator can be achieved just as the target surface existed a bias voltage V_{bias}. If V_M is a sine wave, a bias voltage will also be formed and sputtering of insulators can be also achieved. As a conclusion, a capacitor could be formed by the radio frequency current flowing through the insulator. Therefore, the insulator can be sputtering by the RF power. This method can also be used for metal sputtering. RF sputtering can be used for sputtering almost all materials from insulators such as MgO, Al_2O_3, etc. to metals.

All the thin films mentioned in the thesis were prepared by the magnetron sputtering instrument showing in the figure 3.2. The main parameters of this magnetron sputtering are listed below:

Number of Substrates: 18
Number of Targets: 8
Vacuum pressure: 5×10^{-5}Pa
Plasma gas: Argon
Sputtering pressure: 0.5 Pa
Distance between Substrate and Target: 80-110 mm
Target diameters: 50 mm, 60 mm, 75 mm
DC power: 35-120 mA
Deposited rate: .03-1.5 A/s
Magnetic field: 450 Oe

Figure 3.2 The magnetron sputtering instrument used in this thesis. The red notes exhibit the different components of magnetron sputtering, including power supply (DC power and RF power), vacuum chamber and controller computer.

All the CoFeB ultrathin films were prepared by magnetron sputtering. The samples were deposited on the thermally oxidized Si (SiO_x). The silicon wafers were divided into several 2.5*2.5cm squares and stored in Ethanol. The square substrates were mounted on the top of chamber after dried. The advantage of this magnetron sputtering instrument is that it has more targets and more sample growth sites. This setup ensures that more multilayer samples can be grown under the same growth conditions without opening chamber. 16 sample growth sites ensure that all the samples of CoFeB studied in the thesis can be grown in only one sputtering period with same growth condition.

Controlling of magnetron sputtering parameters is necessary for the comparison of the properties of ultrathin films. The three key parameters can control the sputtering rate: DC bias voltage, RF power and Gas flow rate. In order to ensure the homogeneity of each layer of the samples, the samples were sputtered at a lower growth rate. The time of Ta(5nm) and MgO(3nm) sputtered onto the sample are 77.47s and 198.1s respectively. Due to the perpendicular magnetic anisotropy of CoFeB is very sensitive to the thickness, the growth rate sets to 0.073nm/s which the RF power is 313~315V. The lower sputter rate can also ensure the accuracy of CoFeB thickness.

3.2 Characterization measurement techniques

3.2.1 Vibrating Sample Magnetometer (VSM)

The idea of Vibrating Sample Magnetometer (VSM) was published by S. Foner[125]. It is based on the flux change in a coil when a magnetized sample is vibrated near it. The sample is sticked to the end of nonmagnetic rod, the other end of which is fixed to a loudspeaker cone or to some other kind of mechanical vibrator (as shown in figure 3.3). The detection coils can pick up the signal generated by the vibrating sample, and the magnitude of this signal is proportional to the magnetic moment of the sample. The signal then is amplified by the lock-in amplifier which is sensitive only to signals at the vibration frequency.

VSM provides experimental results in magnetic moment (m) against the applied magnetic field (H) where calibration of both H and m is required on weekly bases to keep the accuracy. The applied magnetic field H is calibrated by first calibrating the Hall probe at zero field shield to check the zero point. By placing the probe into an applied magnetic field, the Hall probe measures and calibrates against a Lakeshore 425 gauss meter which is a secondary standard. For magnetic moment calibration, the sample is replaced by a Palladium foil whose geometry and dimension is similar to the sample. Palladium has a fixed value of moment at any applied field.

Magnetization curves generating from the VSM are providing the general magnetic properties, such as coercivity (H_c), saturation magnetization (M_s) et.

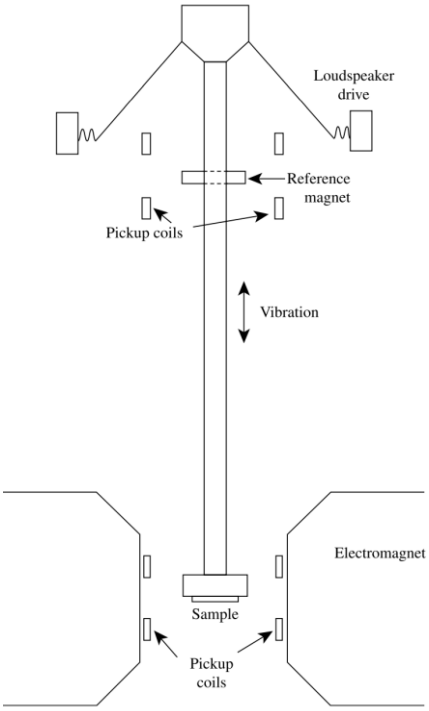

Figure 3.3 Schematic diagram of Vibrating sample magnetometer (VSM).[47]

The specific version of Microsense VSM used in this thesis is the DMS Model 10

(as shown in the figure 3.4). This instrument has a high sensitivity of 10^{-6} emu. Rotation of the magnet is possible within the range of -540 to +540 degrees (resolution< 0.1 degree). The system can reach a maximum magnetic field of 20 kOe. Temperature variation from 100K to 773K is available via a gas-flow system. Induced nitrogen flow over the heater can controls the temperature stabilize within 0.01K error.

Figure 3.4 The DMS Model 10 VSM used in this thesis.

All the magnetic characterization and temperature variation experiment of samples were measured by DMS Model 10 VSM.

The magnetic moment (m) versus the external field (H) plotting the magnetization curve provides the general magnetic properties of CoFeB ultrathin films studied in this thesis. The in-plane and out of plane magnetic properties can be measured via different type of probes. Due to the saturation magnetization of perpendicular magnetic anisotropy of CoFeB changes very slightly at different temperatures[74, 75], this high sensitivity precision and high temperature stability Model 10 VSM was chosen for measurement. The characteristic measured by VSM provide the key magnetic properties for temperature dependent CoFeB investigation, such as saturation magnetization (M_s), saturated applied field for hard axis (H_a), coercivity (H_c).

3.2.2 Scanning electron microscope (SEM)

The scanning electron microscope arises from that the best conventional optical microscope has the limitation of magnification. In electron microscopy the electrons are usually accelerated to high energies of between 2 and 1000 KeV. Those high-energy electrons will interact with the atoms in the specimen. Some incident electrons will elastic or inelastic scattering and may end up in a direction back out of the sample surface, which called backscattered electrons. The number of these electrons is

dependent on the scattering cross section of the atoms in the sample involved in the scattering. Some other low energy electrons emitted from the surface called secondary electrons. These electrons are excited out of the ground state of the atoms in the specimen via interaction with high-energy electron beam. The atomic number of the target sample, surface topography and energy of the incident electrons determine the number of secondary electrons. These secondary electrons are detected by the detector and is then amplified and converted into an electrical voltage. Another inelastic process occurs when excited electron is de-excited into ground state and X-ray photons are generated.

For imaging the sample surface, the incident electron beam scans over the surface and secondary electrons are collected by the detector in the specimen chamber. The signal from detector can be fed to a monitor. These provide the highest spatial resolution images, as they can only be excited from a near-surface layer of material and the signal comes from an area about the size of the electron probe. Since the electron-atom interaction mechanism in the scanning process, electrons or photons may be emitted which means that the detectors positioned above the sample are able to detect these escaping from sample surface. Therefore, some compositional contrast is also present.

The SEM images illustrated in this thesis are measured by the Vega Scanning Electron Microscope (as shown in Figure 3.5(a)). The Vega series is a family of high-quality, fully PC-controlled SEM. The unique four-lens electron optical column allows the optical system to be used in various modes, such as ‘field’, ‘depth’ mode et. The ‘resolution’ mode showing in the figure 3.5(b), which provides the highest resolution for the chosen working conditions, is selected in this thesis.

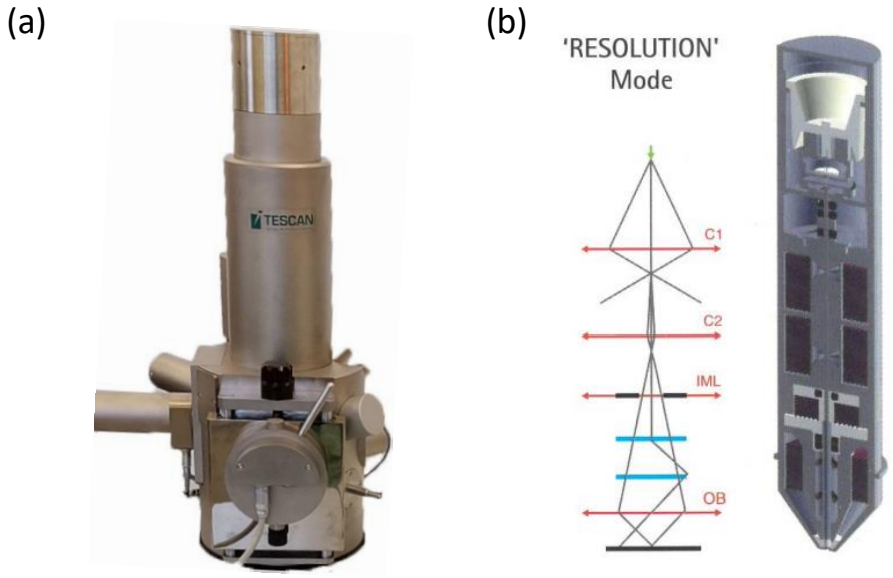

Figure 3.5 (a) Vega Scanning Electron Microscope used in this thesis. (b) Schematic diagram of ‘resolution’ mode.

The overview and specifications of Vega SEM

Resolution: 3.5nm (in high vacuum mode)

Working vacuum: $5 \times 10^{-3} Pa$

Pumping time after specimen exchange: 3 minutes
Magnification at 30kV/15mm: 20 to 500000x
Accelerating voltage: 500V to 30kV
Electron gun: Tungsten heated cathode
Probe current: 1pA to 2μA
Scanning speed: from 600ns to 10ms per pixel adjustable in steps or continuously
Image size: up to 4096*4096 pixels

The Y-shaped nanowires studied in this thesis were imaged by the high-resolution SEM. The SEM images provide clearer edges and more accurate scale of nanostructure.

3.2.3 Magneto-optical Kerr effect imaging system

Magnetic imaging at optical frequencies employs mainly the magneto-optical Kerr and Faraday effect. Both are rotational effects, that is, plane-polarized light is rotated on transmission through the transparent specimen (Faraday effect) or reflection from nontransparent specimen (Kerr effect). This rotation is converted into a domain contrast that can be amplified by digital image processing. Among all the observation methods, Kerr microscopy has unbeatable advantages due to the most versatile and flexible imaging characteristic. The sample investigated by MOKE imaging usually is allowed by coatings and no specific surface treatment. The relatively strength magnetic field can be directly applied to the sample, that making it possible to observe magnetization process and record magnetization loop simultaneously. The magnification can easily be varied by changing the microscope objective. The magnetization dynamic can also be studied within very small time interval via Time-resolved MOKE (TR-MOKE).

Depending on the orientation of the magnetization vector relative to the reflective surface and the plane of incidence of the light beam, three types of Kerr effect are distinguished: the polar, longitudinal, and transverse. The magnetization of sample is oriented perpendicularly to the reflective surface and parallel to the plane of incidence in the polar effect. For the longitudinal Kerr effect, a rotation of the plane of polarization occurs and an ellipticity appears when linearly polarized light reflects from a sample surface, provided that the magnetization lies both in the sample plane and in the plane of incidence of the light. The effect can be used to observe the domain structure of a material whose magnetization lies in the sample plane. The transverse effect can be only observed for absorbing materials. It is manifested as intensity variations and a phase shift of linearly polarized light reflected from a magnetized material, if the magnetization lies in the sample plane but is perpendicular to the plane of incidence of the light.

The wide-field Kerr microscopy is illustrated in figure 3.6. Light emitted from the LED lamp is focused onto the plane of the aperture diaphragm by the collector lens in front of lamp. The light passes through the opening of a variable field iris diaphragm and is then plane polarized and deflected downward into objective lens. After reflection from the sample, the light is captured by the objective lens and then reflected by beam splitter onto the other path. After passing the Analyzer, the beam enters the lens which

forms an intermediate image that is further processed toward the CCD. The field diaphragm is imaged on the specimen and therefore determines which part of the sample is illuminated. By adding a focus lens between the Beam splitter and Analyzer, the image in front of Objective lens is capture by the CCD camera which illustrated a 'Cross' showing in the figure 3.6. Therefore, controlling of aperture diaphragm, different incident angles can be selected to detect magnetic materials with different magnetization orientations.

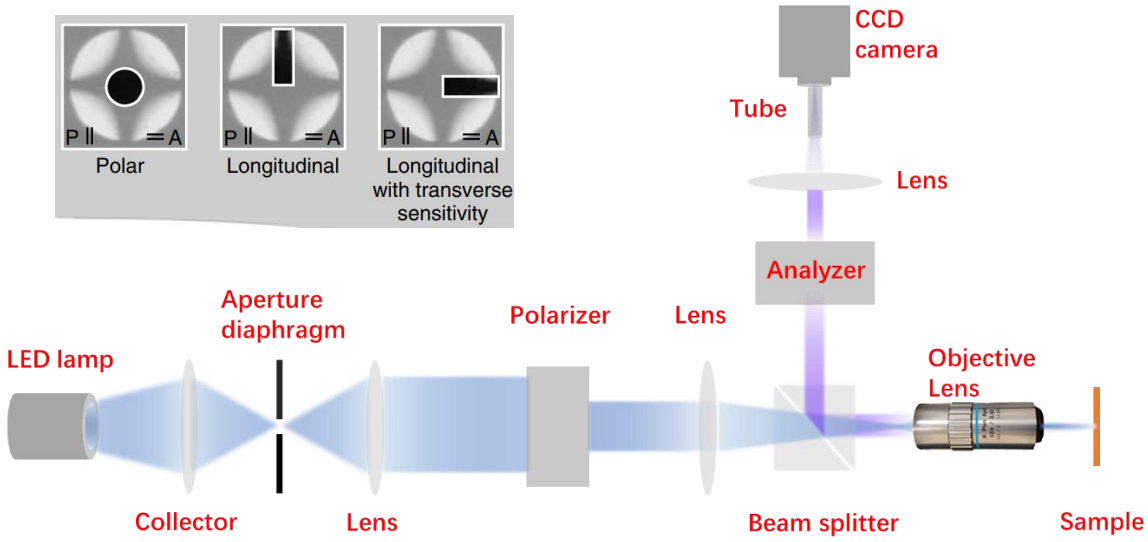

Figure 3.6 Illumination path for perpendicular light incidence. The blue light path and purple light path present the light incidence to the sample and refection from the sample. Different colors of light in the diagram are only used to distinguish different light path. The insert image is the extinction cross and aperture stop positions, observed in back focal plane. The aperture diaphragm can be viewed and adjusted to fulfill the requirements for the polar Kerr effect (centered iris diaphragm) or longitudinal effects (displaced slit diaphragm)[51].

The resolution of the MOKE images can be adjusted by changing different magnification objective lens. With high magnification objective lens, the details of domain structure and skyrmions can be observed. According to Rayleigh criterion, the smallest distance between two objects that can be resolved is given by $D = 0.5\lambda NA^{-1}$, where the λ is the wavelength of light and the NA is the numerical aperture which usual given by objective lens. In the thesis, the wavelength of led light is 465nm and NA is 0.55 (50x magnification). Therefore, using such an objective and blue light for illumination, domains as narrow as 422nm can be resolved. The contrast MOKE images proposed in this thesis was generated by dividing the two different initial state image (m_1) by the specific image (m_x) resulting in a magnetization distribution $\Delta m = m_1/m_x$. The initial state image was usual taken under saturated condition.

Wide-field Kerr microscopy is suitable for dynamic domain studies. The real-time domain structure evolution versus hysteresis loop can be captured by high-speed camera. The exposure time of CCD used in our MOKE setup can be as small as 0.1s.

Therefore, it can continuously and accurately reflect the dynamic relationship between the domain structure evolution and hysteresis loop, which cannot be achieved by other magnetic characterization methods. As First order reversal curves (FORCs) technique for example, most of previous research used VSM to realize the measurement of FORCs and domain structure evolution captured by MFM separately. However, those series of minor loops cannot directly connect magnetization process with corresponding domain evolution. Therefore, the magnetic characterization via Wide-field Kerr microscopy can reflect the relationship between magnetization and domain change accurately and in real time. It is an important and main magnetic characterization technique in this thesis.

3.3 Collaborating works' techniques

3.3.1 Electron-beam lithography

Electron Beam Lithography (EBL) is a powerful technique for creating nanostructures that are too small to fabricate with conventional photolithography. This nano-fabrication technique has two main advantages. First, it is possible to create nanostructures with dimensions below 10nm. The convenience of directly writing, patterns are created directly from CAD designs without a physical mask, enabling frequent, cost-free changes - ideal for optimizing, refining and prototyping designs.

The EBL, a process similar to photolithography, except that a focused beam of electrons is used to expose the resist, rather than photons. Complex geometrical patterns can be created by steering the beam across the surface of the sample. The electron beam lithography system used in this thesis is a Raith 50 system which is based on a SEM system with additional hardware and pattern generating software. The system can produce structures with a minimum feature size of around 50 nm.

The RAITH 50 consists of the following main subsystems:

- Digital controlled LaB6-based electron column
- SEM sub system and Windows NT user interface
- Pattern generation and PC based lithography user interface
- Vacuum chamber, clean vacuum system and plinth
- X-Y-Z fully automated laser interferometer controlled sample stage

All the nanofabrication mentioned in this thesis were done by Dr. Li Chen in Leeds University.

3.3.2 Transmission Electron Microscopy (TEM)

The transmission electron microscopy (TEM) is a microscopy technique which used

a beam of electrons instead of light to image the physical structure of ultra-thin films on an atomic scale. It consists in an electron emission source, electromagnetic lenses and an electron detector. The electron beam emitted from the source is accelerated and then focused on the sample by the lenses. The beam passes through the sample which modifies it and imprint its image, eventually magnified by other lenses and usually detected by fluorescence. The general layout is illustrated in figure 3.7.

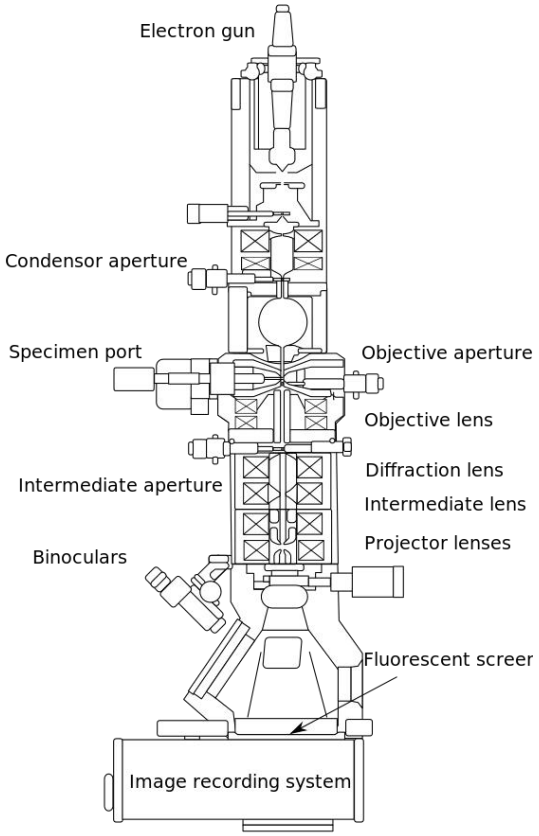

Figure 3.7 Layout of optical components in a basic TEM.[126]

One type of transmission electron microscopy is the Scanning Transmission Electron Microscope (STEM). The electron beam is focused on a specific point of the ultra-thin films rather than the whole surface. The transmitted beam is then detected, and a scanning of the surface allows to visualize the magnified image of the sample.

All the STME images in this thesis were measured by our collaborator Dr. Balati Kuerbanjiang in the York JEOL Nanocentre. The instrument JEOL 2200 FS is a 200kV Field Emission Transmission and Scanning Transmission Electron Microscope (TEM/STEM) with Cs Aberration Correctors for both TEM and STEM with 1 Å resolution, achieving single atom imaging sensitivity. This instrument is based on a JEOL 2200 FS TEM/STEM system with third order spherical aberration correctors for both TEM and STEM modes has been in-house modified with an open cell environmental chamber for dynamic in-situ experiments under operational conditions of controlled temperature (room temperature to 1100 C) in a gas environment (O_2, N_2 and H_2) with pressure up to 10 Pa.

The instrument is equipped with:

Thermo scientific 100mm^2 silicon drift EDX detector.
In column Omega type Electron Energy filter.
A High Angle Annular Dark Field (HAADF) STEM detector.
A Bright Field (BF) STEM detector.
In situ MEMS heating/biasing holders single and double tilt (DENS solution).
In situ heating liquid cell holder single tilt (Protochips).
In situ furnace heating single tilt holders (Gatan).
High dynamic range CCD ultrascan camera.
Fast frame acquisition Orius camera for dynamic TEM.
Turbo molecular pump vacuum system.
Wide gap HRP objective lens pole piece.
Remote operation.

In additional, the STEM images can be transferred into color mapping by using gwyddion processing.

3.3.3 Magnetic Force Microscopy (MFM)

Magnetic Force Microscopy is a variety of Atomic Force Microscopy (AFM), in which a sharp magnetized tip scans a magnetic sample. The interaction between the sample and tip are detected and used to reconstruct the magnetic structure of the sample surface. The schematic diagram of MFM is showing in the figure 3.8. The tip coating with a thin layer of magnetic material, experiences a measurable force when it enters the field gradient where a domain wall meets the sample surface. MFM requires minimal surface condition and can work on both conducting and insulating materials. This instrument can observe magnetic structures at extremely high resolution.

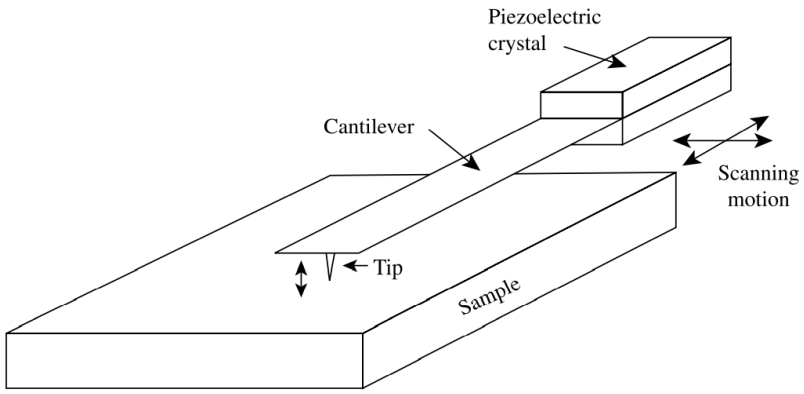

Figure 3.8 The schematic diagram of Magnetic Force Microscopy.

The MFM images illustrated in this thesis were measured by Dr. Kelvin Elphick

from department of electronics in York. The device picture is showing in the figure 3.9

The VLS-80 combines uniquely high vacuum SPM performance with high precision sample navigation. The new SPM scanner provides a scan range of 80 x 80 μm^2 with 20bit scanner resolution and allows for SPM analysis down from the nanometer up to the millimeter range. High resolution photo navigation in combination with the new high precision sample stage provides unique possibilities for sample navigation. The instrument can be operated under normal atmosphere condition or in high vacuum for maximum sensitivity in all dynamic SPM modes. The NanoScan controller system supports all standard SPM modes and also supports unique features such as tip protection and long-distance surface profiling. In additional, the image data processing was done by gwyddion[127].

Figure 3.9 The VLS-80 Magnetic Force Microscopy used in this thesis.

Part 2 Original work

Chapter 4-Defect-Correlated Skyrmions and Controllable Generation in Perpendicularly Magnetized CoFeB Ultrathin Films

4.1 Introduction

Skyrmions have attracted significant interest due to their topological spin structures and fascinating physical features. The investigation of defect-correlated skyrmions by induced local defects has been introduced in the chapter 2, however, the inhomogeneous distribution caused by the sample deposited has not been investigated. Moreover, the research on the density of skymions under external field remains problem. Although skyrmions have been demonstrated experimentally, the general critical intrinsic relationship between fabrication, microstructures, magnetization and the existence of skyrmions remains to be established.

Here, two series of CoFeB ultrathin films with controlled atomic scale structures are employed to reveal this relationship. The amount of defects was artificially tunned by inverting growth order, and skyrmions shown to be preferentially formed in samples with more defects. By utilizing first-order reversal curves, the stable region and the skyrmion densities can be controlled efficiently in the return magnetization loops. These findings establish a general internal link from sample preparation to skyrmion generation and provide a general method for controlling skyrmion density.

All the simulation results were completed by Dr. Junlin Wang. The discussion of theoretical part was assisted by Prof. Roy W. Chantrell and Prof. Haihong Yin. All the STEM images were taken by Dr. Balati Kuerbanjiang.

4.2 Sample preparation

To investigate the relationship between material features, magnetization characteristics and magnetic skyrmions, two series of CoFeB ultrathin films with inverted growth order are fabricated. Substrate/Ta(5)/MgO(3)/CoFeB(t)/Ta(5) (from the bottom, layer thickness in nm) samples were deposited on thermally oxidized Si wafers (100) using magnetron sputtering system at RT with base pressure better than 5×10^{-5} Torr. To obtain flat surface morphology, the working pressure during

sputtering was kept low at about 3.3×10^{-1} Torr in Ar atmosphere. In the fabrication, metallic layers (Ta) were deposited by dc magnetron sputtering, while MgO and CoFeB layers were deposited by RF magnetron sputtering. A Ta capping layer of 5nm thickness was deposited to protect the films against oxidation. Because the PMA originates from the Fe-O hybridization and B accumulation at interface, which only exists with a very small layer thickness range, thus the thickness of the CoFeB (0.8-3 nm) layer was varied across the films studied in this work. Finally, the deposited films were annealed in a high vacuum furnace chamber at 300 ºC for 30 min. The same sputtering method was used to prepare substrate/Ta(5)/CoFeB(t)/MgO(3)/Ta(5) ultrathin films. The thickness of the CoFeB layer is also varied from 0.8 nm to 3 nm to obtain PMA ultrathin films.

4.3 Defect-correlated magnetization and skyrmion generation

4.3.1 Magnetization investigated based on MOKE imaging

Here, substrate/Ta/MgO/CoFeB/Ta ultrathin films with PMA are chosen for investigation [Figure 4.1(a)] by virtue of the large skyrmion size ($\sim$1 μm) at room temperature [91, 99, 104, 111, 128], which can be easily monitored utilizing a polar magneto-optical Kerr effect (MOKE) microscope[91, 99, 104, 111]. In the overwhelming majority CoFeB ultrathin films with reported skyrmions, the same growth order of sputtering Ta on CoFeB is used to generate the skyrmion. In studies reported by Yu et al.[111] and Zázvorka et al.[128], an ultrathin Ta interlayer was purposefully introduced between CoFeB and MgO layers, which was interpreted as playing a critical role in tuning the PMA by the weakening the Fe−O bonds at the interface[129]. Another possibility, however, comes from the detail of the preparation process. In the sputtering processes: a common MgO/CoFeB/Ta multilayers preparation technique, it is important to note that Ta atoms have relatively high momentum due to their large atomic number Z. Since neutron, proton or heavy ion irradiation can create a large amount of defects in irradiated metallic materials[130], it is expected that more defects should be induced at CoFeB/Ta interface by sputtering Ta as a capping layer. In contrast, it follows that if the growth order is inverted, the interfacial defect density should be far lower. In this work, two series of MgO/CoFeB/Ta ultrathin films with different growth order are employed to investigate the influence of defect

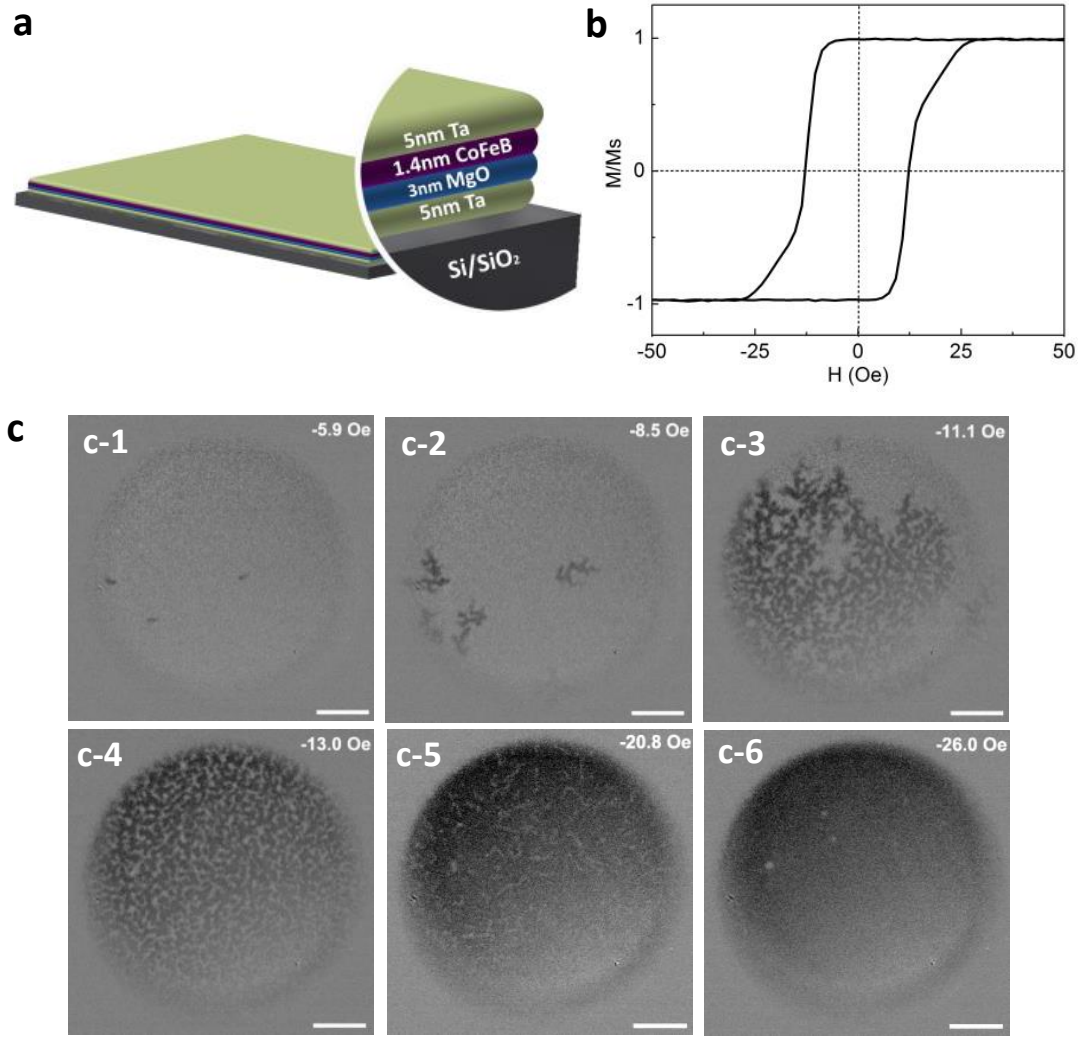

Figure 4.1 Sample structure and magnetization reversal. a-c, Structure schematic (a), out-of-plane Kerr hysteresis loop (b), and MOKE images (c) for substrate/Ta(5)/MgO(3)/CoFeB(1.4)/Ta(5). The MOKE images, which circle field of view, are acquired by changing the out-of-plane field strength after the initial positive field saturation. The dark(white) presents the magnetization point out(in) of plane. The scale bar is 20 μm.

Figure 4.1b shows a Kerr hysteresis loop with symmetric rounded loops, indicating multiple evolution states during magnetization. Figure 4.1c shows the domain evolution in substrate/Ta(5)/MgO(3)/CoFeB(1.4)/Ta(5) (in nm) film under an out-of-plane field. The magnetization exhibits a typical nucleation reversal process, including the four stages of nucleation (Figure 4.1c-1), expansion from nuclei (Figure 4.1c-2 and c-3), domain expansion (Figure 4.1c-4 and c-5) and reversal of hard entities (Figure 4.1c-6). The nucleation-dominated reversal is attributed to the inhomogeneous film. Local defects give rise to a broad inhomogeneous distribution of energy barriers, which promote nucleation-dominated reversal in the sample, thereby generating local magnetic entities with varying coercivity. Several bubble-like magnetization

configurations firstly emerge at low applied fields (Figure 4.1c-1), nucleated at local entities with low coercivity (called “easy centers” here). The increasing applied field accelerates the domain growth, and the magnetization configurations transform to a labyrinth phase (Figure 4.1c-4). Then the domain wall expands with increasing field and the labyrinth phase transforms to stripe domains (Figure 4.1c-5). When the field approaches close to the saturation, the stripe domains are reversed gradually, condense at local entities with a high coercivity (called “hard centers” here), and transform to bubble-like magnetization configurations **(**Figure 4.1c-6). Eventually, when the external magnetic field is large enough, the magnetic bubbles are thoroughly reversed.

We have further carried out two series of comparative magnetization tests for both substrate/Ta(5)/MgO(3)/CoFeB(t)/Ta(5) and substrate/Ta(5)/CoFeB(t)/MgO(3)/Ta(5) (Figure 4.2a) specimens. Perpendicular substrate/Ta(5)/MgO(3)/CoFeB(t)/Ta(5) samples with different CoFeB thickness show similar nucleation reversal process; however, a fast domain-wall propagation are observed in the magnetization reversal of substrate/Ta(5)/CoFeB(t)/MgO(3)/Ta(5) specimens (Figure 4.2b and c).

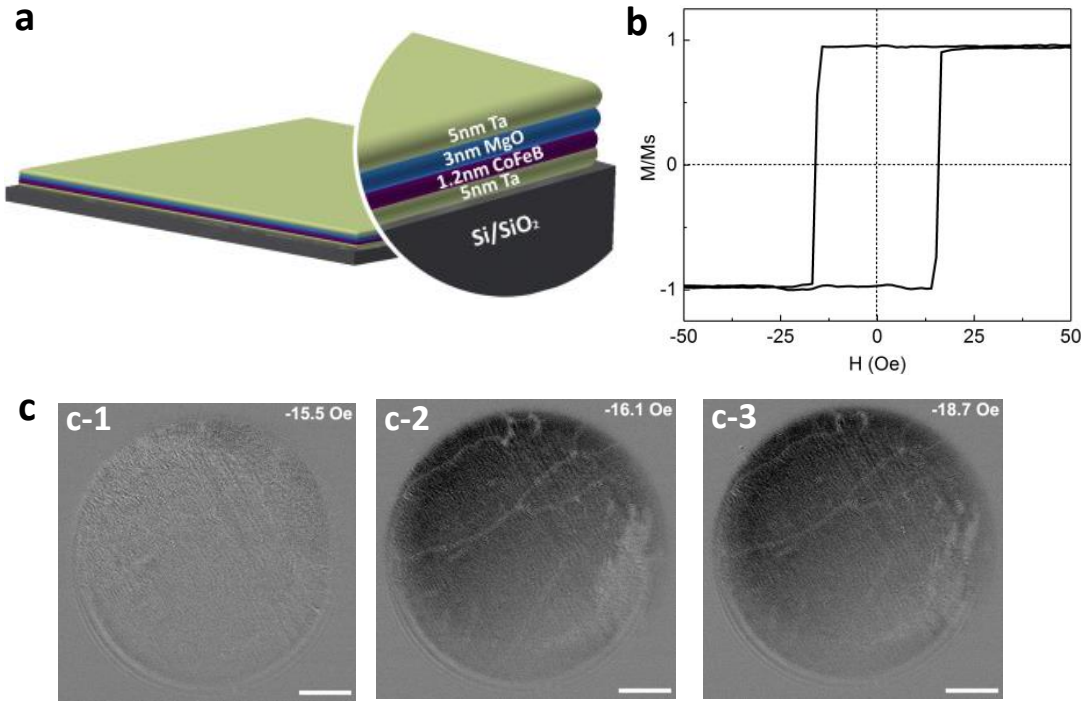

Figure 4.2 Sample structure and magnetization reversal. a-c, Structure schematic (a), out-of-plane Kerr hysteresis loop (b), and MOKE images (c) for substrate/Ta(5)/CoFeB(1.2)/MgO(3)/Ta(5). The MOKE images are acquired by changing the out-of-plane field strength after the initial positive field saturation. The dark(white) presents the magnetization point out(in) of plane. The scale bar is 20 μm.

The magnetic skyrmions can only observed in substrate/Ta(5)/MgO(3)/CoFeB(t)/Ta(5) specimens, rather than in substrate/Ta(5)/CoFeB(t)/MgO(3)/Ta(5) specimens according to our experiments. The vastly different findings can be interpreted by their distinct material features. Specimens in this work are all prepared by the sputtering technique, in which Ta atom

has relative high momentum due to high Z. Thus, by sputtering Ta layer on bottom CoFeB/MgO, the Ta atomic bombardment would induce more defects.

4.3.2 Single skyrmion captured by magnetic force microscopy

A single pass magnetic force microscopy (MFM) mode was selected[131] in this case to image the nucleation of skyrmions. The sample Ta(5)/MgO(3)/CoFeB(1.4)/Ta(5) was fixed on a MFM scanning stage by conductive adhesive under base pressure of $3 \times 10^{-6}\, Torr$, the sample was initially saturated at 100mT and individual skyrmion was imaged at a reversed 2.5mT magnetic field. Figure 4.3a shows an upper bound for the skyrmion diameter, which is given by the FWHM (Full Width at Half Maximum) of the corresponding gaussian profile : ~300 nm (measured by the black linescan shown in Figure 4.3a) for single magnetic skyrmions, whose out-of-plane magnetic moment component is shown in frequency shift data mapping[132]. These skyrmion bubbles are quite stable even in the close to saturating external field during the MFM measurements[131].

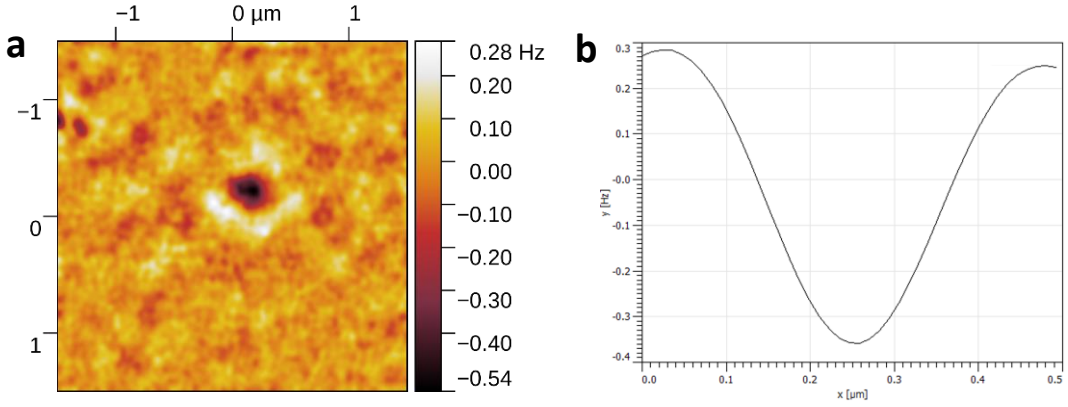

Figure 4.3 Observation and analysis of magnetic skyrmions. Magnetic force microscopy (MFM) imaging of individual skyrmions in single pass MFM mode. a Skyrmions is imaged by frequency shift data mapping under an applied perpendicular field $H_z = 2.5mT$. The black line in the skyrmion image is the linescan across which the skyrmion size is measured shown in the b.

4.3.3 Determination of DMI strength

4.3.3.1 DMI strength estimation from domain width

We determine the DM interaction strength in substrate/Ta(5)/MgO(3)/CoFeB(1.4)/Ta(5) ultrathin films using the well-known domain spacing model[92, 99, 100, 111]. The domain width as a function of applied

external magnetic field (out of plane in our experiment). When applied a high external magnetic field, the domain opposite to the field will disappear. The experimental result is shown in Figure 4.4b, and the domain up (d_{up}), domain down (d_{down}), periodicity (d_{aver}) are representing the black/white and black+white in images respectively. The domain width terminated with the changing external magnetic field was fitted by the function $\mathrm{D}(x) = a \cdot tanh(\omega \cdot x + \varphi) + b$, which can be used to describe a hysteresis loop[92]. For periodic stripe domains in thin film, the low-field domain period $d_{aver} = d_{up} + d_{down}$ is given by[49]

$$\frac{\sigma_{DW}}{\mu_0 M_s^2 t} = \frac{{d_{aver}}^2}{t^2} \sum_{odd\ n=1}^{\infty} \frac{1}{(\pi n)^3} \left[1 - \left(1 - \frac{2\pi n t}{d_{aver}}\right) \exp\left(-\frac{2\pi n t}{d_{aver}}\right)\right] \tag{4.1}$$

At the high field, the terminal width can be extracted from the fitting function as $d_{min} = |b - a|$ given by

$$\frac{\sigma_{DW}}{\mu_0 M_s^2 t} = In\left[1 + \left(\frac{d_{min}}{t}\right)^2\right] + \left(\frac{d_{min}}{t}\right)^2 In\left[1 + \left(\frac{d_{min}}{t}\right)^{-2}\right] \tag{4.2}$$

The DW energy is also known as

$$\sigma_{DW} = 4\sqrt{AK_{eff}} - \pi|D| \tag{4.3}$$

Here, σ_{DW} is the DW energy, M_s the saturation magnetization, *t* the thickness of the film, *A* the exchange constant, and K_{eff} the effective uniaxial anisotropy. The high DMI constant favours small chiral skyrmions.

As a result of the fitting, the $d_{aver} = 2.02 \pm 0.20\ \mu m$, $d_{min} = 0.5 \pm 0.05\ \mu m$. Since domain width has a strong dependence on the external H-field shown in Figure 4.4, to have a consistent analysis, we use the terminal domain width for the σ_{DW} calculation, where domain witdh is saturated. Therefore, the DMI constant was estimated $|\mathrm{D}| = 0.35 \pm 0.02\ mJ/m^2$.

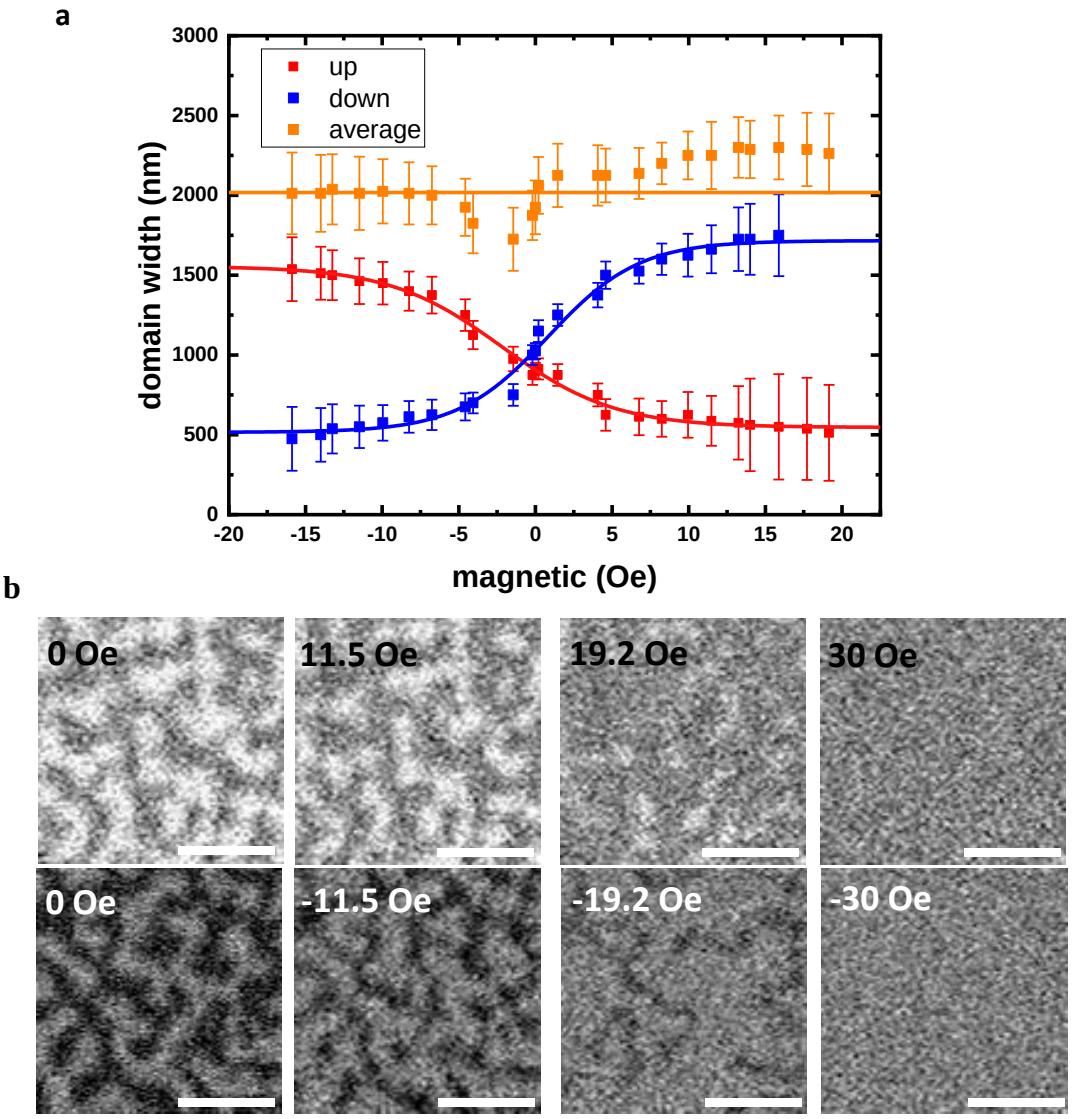

Figure 4.4 DMI strength estimation using the domain spacing model. a, Domain width as a function of external magnetic field. The line showing in the diagram were carried our using the fitting function $D(x) = a \cdot tanh(\omega \cdot x + \varphi) + b$. *The scale bar is 5 μm. Error bars are given by the standard deviation of the stripe domain width. b, The domain width evolution under an increasing positive/negative magnetic field. The dark(white) presents the magnetization point out(in) of plane.*

In previous works on Ta/CoFeB/metal-oxides thin films [91, 99, 104, 111], the interfacial DM interaction and the generation of magnetic skyrmions have been confirmed. Here, the magnitude of the interfacial DM interaction is estimated to be 0.35 ± 0.02 mJ/m^2 in our sample. The interfacial DM interaction competes with SOC, induces and stabilizes Néel-type chiral domain walls in the substrate/Ta(5)/MgO(3)/CoFeB(1.4)/Ta(5) film.

4.3.3.2 Micromagnetic Simulation of the Domain Spacing to Determine DMI Strength

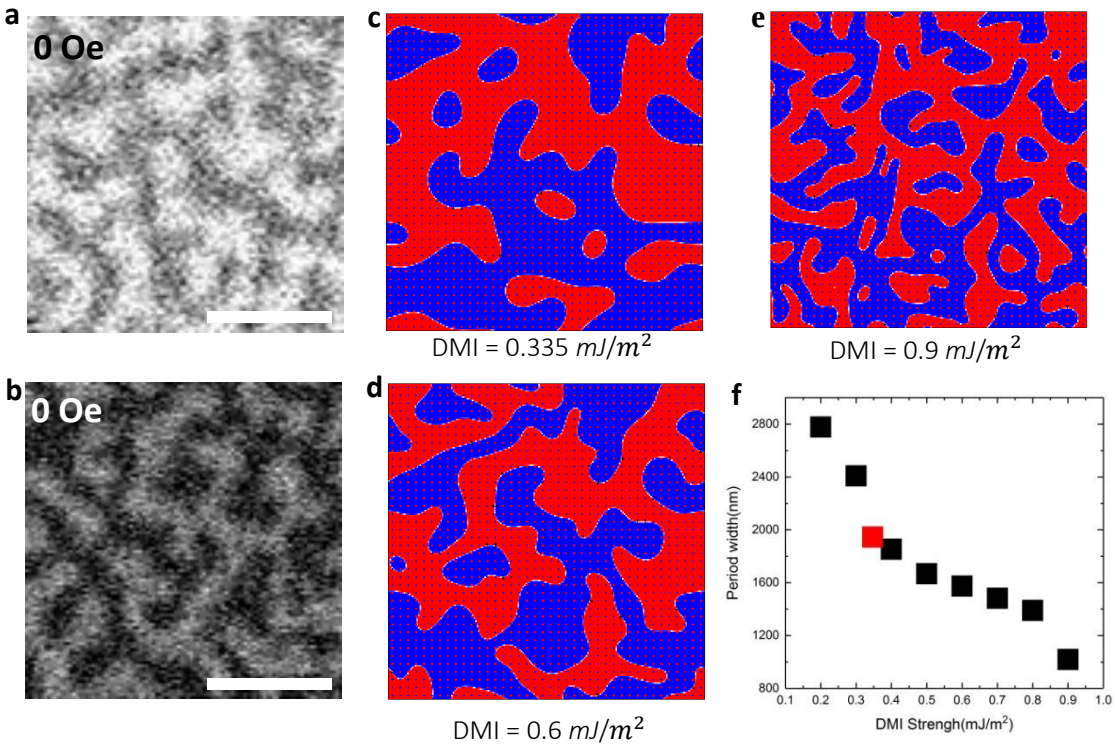

Figure 4.5 Simulation of the domain spacing in substrate/Ta(5)/MgO(3)/CoFeB(1.4)/Ta(5) versus DMI. a-b, Domain structure at 0 Oe when no external field is applied. The scale bar is 5 μm. c-e, The results of the micromagnetic simulations showing a varying domain width for different values of the DMI. f, Relationship between the domain period width and the DMI strength. The simulation result is consistent with the DMI estimated by the domain spacing model.

The calculated DMI strength given in the previous subsection is confirmed using full micromagnetic simulations of the domain spacing as a function of DMI. The simulation is performed using the numerical package of the Mumax3[133]. The parameters for the micromagnetic simulation are from the experiment measurement: the saturation magnetization $M_s = 874\ kA/m$ and the perpendicular magnetic anisotropy $K_u = 0.1312\ MJ/m^3$. The parameter exchange constant $A = 10\ pJ/m$. The range of the DMI strength is adjusted from $0.2\ mJ/m^2$ to $1.0\ mJ/m^2$. The simulation model is a $10\ \mu m \times 10\ \mu m \times 1.2\ nm$ ferromagnetic thin film with a periodic boundary condition.

From Figure 4.5a - c, the measured magnetization distribution is good agreement with the simulation results. The domain widths obtained from experiments and simulations are very close, which indicates the simulation model can verify the experiment results. In addition, the period width of the strip domain is inversely

proportional to the DMI strength which has been shown in Figure 4.5c-d. With the DMI strength increasing, the period width of the strip domain decreases to a small size. The trend of between the varied DMI strength and the period width of strip domain is given in Figure 4.5f, the result of DMI strength is about $0.335\ mJ/m^2$ marked as a red square.

4.3.4 Magnetic characterization of CoFeB ultrathin films

4.3.4.1 Magnetization Curves for Two Series of CoFeB Ultrathin Films

The magnetization curves are measured by vibrating sample magnetometer (VSM). For substrate/Ta(5)/MgO(3)/CoFeB(t)/Ta(5) ultrathin films with t=0.8 and 1.0 nm, no signature VSM signal is detected due to tiny amounts of CoFeB. When t increases to 1.2 nm, the magnetic hysteresis loops show a low perpendicular anisotropy as shown in Figure 4.6a. With t increasing to 1.3 and 1.4 nm, both samples show better perpendicular anisotropy compared to the sample with t = 1.2 nm (Figure 4.6b and c). When t further increases to 1.6, 1.8, 2.0 and 3.0 nm, the samples exhibit in-plane magnetic anisotropy.

For substrate/Ta(5)/CoFeB(t)/MgO(3)/Ta(5) ultrathin film with t=0.8 nm, no signature VSM signal are detected. With t increasing to 1.0 and 1.2 nm, both samples show high perpendicular anisotropy (Figure 4.6d and e). When t further increases larger, the samples exhibit in-plane magnetic anisotropy.

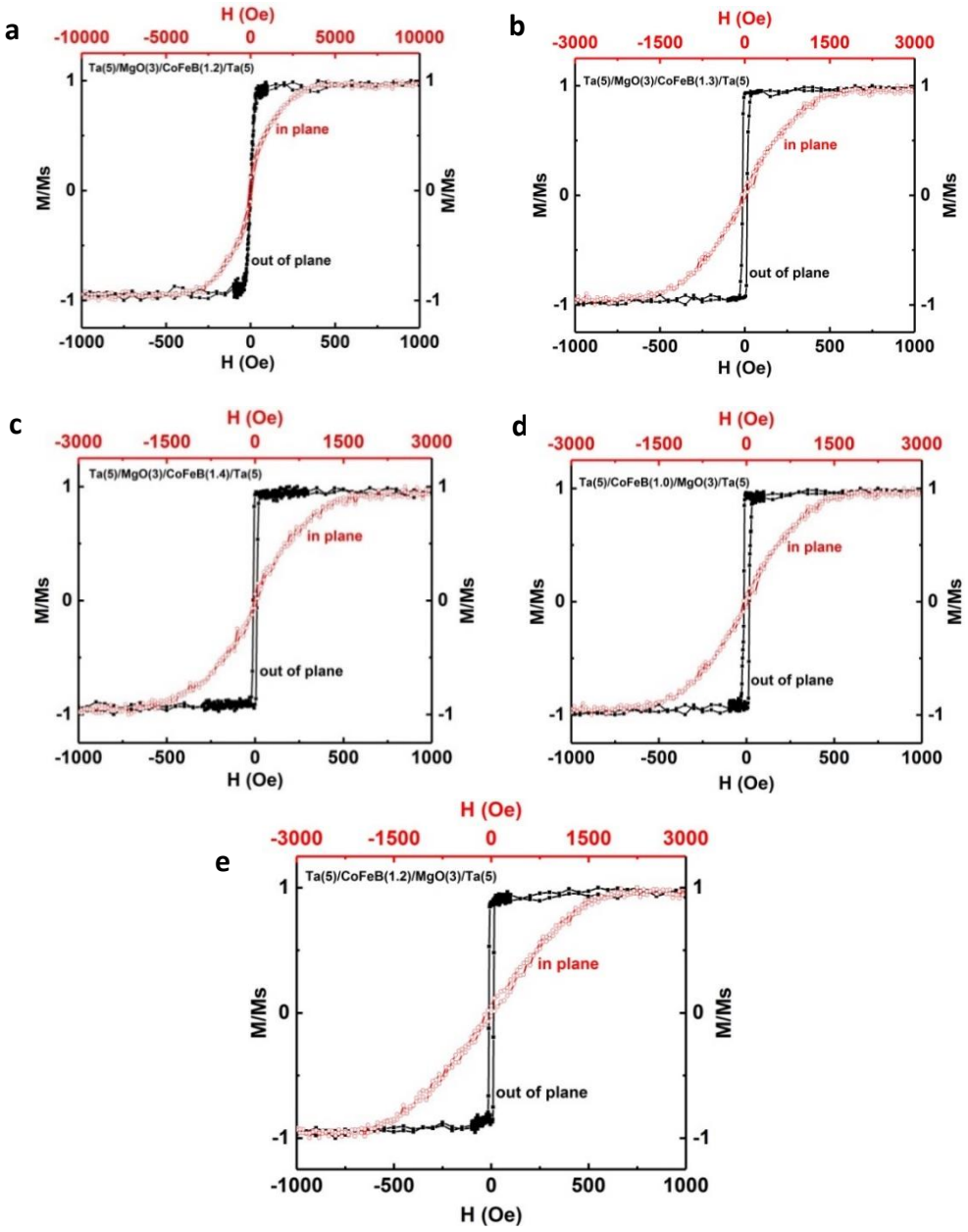

Figure 4.6 Magnetization curves for CoFeB ultrathin films. a-c, In-plane and out-of-plane hysteresis loops for substrate/Ta(5)/MgO(3)/CoFeB(t)/Ta(5) samples with the CoFeB thickness (t) is equal to 1.2 nm (a), 1.3 nm (b) and 1.4 nm (c). substrate/Ta(5)/MgO(3)/CoFeB(1.2)/Ta(5), d-e, In-plane and out-of-plane hysteresis loops for substrate/Ta(5)/CoFeB(t)/MgO(3)/Ta(5) samples with the CoFeB thickness (t) is equal to 1.0 nm (d) and 1.2 nm (e).

4.3.4.2 Magnetization Reversal of CoFeB Ultrathin Films

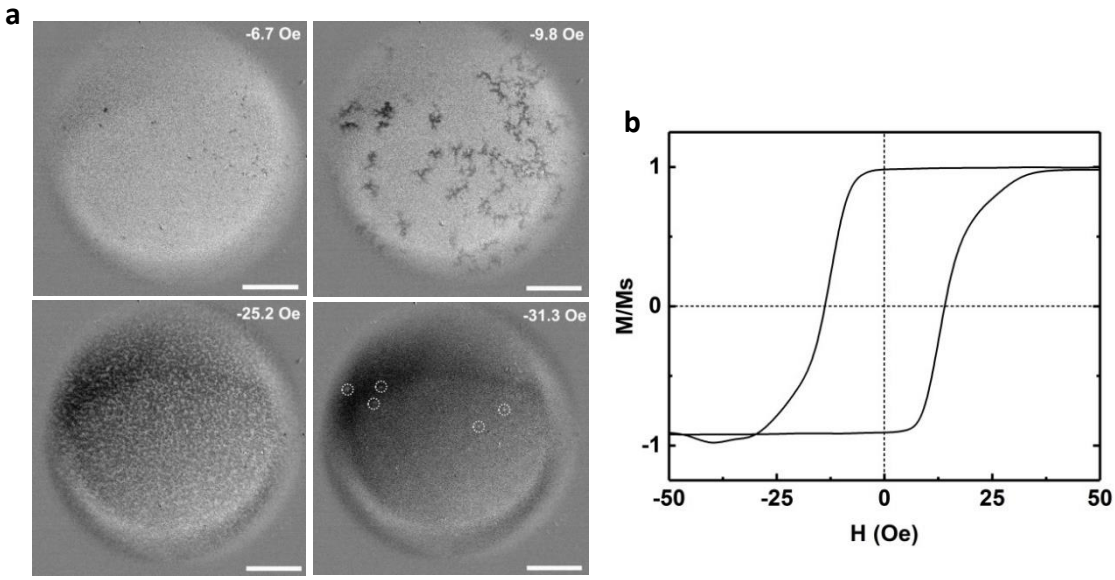

Figure 4.7 Magnetization reversal of the substrate/Ta(5)/MgO(3)/CoFeB(1.3)/Ta(5) sample. a, MOKE images acquired for several out-of-plane fields after positive field saturation. b, The out-of-plane Kerr hysteresis loop with magnetization (M) normalized to the saturation magnetization (Ms). The dark(white) presents the magnetization point out(in) of plane. The scale bar is 20 μm.

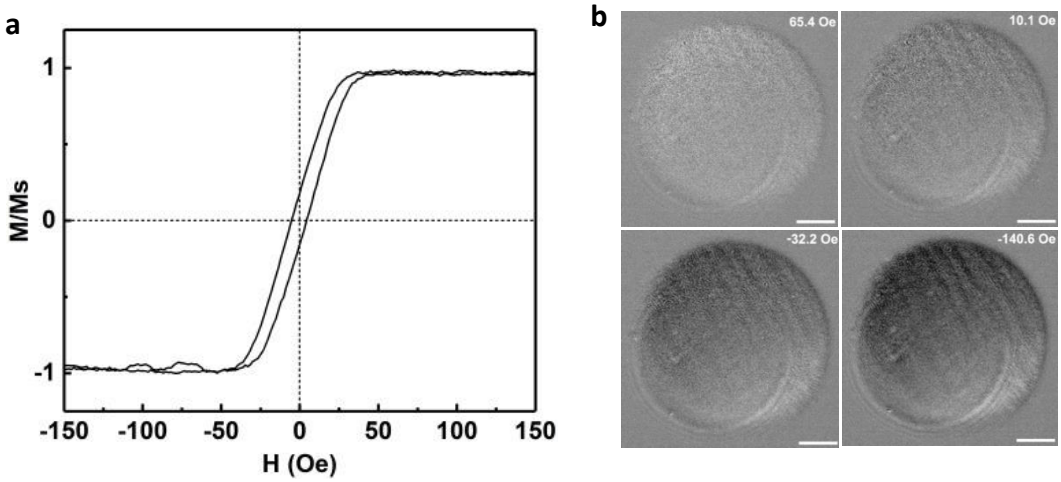

Figure 4.8 Magnetization reversal of the substrate/Ta(5)/MgO(3)/CoFeB(1.2)/Ta(5) sample. a, The out-of-plane Kerr hysteresis loop with magnetization (M) normalized to the saturation magnetization (Ms). b, MOKE images acquired for several out-of-plane fields after positive field saturation. The dark(white) presents the magnetization point out(in) of plane. The scale bar is 20 μm.

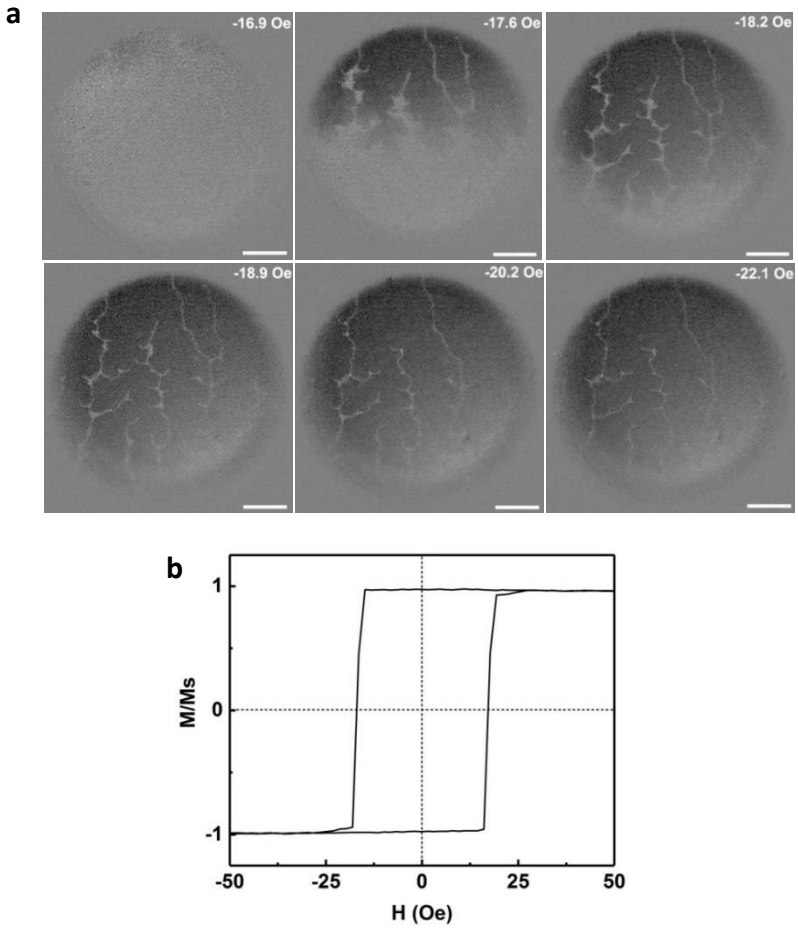

Figure 4.9 Magnetization reversal of the substrate/Ta(5)/CoFeB(1.0)/MgO(3)/Ta(5) sample. a, MOKE images acquired for several out-of-plane fields after positive field saturation. b, The out-of-plane Kerr hysteresis loop with magnetization (M) normalized to the saturation magnetization (Ms). The dark(white) presents the magnetization point out(in) of plane. The scale bar is 20 μm.

In all CoFeB ultrathin films, three different mechanisms (nucleation, rotation and wall propagation) of magnetization reversal are observed in the MOKE imaging investigation. For substrate/Ta(5)/MgO(3)/CoFeB(t)/Ta(5) films with PMA, both samples with t = 1.3 and 1.4 nm show similar nucleation-dominated reversal processes (Figure 4.1b-c and Figure 4.7), which can be attributed to the inhomogeneous distribution of energy barriers caused by the sputtering-induced defects as analyzed in the main text. However, although the sample with t = 1.2 nm also shows an out-of-plane anisotropy, a lower perpendicular anisotropy is observed (Figure 4.8a), and the sample exhibits a rotation reversal behavior in the magnetization process. The corresponding MOKE images in Figure 4.8b show a continuous contrast evolution, indicating no multidomains but uniform domains are observed in the whole reversal process.

For substrate/Ta(5)/CoFeB(t)/MgO(3)/Ta(5) films with PMA, the samples with t = 1.0 and 1.2 nm show similar wall-propagation reversal process (Figure 4.2c and Figure 4.9). A reversed domain is first formed at the edge, and a small increase of H triggers a large wall rapidly jumping through the film. Following with domain expansion and the

final reversal of hard magnetic entities, the reversal process is finally completed. It is clear that the magnetization is a wall-propagation-dominated switching process, in which the domain nucleation is a rare event. This reversal behavior is typical for homogeneous and continuous magnetic film, revealing a relative low density of defects in substrate/Ta(5)/CoFeB(t)/MgO(3)/Ta(5) samples.

The investigation of the two series of CoFeB ultrathin films indicates that only samples with nucleation-dominated reversal can generate magnetic skyrmions. The interstate formation in the magnetization reversal will result in a curved hysteresis loop, thus it is certain that the sample which can generate magnetic skyrmions will display a curved hysteresis loop. This rule can also be indirectly confirmed in previous works[100, 104, 111, 113, 114]. In this work, only samples of substrate/Ta(5)/MgO(3)/CoFeB(t)/Ta(5) with t = 1.3 and 1.4 nm have curved hysteresis loops and can generate magnetic skyrmions.

4.3.4.3 Magnetic properties summary of samples

All samples of two series of substrate/Ta(5)/MgO(3)/CoFeB(t)/Ta(5) and substrate/Ta(5)/CoFeB(t)/MgO(3)/Ta(5) are listed in Table 4.1. When the CoFeB layer thickness is equal to 1.2, 1.3 and 1.4 nm, respectively, substrate/Ta(5)/MgO(3)/CoFeB(t)/Ta(5) ultrathin films show out-of-plane anisotropy, while substrate/Ta(5)/CoFeB(t)/MgO(3)/Ta(5) samples exhibit out-of-plane anisotropy when t = 1.0 and 1.2 nm. It is noted that different thickness range of the CoFeB layer is required for the two series of samples to generate perpendicular anisotropy. This is owing to different degrees of nanocrystallizaiton and the intermixing at Ta/CoFeB interfaces during sputtering. H_a is the saturation magnetic field of hard magnetization axis. The red box shows the samples can be observed skyrmions generation.

Table 4.1 Sample list of CoFeB ultrathin films.

substrate/Ta(5)/MgO(3)/CoFeB(t)/Ta(5)				
Thickness(nm)	t=1.2	t=1.3	t=1.4	t=1.6
Easy axis	out of Plane	out of Plane	out of Plane	In plane
Hysteresis loop	Curved loop	Rounded loop	Rounded loop	In plane
Mangetization	Rotation	Nucleation	Nucleation	
Skyrmion	No	Yes	Yes	
Ms(emu/cc)	510	829	874	714
Ha(Oe)	5000	3000	3000	4000
Ku(MJ/m^3)	0.1275	0.1244	0.1312	-0.1429
DMI(mJ/m^2)		0.31	0.35	
substrate/Ta(5)/CoFeB(t)/MgO(3)/Ta(5)				
Thickness(nm)	t=1.0	t=1.2	t=1.4	
Easy axis	out of Plane	out of Plane	In plane	
Hysteresis loop	Quasi-square	Quasi-square	In plane	
Mangetization	Wall progagation	Wall propagation		
Skyrmion	No	No		
Ms(emu/cc)	1105	1156	1020	
Ha(Oe)	3000	3000	3500	
Ku(MJ/m^3)	0.1658	0.1735	-0.1786	
DMI(mJ/m^2)				

4.3.5 STEM analysis of CoFeB ultrathin films

To data, CoFeB ultrathin films are commonly prepared by the sputtering technique. In sputtering processes, Ta atom has relative high momentum due to high Z, thus one conceivable strategy to increase the amount of defects in CoFeB ultrathin films is reversing the growth order. By sputtering Ta layer on CoFeB/MgO, the Ta atomic bombardment would increase the intermixing degree at Ta/CoFeB interface, inducing

more defects. To confirm our exception, STEM investigation for samples of substrate/Ta(5)/MgO(3)/CoFeB(1.4)/Ta(5) and substrate/Ta(5)/CoFeB(1.2)/MgO(3)/Ta(5) is performed.

As shown in Figure 4.10, the cross-sectional STEM images show clear stack layers with the designed thickness. The 3 nm thick MgO shows clear and sharp interfaces with the CoFeB layer of both samples, while the Ta/CoFeB interface is unclear. The corresponding STEM investigation indicates the Ta/CoFeB interface in Figure 4.10a is more indistinct than that in Figure 4.10b, and there is a clearer distinction in the color mapping as shown in figure 4.10 c and d, confirming higher intermixing degree at Ta/CoFeB interface of substrate/Ta(5)/MgO(3)/CoFeB(1.4)/Ta(5). Our investigation is consistent with the previous studies which found that the sputtering will increase the interface roughness and form a magnetic dead layer[134, 135]. Meanwhile, it is noted that the CoFeB layer in substrate/Ta(5)/MgO(3)/CoFeB(1.4)/Ta(5) is semi-crystalline with some local crystalline CoFeB grains about 1–2 nm are formed (Figure 4.10a), while the CoFeB layer in substrate/Ta(5)/CoFeB(1.2)/MgO(3)/Ta(5) is amorphous (Figure 4.10b). Therefore, the Ta atomic bombardment and the local nanocrystallization can both induce more structural defects, resulting in an inhomogeneous CoFeB layer. In the overwhelming majority of literature reports, the same sputtering of Ta on CoFeB layer was adopted for skyrmion generation in Ta/CoFeB/metal-oxides ultrathin films [91, 99, 104, 111]. As skyrmions favor nucleation at a certain location as also observed by Jakub Zázvorka et. in similar sample specimen[106], this phenomenon supports our hypothesis about defect-correlated skyrmion generation. The sputtering- and naocrystallization-induced defects give rise to the inhomogeneous distribution of energy barriers. Consequently, magnetic skyrmions emerge preferentially in the sample with more defects, generating skyrmions with opposite magnetization sign as shown in Figure 4.1c-1 and c-6.

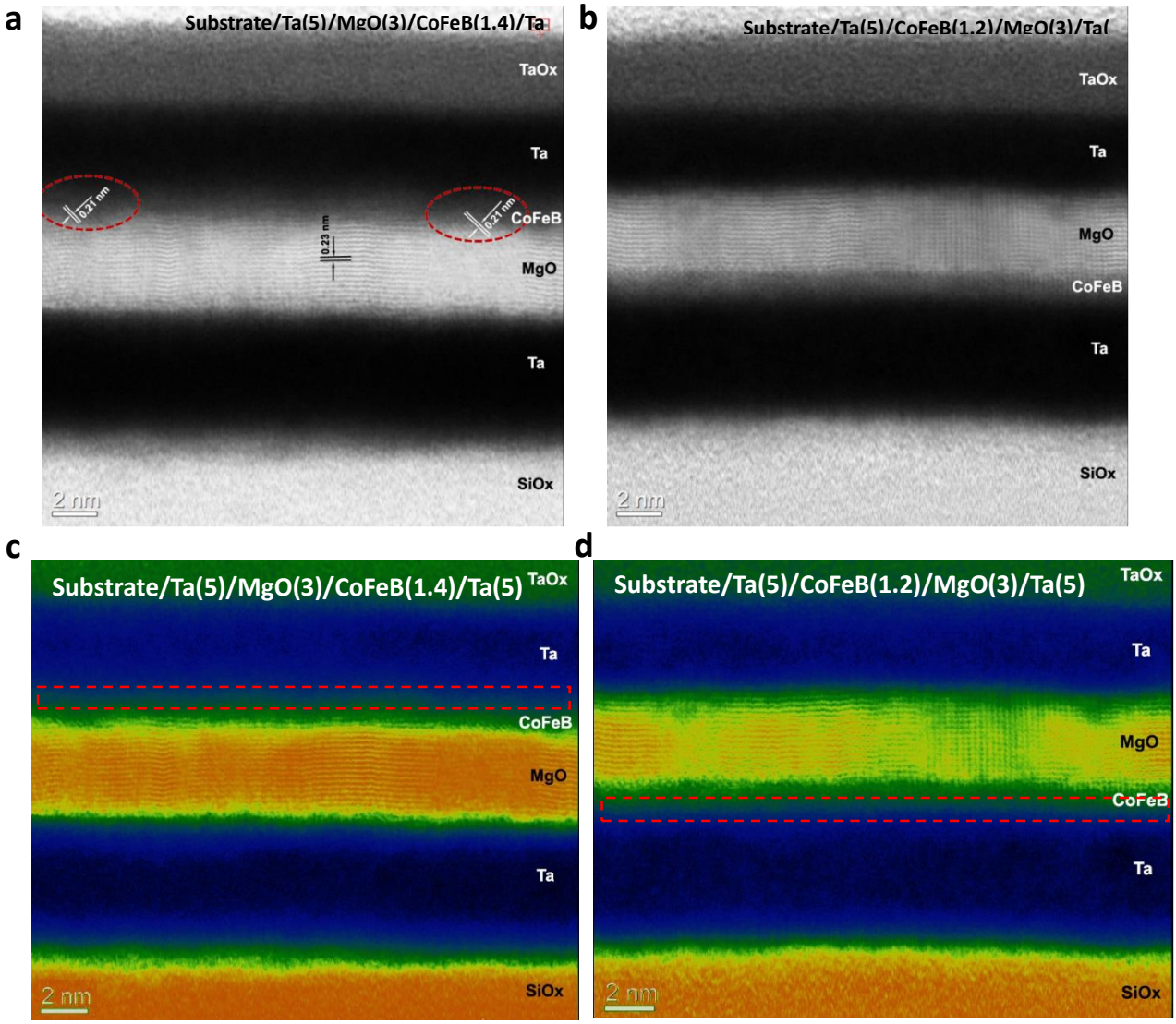

Figure 4.10 STEM images of CoFeB ultrathin films. a-b, STEM images for substrate/Ta(5)/MgO(3)/CoFeB(1.4)/Ta(5) and substrate/Ta(5)/CoFeB(1.2)/MgO(3)/Ta(5), respectively. The corresponding color mapping of STEM images of CoFeB are showing in c, d. The Ta/CoFeB interface in plane a is more indistinct than that in plane b or d, confirming higher sputtering-induced intermixing degree at Ta/CoFeB interfaces.

4.3.6 Atomistic simulation

For a deeper understanding of defect-correlated magnetization and skyrmion generation, a simulation based on an atomistic spin model was performed to investigate the influence of sputtering-induced defects on the magnetic anisotropy.

The atomistic simulation in this work is performed using the simulation package of *Vampire 5* [136]. The energy of the system is described by the following Hamiltonian, which include all the energy contribution to the magnetic behavior of the system, including the Heisenberg form of exchange:

$$\mathrm{H} = -\sum_{i<j} J_{ij}\overrightarrow{S_i}\cdot\overrightarrow{S_j} - \sum_i k_u^i\left(\overrightarrow{S_i}\cdot\hat{e}\right) - \mu_0\sum_i \mu_S^i\overrightarrow{S_i}\cdot\overrightarrow{H_{app}} + H_{demag}, \qquad (4.4)$$

where the J_{ij} is the exchange interaction between the spins on site i and j, K_u is the uniaxial anisotropy energy on site i along the axis $\hat{e}$, μ_S^i is the atomic spin moment on the atomic site i in unit of μ_B and μ_0 is the permeability constant. The parameters in this equation can be measured by the experiment or calculated by ab initio density functional theory (DFT) calculations.

The atomistic simulation model in this work has been considered as the magnetic anisotropy of CoFeB thin film is provided by the monolayer atom at CoFeB-MgO interface and is guided by previous first-principles calculations [137]. The magnetic properties of the different element Co, Fe, B has been considered as an average magnetic with high anisotropy (For interface) and zero anisotropy (For bulk). The crystal structure of the model is a bcc lattice with lattice constant as 2.86 Å and the system is 10 nm × 10 nm × 1.4 nm with periodic boundary condition. For the simulation of the material defect in CoFeB/Ta interface, we consider Ta atoms play a role as non-magnetic atom in the system. The MgO induces a strong perpendicular anisotropy at the interface between CoFeB which has been studied by Ab-initio calculation [138, 139]. The exchange coupling of Fe and Co sites at the same interface also been enhanced. The adopted parameters of the interface and bulk CoFeB atoms are list in Table 4.2. The parameters for the simulation model in this work are obtained from direct comparison with experiments which is given as below [140]. The atomic spin moment μ_S = 1.60μ_B corresponding to M_S = 1.3 MAm^{-1}, which is close to experimental value [134]. The total torque in the system and the temperature-dependent properties of the system are calculated by the constrained Monte Carlo method [141, 142]. We considered that the Ku (uniaxial anisotropy energy) reflects the comprehensive magnetic properties of the sample including Ms, volume of samples, and external magnetic field. Ku as a key parameter was chosen for our simulation model.

Table 4.2 Adopted model parameters in the atomistic simulation

	CoFeB(interface with MgO)	CoFeB(bulk)	Unit
J_{ij}	1.547×10^{-20}	7.735×10^{-21}	J $link^{-1}$
μ_S	1.60	1.60	μ_B
k_u	1.35×10^{-22}	0.0	J atom^{-1}

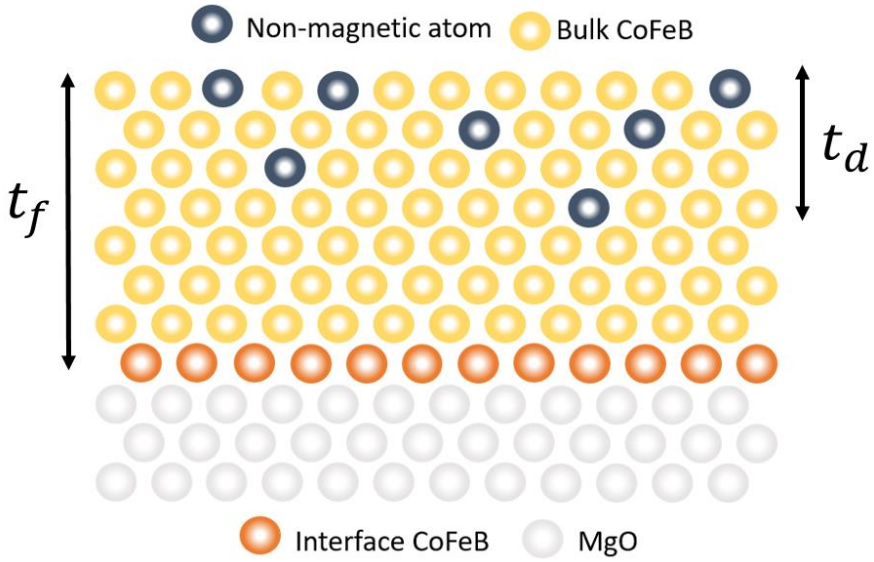

Figure 4.11 The atomistic spin model of the CoFeB single layer with material defects. The t_d, t_f are the thickness of the defect layer and the film thickness respectively.

The atomistic simulation model in this work has been considered as the magnetic anisotropy of CoFeB thin film is provided by the monolayer atom. The atomistic simulation model has been given in Figure 4.11, the defect layer t_d and film thickness t_f have been marked in the figure. In this model, we assume that the anisotropy energy of the CoFeB system is enhanced by the non-magnetic atoms in the defect layer. According to Figure 4.11, the non-magnetic atoms reduced the effective thickness to $t_d \cdot \varepsilon$. Then the net anisotropy without thermal effect can be explained as

$$K = \frac{0.5K_0 a}{t_f - t_d \cdot \varepsilon} \tag{4.5}$$

where ε is the defect concentration, a is the CoFeB lattice spacing, K_0 is the anisotropy of the CoFeB layer in contact with the MgO layer, and 0.5 is the coefficient calculated from the bcc crystal structure. From the results, when the number of defect atoms increases, the perpendicular anisotropy for the whole system will also increase. Furthermore, the trend of the anisotropy variation depends on the number of non-magnetic atoms. The PMA of CoFeB is provided by the hybridization between Fe-3d and O-2p orbitals at the MgO interface[63]. In the simulation, we assume one monolayer of atoms at MgO/CoFeB interface provide a local PMA, which is stable and unaffected by the defect sites. However, due to a reduction in the effective magnetic thickness, the effective anisotropy can be described approximately by the expression

$$K = K'\left(1 + \frac{t_d \cdot \varepsilon}{t_f}\right) \tag{4.6}$$

where $K' = \frac{K_0 a}{t_f}$, and t_d, t_f are the thickness of the defect layer and the film thickness respectively. This expression is plotted as solid lines in Figure 4.12 and gives good agreement with the simulations. Thus, the existence of defects will lead to a

nonuniform PMA distribution in the sample. A local area having high defect density will be hard to reverse, thus generating hard nucleation point named “hard centers”; conversely, a local area with low defect density should be easily reversed, thus generating easy nucleation points named “easy centers”.

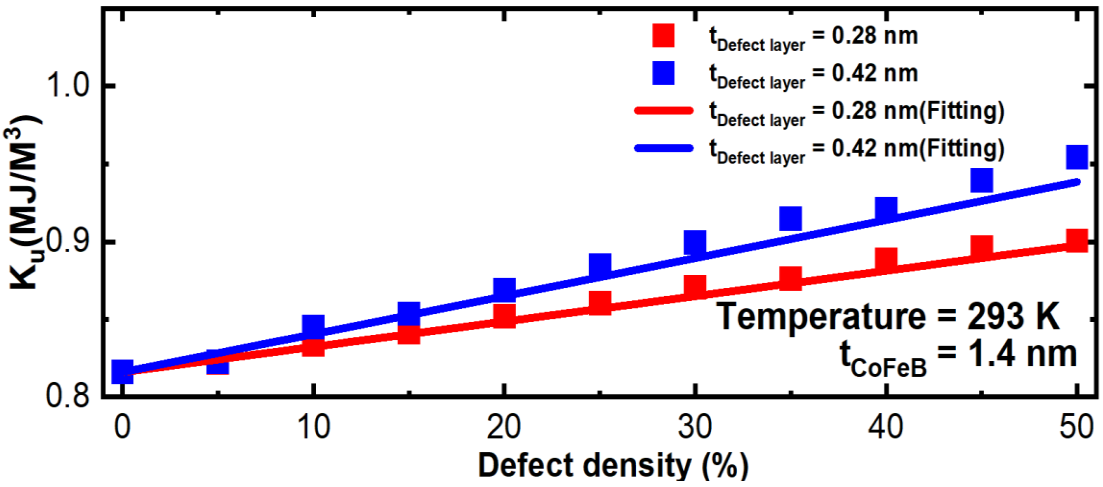

Figure 4.12 The atomistic spin model simulation of defect-influenced magnetic anisotropy energy in the CoFeB single layer. The defect density means the percentage of missing atoms in the defect layer.

4.4 Skyrmion density controlled via FORC technique

4.4.1 Stable region of Skyrmions investigated by FORC

To generate skyrmions by a magnetic field, a unidirectional field has frequently been applied to CoFeB ultrathin films[100, 111, 112, 143], but its value was just previously empirically adjusted by increasing the field strength gradually until magnetic skyrmions are generated[100, 111, 112, 143]. Until now, achieving controlled skyrmion generation using magnetic field, regulating the nucleation density and determining stable regions has been a challenge since skyrmion are metastable and only stable in a certain magnetic region. Because the applied field can trigger the phase transition between skyrmions and other metastable states, creating magnetic skyrmions inevitably requires to overcome energy barriers existing between different spin textures, indicating that magnetic skyrmions are stable only when they are trapped in magnetic potential wells with local minimum free energy. According to the simulation results, the defects induce a nonuniform anisotropy distribution in the system, which enhances the fluctuation of energy barriers, leading to the formation of many local magnetic potential wells. With the first-order reversal curves (FORC) technique[144], the return magnetization provides a unique way to achieve various meta-stable states determined by these local potential wells, which can then be utilized to control the density of the skyrmions. This study is the first report by applying FORCs to CoFeB via MOKE

microscopy, which the real-time domain structure evolution versus magnetization state could be clearly investigated. The generation of a FORC is generally preceded by the saturation of a system in a positive out-of-plane applied field initially. The magnetization M is then measured continuously from a reversal field H_r back to positive saturation, tracing out a FORC. Figure 4.13a shows a family of FORCs measured at different H_r with equal field spacing of 0.65 Oe. For each FORC with H_r near the coercivity, an unusual valley is formed, showing a delayed magnetization behavior suggesting that the domain reversal would continue even though the applied field H is decreasing. The delayed magnetization behavior contributes to the magnetic aftereffect, caused by the thermal activation, and evidenced by a time dependent magnetization measurement. When H_r is larger than the coercivity and close to the saturation field, the delayed magnetization behavior is weakened gradually, accompanied by a clear left-valley-shift (Figure 4.13a).

As analyzed in Figure 4.1b and c, only a few skyrmions are generated by applying a unidirectional H. In contrast, in the return magnetization of the FORCs (Figure 4.13a), H is not the only parameter controlling skyrmion generation, but the reversal field H_r also plays a critical role. Here, the slope χ^d for each FORC is defined as the derivative:

$$\chi^d_{H_r}(H_r, H) = \frac{dM(H_r,H)}{dH}|_{\mathrm{H}_r=constant} \quad (4.7)$$

With varying of H_r, χ^d is scanned in the H-Hr plane, mapping out a contour plot (Figure 4.13b) or a 3D plot (Figure 4.13d). Magnetic skyrmions are only observed in Zones 1, 2 and 3 (Figure 4.13b and d). Here, the skyrmion field stability is evaluated by the slope χ^d, and simultaneously the influence of the magnetic aftereffect is considered. For FORCs in Zone 1 (-4.2 Oe < Hr < -1.6 Oe), several magnetic skyrmions are initially nucleated at easy centers. The slope χ^d in Zone 1 is approximately equal to zero, indicating only a slight changing of M caused by H, thus magnetic skyrmions in this region are field stable. However, due to the influence of the magnetic aftereffect, skyrmions in the left of Zone 1 ($H < 0$ Oe, marked by a red dashed circle in Figure 4.13b) will finally transform to a multidomain phase after applying a fixed field ($H < 0$ Oe) and a long enough waiting time. Therefore, magnetic skyrmions are generated in the left region of Zone 1, but the real stable region is the right of Zone 1. For Zone 2, H_r is close to the saturation field and located at the rounded edge of the major hysteresis loop (Figure 4.13c, marked in the red line). The FORC start from an initial high negative H_r (-26.3 Oe < Hr < -21.8 Oe), and follow the return magnetization.

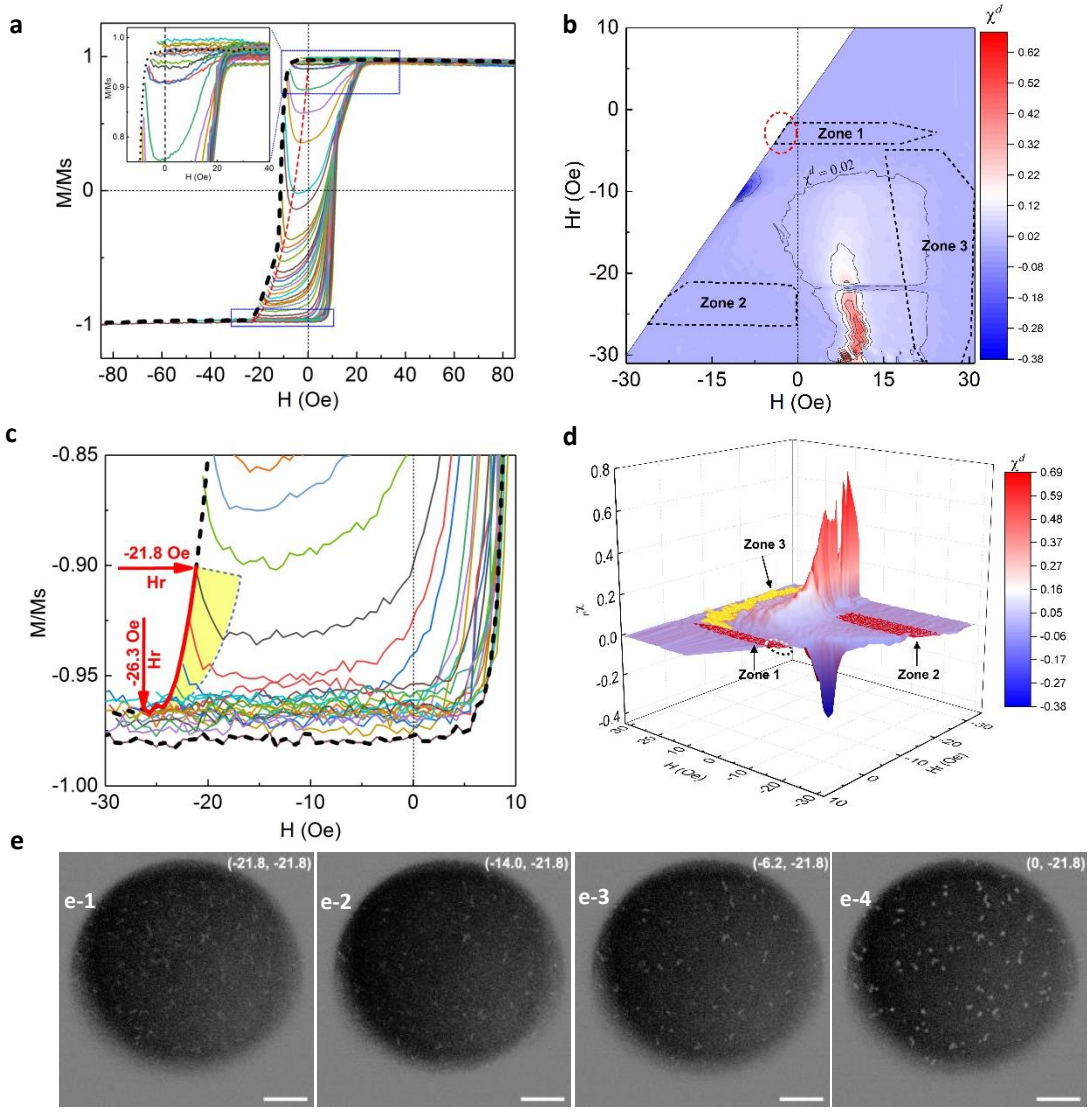

Figure 4.13 Return magnetization analysis for substrate/Ta(5)/MgO(3)/CoFeB(1.4)/Ta(5) film. a, A family of FORCs with an out-of-plane field, showing obvious left-shift valleys (dashed red line). The inset is the enlarged plot for FORCs marked in the right rectangle. b and d, A contour and a 3D plot of the FORC slope χ^d versus H_r and H. Zone 1, 2 and 3 is the skyrmion phase diagrams determined by (H, H_r). c, The enlarged plot for FORCs marked in the bottom rectangle of plane a. The red line indicates H_r required for the skyrmion generation. The yellow region highlights the influence of the magnetic aftereffect. e, MOKE images for the transition from stripe domain to skyrmion in the FORC with H_r = -21.8 Oe. The top-right labels are denoted as (H, H_r) with the unit of Oe. The scale bar is 20μm.

Take the FORC with H_r = -21.8 Oe as an example. Due to high H_r, most of the film area has been reversed except for some stripe domains (Figure 4.13e-1). With H increasing, the stripe domains continue switching due to the magnetic aftereffect, and then transform to magnetic skyrmions at hard centers (Figure 4.13e-2). Because the film cannot be thoroughly saturated in a return magnetization process and the

slope χ^d is a small value fluctuating slightly, the magnetic skyrmions exhibit high field stability, maintaining their bubble-like shapes in a wide field range. With H further increasing to -6.2 Oe and then to 0 Oe, the skyrmion size enlarges and part of the new skyrmions emerge due to a slight increase of χ^d (Figure 4.13e-3 and e-4), owing to the magnetization relaxation with H. In Zone 2, the fluctuation of the FORC slope χ^d is weakened with H_r decreasing and the FORCs approach to the horizontal gradually. In addition, the delayed magnetization is depressed in high field regions, thus the magnetic aftereffect influence is restricted to a narrow range ($\Delta H < 3$ Oe, the yellow region in Figure 4.13c), leading to the elevated field stability. Independent measurement is performed to verify the skyrmion stability. Skyrmions are initially generated at H_r = -23.7 Oe and H = -12.0 Oe, and then H is tuned randomly in the range from -2.0 Oe to -22.0 Oe; no deformation is observed in the process, showing high topologically protected stability. For Zone 3, the skyrmion generation is similar to that in the major hysteresis loop, where only a few skyrmions can be generated at hard centers. Because the slope χ^d in Zone 3 is much larger than that in Zone 1 and 2, the skyrmions are rapidly reversed and the sample is thoroughly saturated. As analyzed above, although magnetic skyrmions can be generated in Zone 1, 2 and 3; however, Zone 2 is the only region to generate magnetic skyrmions with both high density and high stability.

4.4.2 FORC investigation on CoFeB ultrathin films series

Besides substrate/Ta(5)/MgO(3)/CoFeB(1.4)/Ta(5), the return magnetization for other samples are also investigated utilizing the FORC technique. As shown in Figure 4.14a, each FORC for substrate/Ta(5)/MgO(3)/CoFeB (1.2)/Ta exhibits a gradual domain rotation in return magnetization processes, and no multidomains but uniform domains are observed in these process. For the sample of substrate/Ta(5)/CoFeB(1.2)/MgO(3)/Ta(5), no any magnetic skyrmions but fast wall-jumping reversal are observed in the return magnetization of substrate/Ta(5)/CoFeB(t)/MgO(3)/Ta(5). A family FORCs are measured at different Hr with equal field spacing of 0.33 Oe and shown in Figure 4.14b. The FORCs are approximately parallel to the major hysteresis loop when $H_r \geq -14.62$ Oe. With Hr is equal to -14.95, -15.28 and -15.61 Oe, the corresponding FORCs exhibit a sharp drop, showing a delayed magnetization reversal caused by the magnetic reversal. The thermal activation is so fast that no distinct valleys are formed in their FORCs. The corresponding MOKE image investigation shows fast domain-wall propagation in the return magnetization processes, and no magnetic skyrmions are observed there. In addition, the sample substrate/Ta(5)/MgO(3)/CoFeB(t = 1.3)/Ta(5) has a similar curved loop and similar skyrmion generation as the sample with t = 1.4 nm. The corresponding FORS investigation demonstrates similar results that high density magnetic skyrmions can be generated. Therefore, it is concluded that magnetic skyrmions in CoFeB ultrathin films are strongly correlated with the defects, and the skyrmion generation and density can be artificially controlled and tuned utilizing the return magnetization.

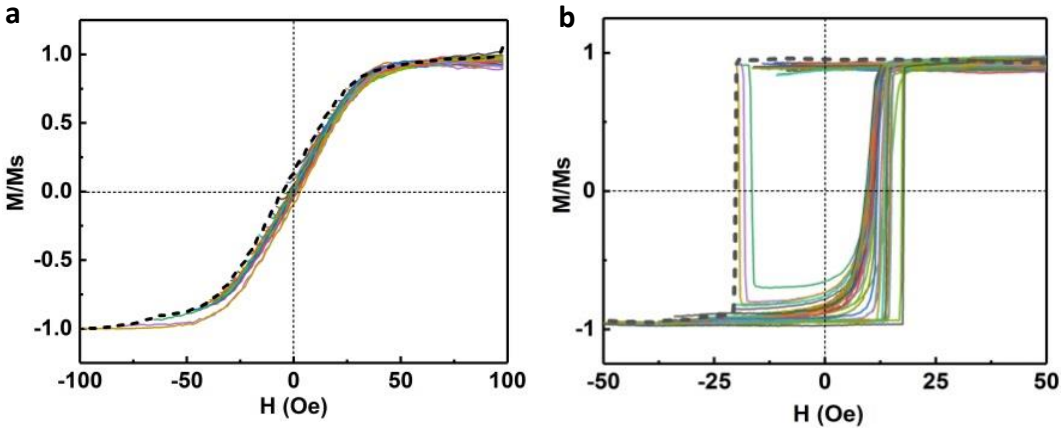

Figure 4.14 Return magnetization investigation with an out-of-plane field for CoFeB films. a, A family of FORCs for substrate/Ta(5)/MgO(3)/CoFeB (1.2)/Ta. b, A family of FORCs for substrate/Ta(5)/CoFeB(1.2)/MgO(3)/Ta(5).

4.4.3 Magnetic aftereffect

The magnetic aftereffect causes a delayed magnetization reversal and leads to a valley formation in the FORCs of substrate/Ta(5)/MgO(3)/CoFeB(1.4)/Ta(5). The magnetic aftereffect in samples is caused by the thermal activation which can be confirmed by a time-dependent magnetization measurement. The temperature effect on the switching behavior is quite strong when the external fields are just below the zero-temperature coercive threshold. When a low external field is applied, thermal fluctuations can provide enough energy to take the magnetization over energy barriers that prevents moments from aligning with the external field. As shown in Figure 4.15a, the magnetization reversal can be triggered even at a low fixed field -5.8 Oe after waiting a long time enough. When the external field increases to a high value, the thermal-activated magnetic reversal is accelerated rapidly, thus the delayed magnetization is depressed in high field region, resulting in a weakened left-shifted valley in FORCs.

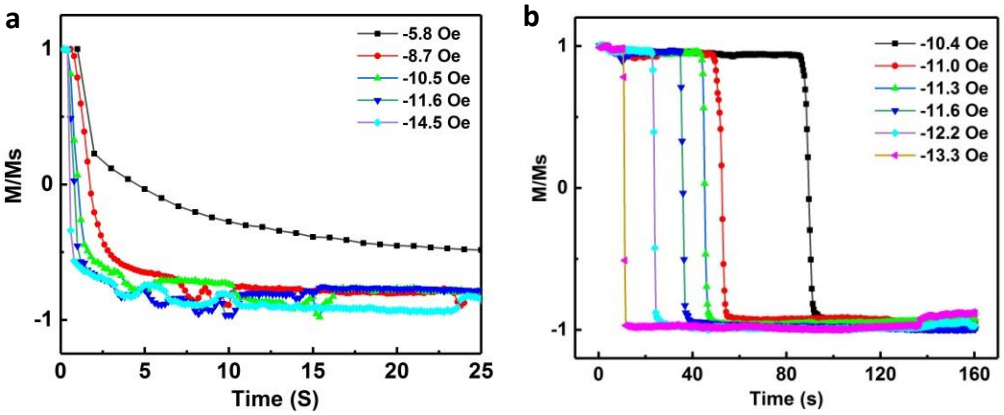

Figure 4.15 Magnetic aftereffect relaxation curves. a-b, Time dependences of M/M_s at several fixed magnetic fields corresponding to substrate/Ta(5)/MgO(3)/CoFeB (1.4)/Ta and substrate/Ta(5)/CoFeB(1.2)/MgO(3)/Ta(5), respectively.

For the sample substrate/Ta(5)/CoFeB(1.2)/MgO(3)/Ta(5), the time-dependent magnetization curves (Figure 4.15b) are quite different from those in Figure 4.15a, showing a sharp drop behavior. With the external field increasing gradually, the waiting time to trigger the switching is shortened rapidly. According to the Fatuzzo-Labrune model[145], the jump behavior (Figure 4.15b) reveals a wall-propagation-dominated reversal process, while the exponential slowing (Figure 4.15a) indicates a nucleation-dominated reversal process, which is in consistent with MOKE imaging investigation. Therefore, the substrate/Ta(5)/CoFeB(1.2)/MgO(3)/Ta(5) sample shows a homogeneous feature in comparison with the substrate/Ta(5)/MgO(3)/CoFeB(1.4)/Ta(5) sample.

4.4.4 Skyrmion density discussion

Figure 4.16a shows the skyrmion density for different FORCs in zero applied field. The density of skyrmion was calculated by the number divide by area. The skyrmion density is strongly affected by H_r, and the highest density is $2 \times 10^4\ mm^{-2}$ (Figure 4.16b-2) corresponding to the FORC with H_r = -22.4 Oe. Here, an energy potential scheme is proposed to interpret the influence of H_r and explain why few skyrmions are obtained in the major hysteresis loop (Figure 4.16c). In the major hysteresis loop, few magnetic skyrmions are generated at low H because the number of easy centers is too few (Figure 4.1b-1). As H decreases, these skyrmions rapidly transform into multidomain phases. Although new nuclei are constantly generated during wall propagation, they are soon submerged in the multidomain states (Scheme I of Figure 4.16c). As H decreases to near saturation field, most hard centers are switched except for some hard centers with very high energy barriers, so few skyrmions are also produced at high H (Scheme II of Figure 4.16c). In contrast, H is increasing in the return magnetization of FORCs (Zone 2 in Figure 4.13b), thus large quantities of hard centers are exposed with the Zeeman energy decreasing (Scheme II of Figure 4.16c). Consequently, the initially formed stripe domains ($H = H_r$) are easily trapped at the exposed hard centers and eventually converted into metastable magnetic skyrmions with opposite chirality. As H_r further decreases, closer to the saturation field, fewer hard centers are exposed, which implies that skyrmion density decreases with H_r (Figure 4.16b).

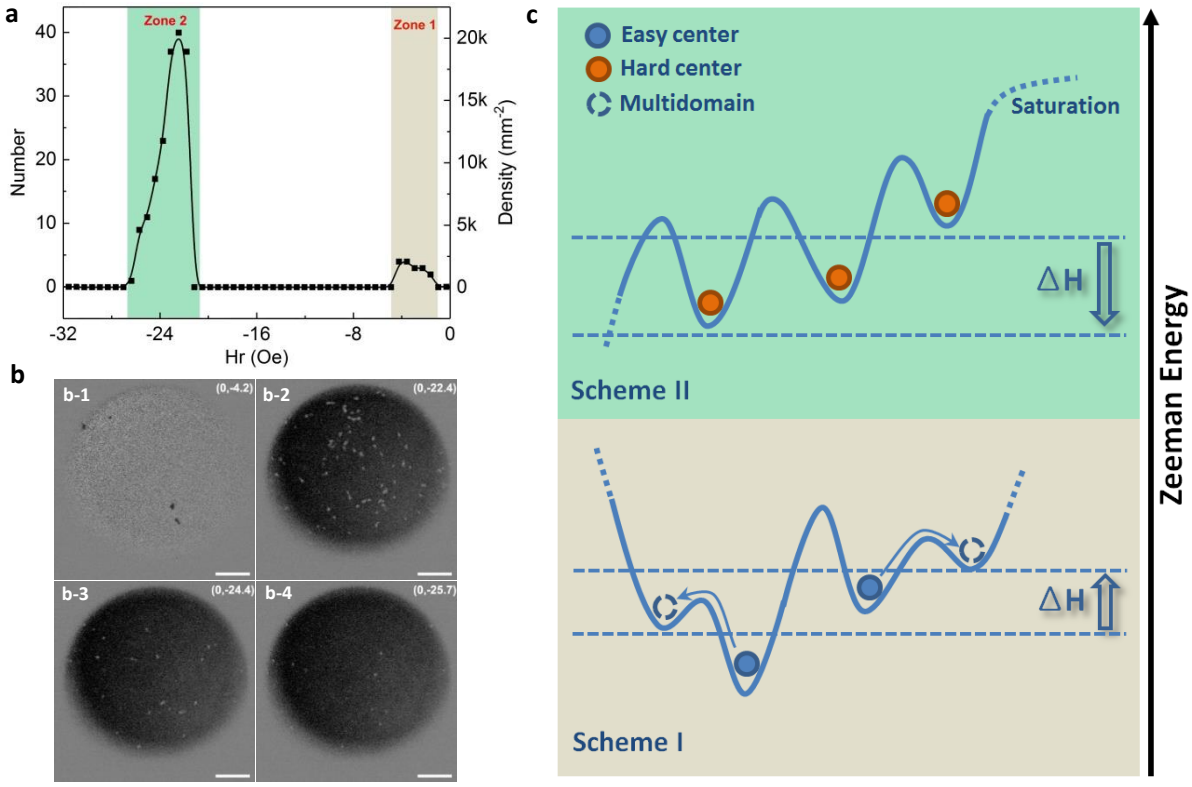

Figure 4.16 The density variation and the scheme for skyrmion generation. a-b, The density/amount and MOKE images of magnetic skyrmions generated at H = 0 Oe for different FORCs. The top-right labels in plane b are denoted as (H, H_r) with the unit of Oe. The scale bar is 20 μm . c, Magnetic energy potential scheme for skyrmion generation at different Zeeman energy.

4.5 Summary and discussion

In conclusion, we have elucidated the intrinsic relationship between fabrication, microstructures, magnetization and skyrmion generation in the MgO/CoFeB/Ta ultrathin films. The sputtering-induced defects cause generally a nonuniform PMA distribution, which leads to the formation of local magnetic potential wells at defect sites during the magnetization. With the FORC technique, the return magnetization can trap and stabilize skyrmions in these potential wells, and thus the skyrmion density and the stable region can be efficiently controlled. These results establish a universal guidance from sample preparation to skyrmion generation, offering a general method to control skyrmion density via the return magnetization, which should also apply to other PMA FM/HM systems for the skyrmion based spintronics applications.

As mentioned in the literature part about defect-skyrmion, the relevant large size of artificial defect induced skyrmion generation has been investigated. In our research,

however, the entity inhomogeneous sample disorder has been studied. This distribution of disorder exist in whole sample caused by sputtering can change the magnetic properties which leading the skyrmion favor generation in more disorder sample. The defect detection based on ultrasonic[146], eddy current[147] and thermography[148] have been investigated for few decades and widely used in Non-Destructive Testing and Evaluation (NDT&D)[149]. For the further study of defect-skyrmion, combining these detection methods with our experiments would quantify defects in our samples. The relationship between the defects and skyrmion generation will become clearer.

Chapter 5-Study on temperature dependent magnetic properties and perpendicular magnetic anisotropic gradients observed via temperature gradients induced

5.1 Introduction

The temperature as a key and special parameter cannot be neglected and the use of temperature can open a new branch in spintronic applications. The temperature dependent CoFeB based magnetic tunnel junction (MTJ) has been investigated for decade[74, 75]. The MTJs are required to operate at a certain temperature range depending on specific application. Therefore, it is of importance to elucidate how the properties of MTJ vary with temperature. The temperature gradient induced spintronic devices is the future development significant direction. Skyrmion, as one of a domain phase, will also be impacted by the thermal effect. Using of the thermal effect to create and drive skyrmion is a hot topic in most recently[88].

In this chapter, we directly compare the influence of the vary temperature and temperature gradients on the magnetization reversal of perpendicular magnetic anisotropy CoFeB based thin film. We aim to give a guidance for the proportion working temperature of CoFeB based device and provide a possible explanation for the temperature gradient driven magnetic domain or skyrmions. It would be a useful method for high density skyrmion generation and driven by using the PMA CoFeB mentioned in the previous chapter. This study also offers a contribution on simple method for perpendicular magnetic anisotropy induced via temperature gradient.

5.2 Sample preparation

Substrate/Ta(5)/MgO(3)/CoFeB(t)/Ta(5) (from the bottom, layer thickness in nm) samples were deposited on thermally oxidized Si wafers (100) using magnetron sputtering system at RT with base pressure better than 5×10^{-5} Torr. To obtain flat surface morphology, the working pressure during sputtering was kept low at about 3.3×10^{-1} Torr in Ar atmosphere. In the fabrication, metallic layers (Ta) were deposited by dc magnetron sputtering, while MgO and CoFeB layers were deposited by RF magnetron sputtering. A Ta capping layer of 5nm thickness was deposited to protect the films against oxidation. Because the PMA originates from the Fe-O

hybridization and B accumulation at interface, which only exists with a very small layer thickness range, thus the thickness of the CoFeB (0.8-3 nm) layer was varied across the films studied in this work. Finally, the deposited films were annealed in a high vacuum furnace chamber at 300 ºC for 30 min. The sample introduced here is the same as the sample in the chapter 4.

5.3 Experiments and results

5.3.1 Variable temperature Vibrating Sample Magnetometer (VSM) measurements

The magnetization curves were measured in a stack structure of Substrate/Ta(5)/MgO(3)/CoFeB(1.4)/Ta(5) along the hard-axis and easy-axis direction by a vibrating sample magnetometer (VSM). The temperature starts from 150K and the hysteresis loop is measured by the step of 50K until 500K.

A series of typical out of plane magnetization curves are shown in figure 4.1. From the curves, we found that the whole magnetic properties of sample are various via different temperature. The coercivity is enhanced at low temperatures compared to room temperature or higher. Another significant change is the saturated magnetic moment (M). The CoFeB thin film shows a variation of M with increasing temperature. The change of M is more obvious at higher temperatures.

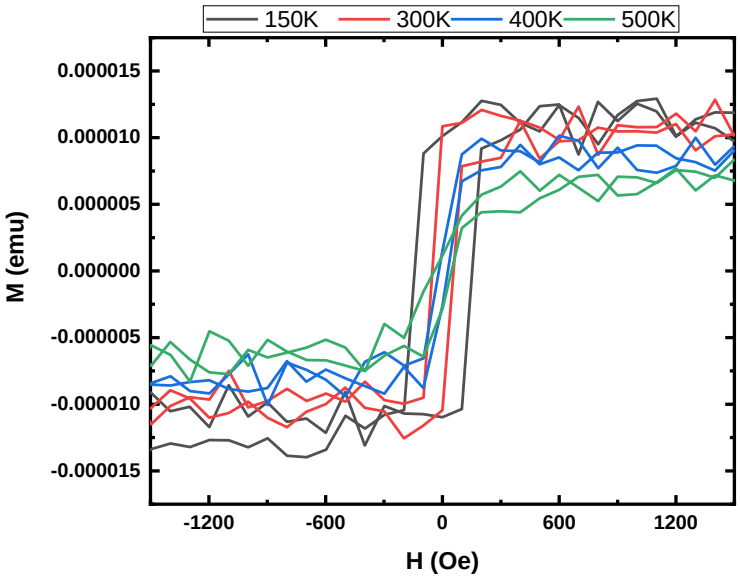

Figure 5.1 The out of plane magnetization curves taken from vibrating sample magnetometer (VSM) at different temperature.

Figure 5.2 shows the in-plane and out of plane hysteresis loops of a CoFeB thin film measured by the VMS at 500K. The magnetization curve indicates that the perpendicular anisotropy is much weaken at high temperature.

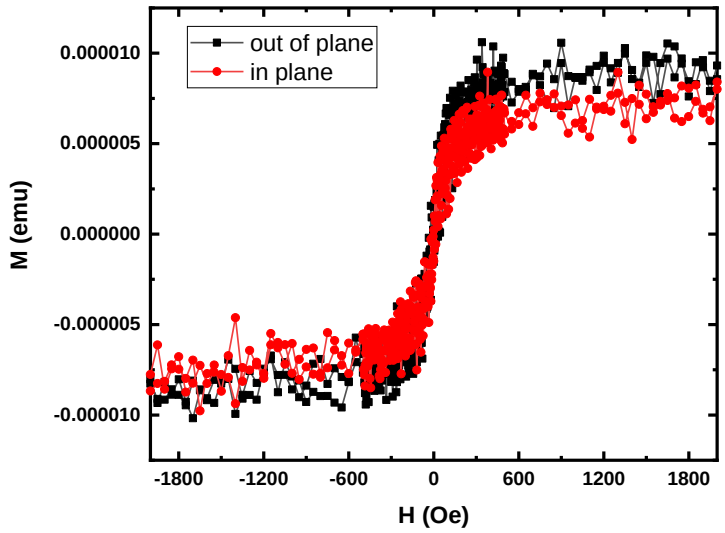

Figure 5.2 Hysteresis loop of CoFeB measured by the VMS at 500K.

Figure 5.3 shows the temperature dependence of saturation magnetization M_s, which is determined from the spontaneous magnetic moment per unit area M divided by the effective CoFeB thickness t of 1.4nm, between 150 and 500K. Although over most of the temperature range M_s is weakly temperature dependent, the slightly changes still could be captured. The M_s exhibits a monotonic reduction tendency in CoFeB thin film within experimental errors. The decay of the M_s at high temperature is greater than that at low temperature which indicates the CoFeB are affected greater at high temperature.

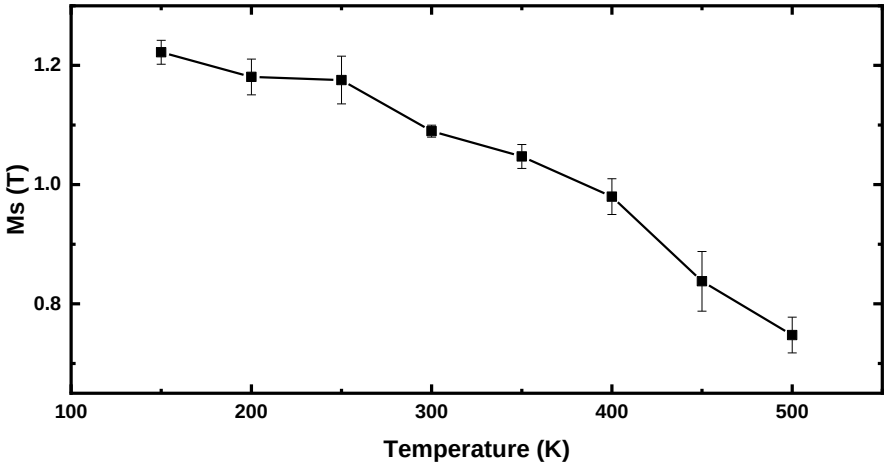

Figure 5.3 Temperature T dependence of spontaneous magnetization Ms for CoFeB stack between 150 and 500K.

The effective perpendicular anisotropy energy density K_{eff} is corresponding to the Ms and effective perpendicular anisotropy field H_k, which the saturated field for in-plane. As the Ms and H_k both exhibit a monotonic reduction tendency with temperature, the K_{eff} is also show the temperature dependence reduction. Because the interfacial anisotropy plays a domain role for perpendicular anisotropy in MgO/CoFeB system, the interfacial anisotropy energy density K_i also decreases with increasing T.

The results indicate that spintronics based on MgO/CoFeB probably exist a certain working temperature. The higher or lower temperature will change the magnetic anisotropy and properties which leading the devices disabled.

5.3.2 Variable temperature magneto-optical Kerr imagining (MOKE) measurements

The temperature variable magneto-optical Kerr (MOKE) experiment is achieved by using the cryostat (MicrostatHe-R from Oxford instrument). The MicrostatHe-R can provide wide temperature range from 2.2K to 500K. This cryostat can be used with liquid nitrogen which achieved rapid cooldown time for 4.2K in less than 10 minutes. The schematic diagram and instrument's details are shown in the figure 5.4.

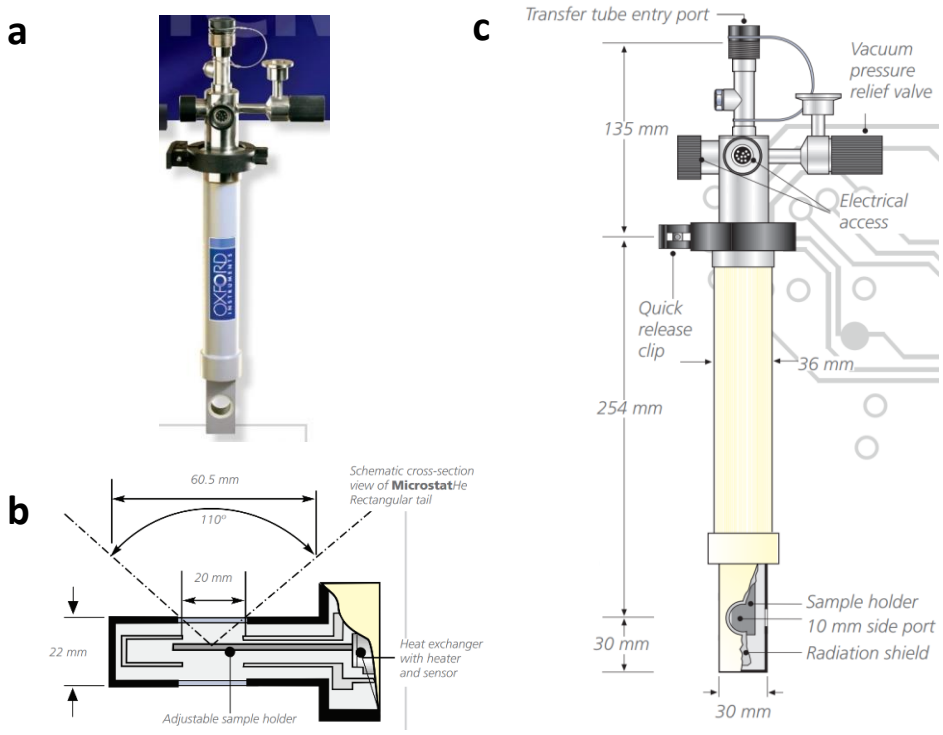

Figure 5.4 a, picture of MircostatHe-R. b, schematic cross-section details information of MicrostatHe rectangular tail. c, schematic diagram view and details information of MicrostatHe-R.[150]

The MOKE setup is not changed expect replacing normal sample stage to the

cryostat. A stack structure of Substrate/Ta(5)/MgO(3)/CoFeB(1.4)/Ta(5) with perpendicular magnetic anisotropy was measured the magnetization curve along the perpendicular direction at various temperature. The hysteresis loop was taken by the MOKE when the set temperature was reached and stabilized. The temperature range for MOKE experiment is from 200 to 340K.

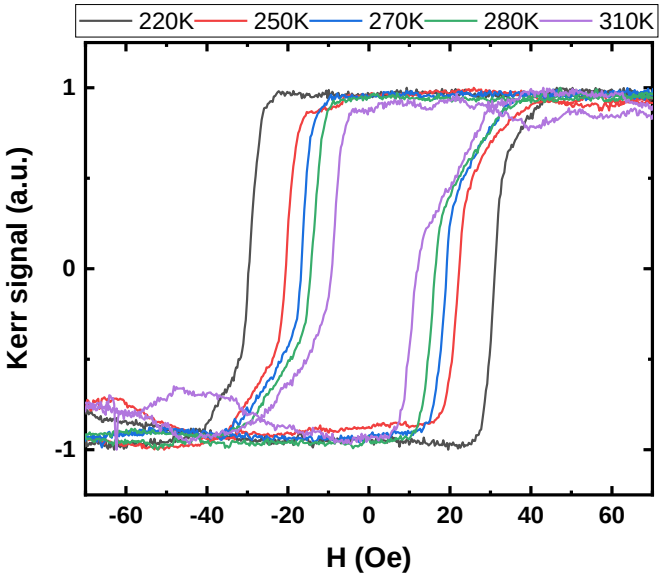

Figure 5.5 Temperature dependent out-of-plane Kerr hysteresis loops with magnetization (M) normalized to the saturation magnetization (Ms) for CoFeB thin film.

Figure 5.5 shows the typical magnetization curves of temperature dependent CoFeB thin film. The out-of-plane Kerr hysteresis loop with magnetization (M) normalized to the saturation magnetization (Ms). The coercivity exhibits temperature dependence, which increases with decreasing temperature. The black semi-square loop of CoFeB at 220K indicates the sample needs lager external field to reverse the magnetization. However, a smaller applied magnetic field can reverse the magnetization of CoFeB at 310K, shown as the violet curved loop.

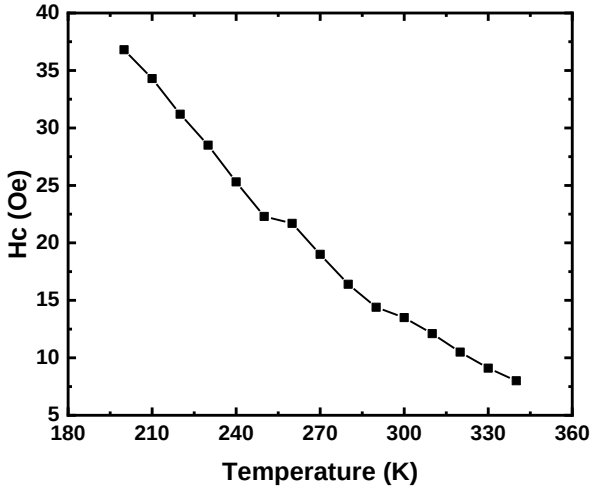

Figure 5.6 Coercivity versus temperature of CoFeB thin film.

Figure 5.6 shows the coercivity monotonic decay with temperature. The result

indicates that the heating can assist magnetization reversal, and cooling can maintain the magnetization of CoFeB against external magnetic field.

The domain structure has been captured by the MOKE imagining system in Ta(5)/MgO(3)/CoFeB(1.4)/Ta(5) (in nm) film under an out-of-plane field via various temperature as shown in the figure 5.7a to o. Those MOKE images were picked up at zero Kerr signal point (position of coercivity). The figure 5.7 shows that the domain width has changed dramatically under a wide range of temperature changes. The domain width evolved from thinner to thick with temperature reduction.

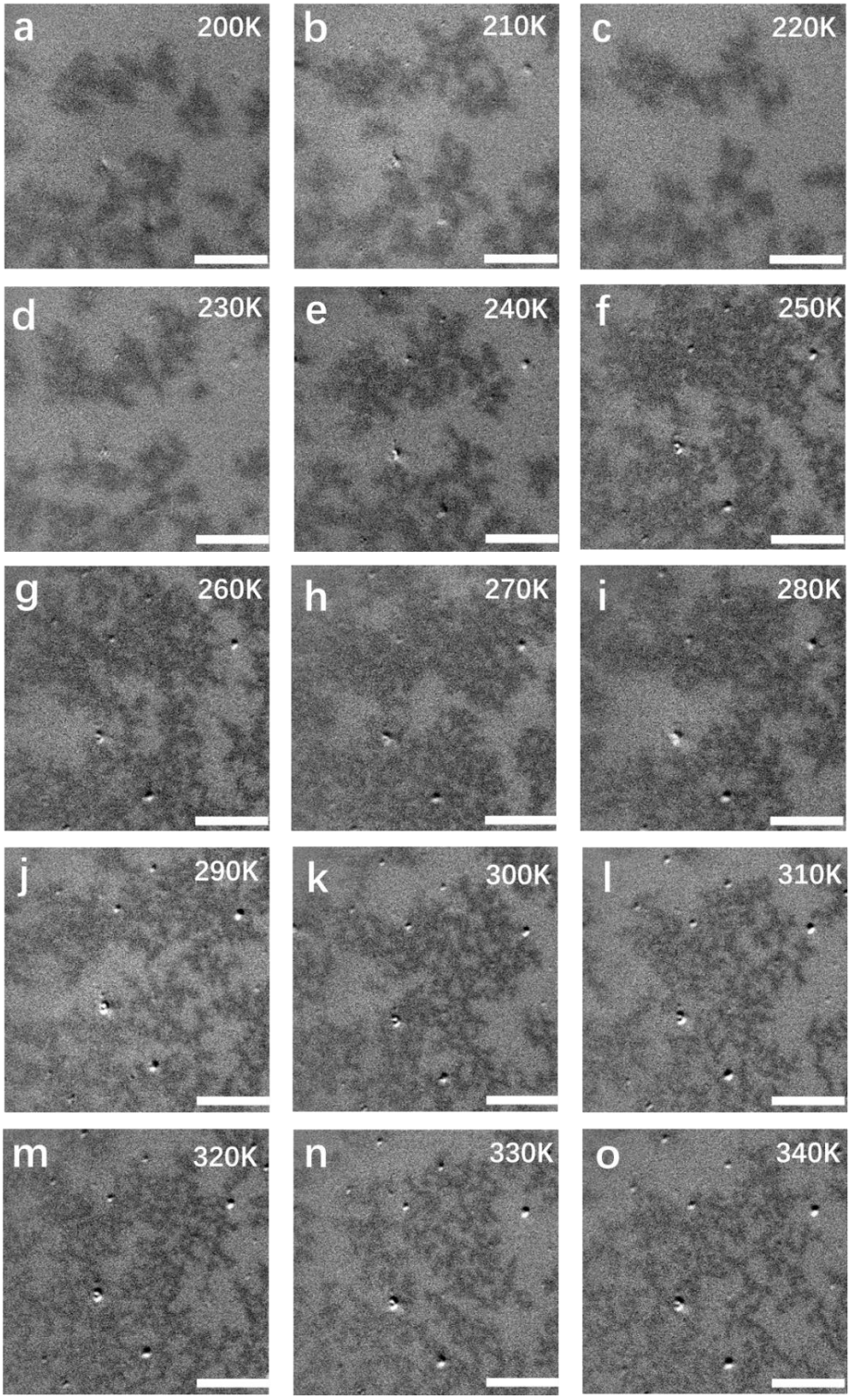

Figure 5.7 Polar-MOKE images for Ta(5)/MgO(3)/CoFeB(1.4)/Ta(5) (in nm) thin film illustrate the domain width evolved via temperature vary from 200 to 340K. The scale bar is 10μm.

The domain width shows monotonic decrease with increasing temperature as shown in the figure 5.8. The largest domain width at 200K is around twice as wide as the smallest domain width at 340K.

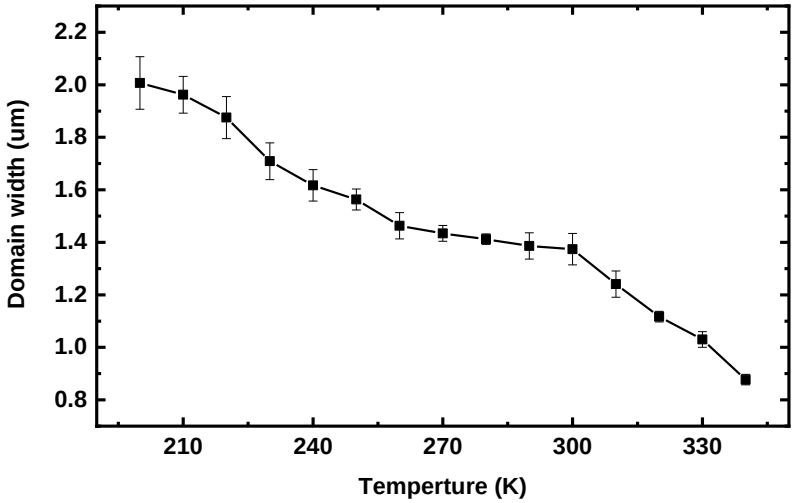

Figure 5.8 Domain width evolved versus temperature various.

A similar phenomenon has been proposed and explained in previously published works[151-153]. Their computational and experimental results suggest that the heights of energy barriers are proportional to the domain size and do therefore strongly depend on temperature. The domain size translation via decreasing temperature is not only because there is less thermal energy available, but mostly because the associated energy barriers increase strongly[153]. The previously reported theoretical and experimental results are in agreement with the observation in our sample system.

5.3.3 Temperature gradient induced magnetic anisotropy gradient observed via MOKE microscopy

Previous research has demonstrated that the domain phase can gradient evolved in magnetic thin films by inducing the magnetic anisotropy gradient, by adding or/and changing the thickness of varied-gradient interlayer or magnetic layer[50, 60]. Photolithography to create a wedge shape nanostructure is another way to induce magnetic anisotropy gradient[89]. The stress induced to the sample would also change the distribution of magnetic anisotropy[50, 154]. The characteristics of domain and domain motion would be affected by magnetic anisotropy exist. The induced of magnetic anisotropy can be seen as a part of spin injection to revers magnetization replacing external magnetic field.

The thermal fluctuations in domain patterns with perpendicular magnetization have been investigated[153]. The changing temperature can affect the transition between the domain phases. Based on previous experiments and other research, the temperature can deterministically change the magnetic anisotropy. Therefore, and magnetic anisotropy gradient can achieve by inducing temperature gradient. Due to the domain patterns exhibit different phases under various temperature, the magnetic anisotropy gradient can be reflected by observing the magnetic domain structure. Here, we demonstrate a

method of magnetic anisotropy gradient created by temperature gradient induced and observing by MOKE microscopy.

First, we introduce the temperature gradient inducing sample stage by using semiconductor chilling plate. We designed a sample stage based on the characteristics of temperature difference produced by semiconductor chilling plate as showing in figure 5.9. We use the cold side to cool the lower part of the sample, and heat the top half by using aluminum to transfer the heat generated from semiconductor chilling plate. Under different working voltage, the chilling plate can provide different temperature and temperature difference to yield temperature gradient. We use thermal conductive tape to stick on the sample to measure the temperature accurately, which avoids the temperature measurement error caused by metal reflection

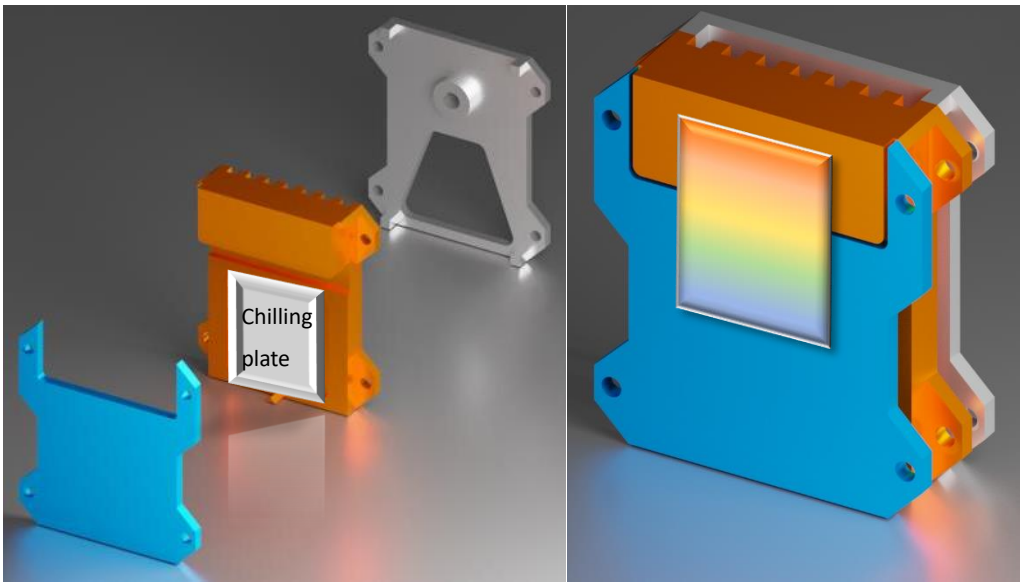

Figure 5.9 a, The schematic designed parts for temperature gradient generator sample stage. The semiconductor chilling plate adhesive in the middle part. b, the schematic assembled diagram of stage with sample. The colorful distribution on the sample corresponding to the temperature gradient. The blue and orange refer to the cold and hot side generated by chilling plate respectively.

A stack structure of Substrate/Ta(5)/MgO(3)/CoFeB(1.4)/Ta(5) with perpendicular magnetic anisotropy was measured by MOKE imagining system via temperature gradient generator sample stage. The temperature distribution is capture by an infrared camera. The measurements started when the temperature distribution generated by the chilling plate is stationary. The working voltage of chilling plate was selected at 1V as shown in figure 5.10a, which yielding a range of 27°C to 37°C temperature distribution. The temperature difference can be achieved in a very short during of 30 seconds, which benefits from the high efficiency of the cooling plate. The sample was highlighted by the gray dash rectangular as shown in the figure 5.10.

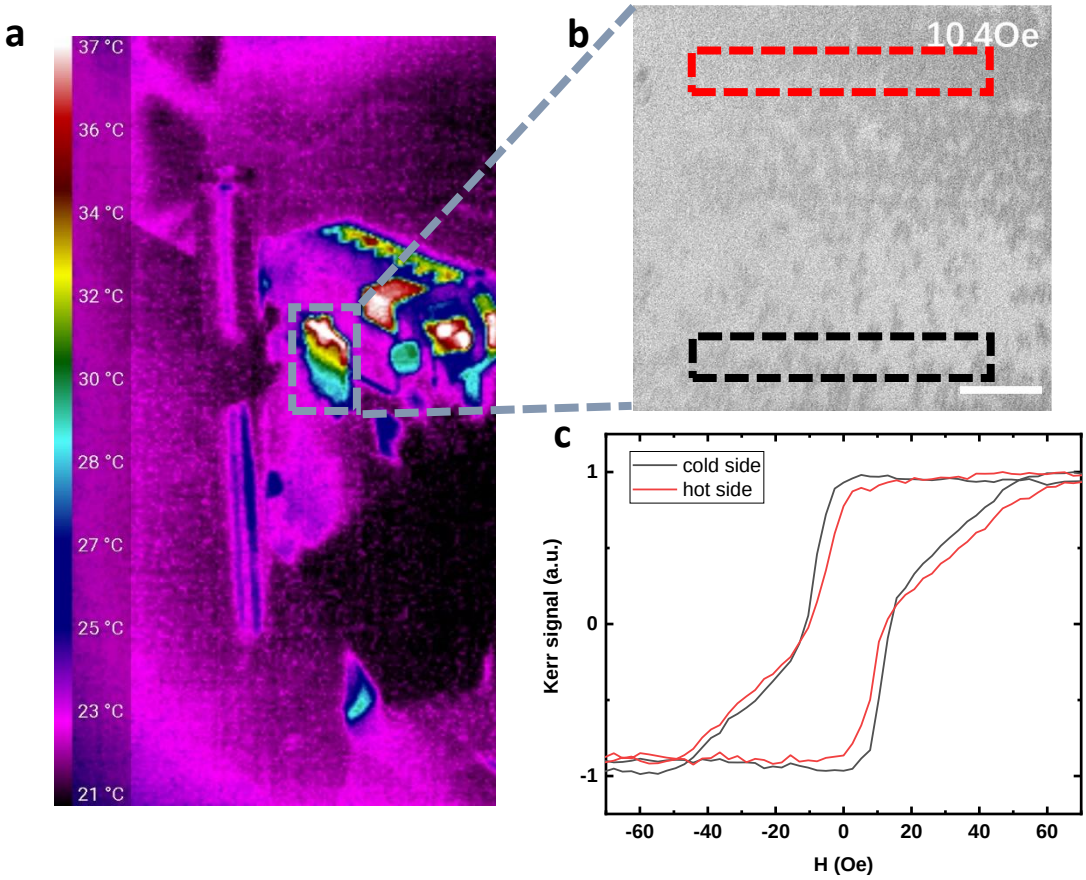

Figure 5.10 a, Temperature distribution captured by an infrared camera. The color mapping corresponding to the magnitude of temperature. The gray dash rectangular sketches the sample position. b, Polar-MOKE image taken from hysteresis loop at 10.4Oe. The red and black dash rectangular exhibit the hot side and cold side corresponding to the magnetization differences selecting area, respectively. The scale bar is 100μm. c, the hysteresis loop taken from hot and cold side respectively illustrated in b.

For easy observation, the HALO lens, replacing the objective lens, was used to enhance the field of view to investigate the magnetization affected by temperature gradient. Figure 5.10b shows the MOKE image taken from measurement at 9.1Oe, and the magnetization of temperature gradient induced CoFeB thin film at selected hot and cold area are presented in figure 5.10c. The magnetization of sample on the hot side reversed first and subsequently the magnetization of sample on the cold side reversed. In order to distinguish the effect of temperature gradient on the CoFeB thin film, figure 5.11 shows a comparative MOKE images taken at room temperature.

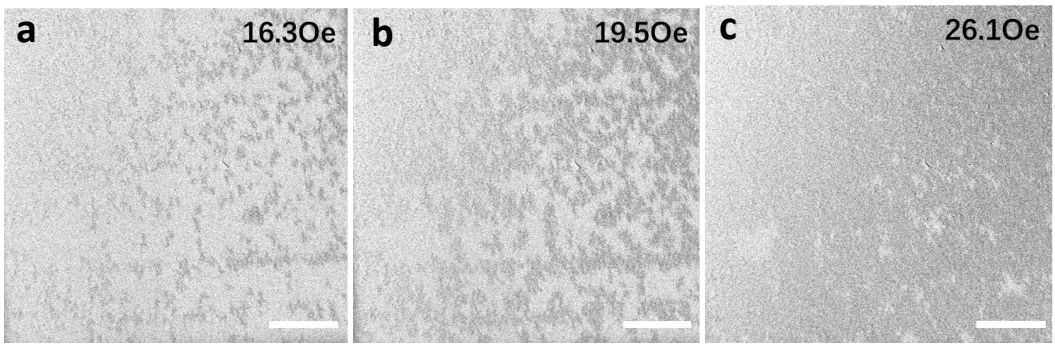

Figure 5.11 Polar-MOKE images exhibit the domain pattern evolved under external magnetic field at room temperature. The scale bar is 100μm.

The domain structures are first nucleating randomly in the sample as shown in figure 5.11a. Then the domain patterns extend and finally the magnetization almost reverses to saturation which is illustrated in figure 5.11b and c respectively. Comparing with domain structures generated at room temperature, due to the temperature gradient induced to the CoFeB thin film, the domains at hot and cold side are generated in different magnetic fields. This temperature gradient experiment was repeated for 10 times and the domain magnetization revers randomly occurred only once. According to the previous variable temperature VSM and MOKE experiments, the existence of temperature gradient affects the magnetization reverse process in sample which can be observed and used.

To further understand the domain patterns generation and propagation, the 50x objective lens was used to investigate the domain structure details. We first take the MOKE images of domain evolution at room temperature as the reference which is illustrated in figure 5.12a to c. The nucleation is taking place at first stage and subsequently domain expansion from nucleation, magnetization reversal at last.

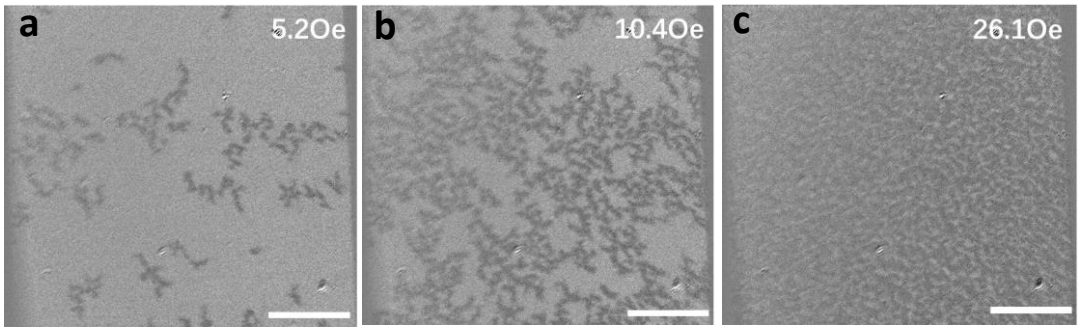

Figure 5.12 Polar-MOKE images illustrate the domain structure evolved under external magnetic field at room temperature. The scale bar is 20μm.

According to the results of domain width via variable temperature MOKE experiments as shown in figure 5.8, in the temperature range of 300 to 310K (corresponding to around 30℃ to 40℃), there is a drop in the domain width. Therefore, the working voltage of the chilling plate was selected at 1.5V as shown in figure 5.13a,

which yielding a lager range of temperature distribution for 30℃ to 43℃. The domain was first generated at the hot side and then expanded while few nucleation points or domain structure existed at the cold side as shown in figure 5.13b and c. Eventually, the domain structure extended to the whole view and will reverse till saturation. This temperature gradient experiment was repeated for 10 times and the domain magnetization revers randomly occurred three times. The reason why the domain magnetization revers randomly occurred higher than the previous experiment is possible that the high magnification objective lens zoomed in the view of the field. It is hard for generating enough temperature gradient sometimes in a limited observation region.

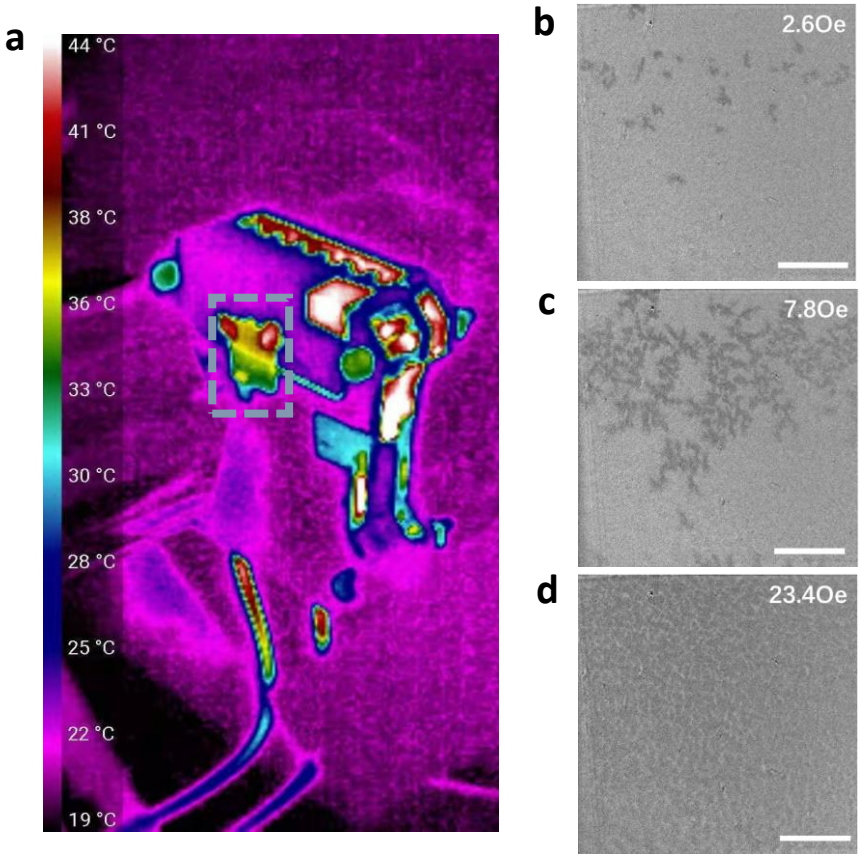

Figure 5.13 a, Temperature distribution captured by an infrared camera. The color mapping corresponding to the magnitude of temperature. The gray dash rectangular sketches the sample position. b to c, Polar-MOKE images exhibit the magnetization reversal process for CoFeB thin film under temperature gradient. The scale bar is 20μm.

To analysis the domain width change, we divide the MOKE image under magnetic field at 23.4Oe into three areas, red area, yellow area and blue area corresponding to the hot, middle and cold side as shown in the figure 5.14a. Then we pick up ten different positions to measure the domain width from three different areas and plot the average domain width showing in the figure 5.14b. The results clearly indicate that the domain width is affected by the temperature gradient which consistent with the previous experimental results. The relationship between the domain width and energy barriers

has been well explained in previous work[153]. The distribution of domain size implies the distribution of energy barriers.

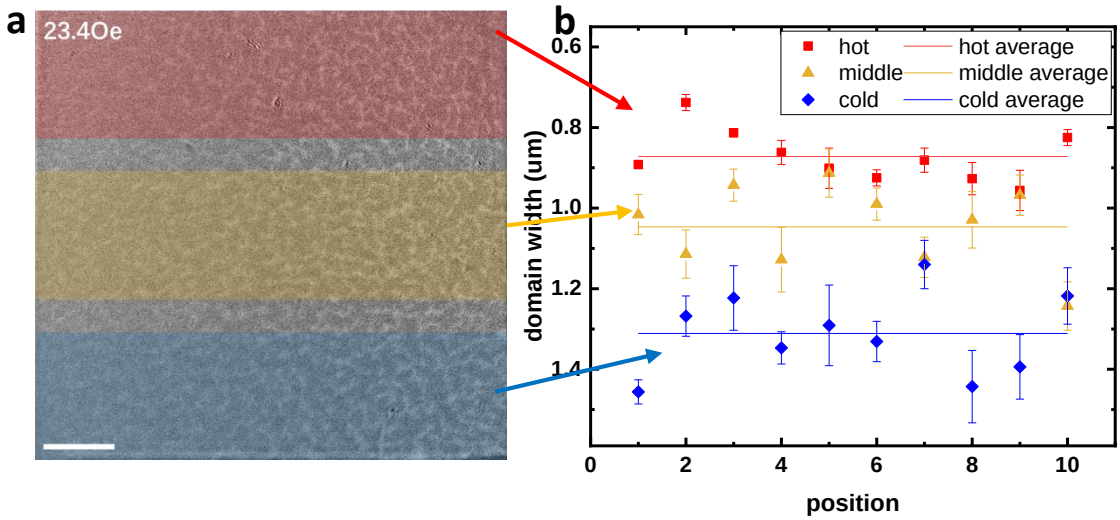

Figure 5.14 a, Polar-MOKE image exhibit the magnetization reversal process for CoFeB thin film under temperature gradient. The three colorful areas, red area, yellow area and bule area corresponding to the hot, middle and cold side. The scale bar is 10μm.

In additional, we carried out another PMA CoFeB sample with the thickness of 1.3 nm. The same temperature gradient experiment was applied to this CoFeB sample for providing an evidence for the repeatability of CoFeB system. The result is showing in the figure 5.15. The magnetization differential of cold and hot side can be clearly observed from the MOKE images as same as the phenomenon with the CoFeB(1.4nm) sample.

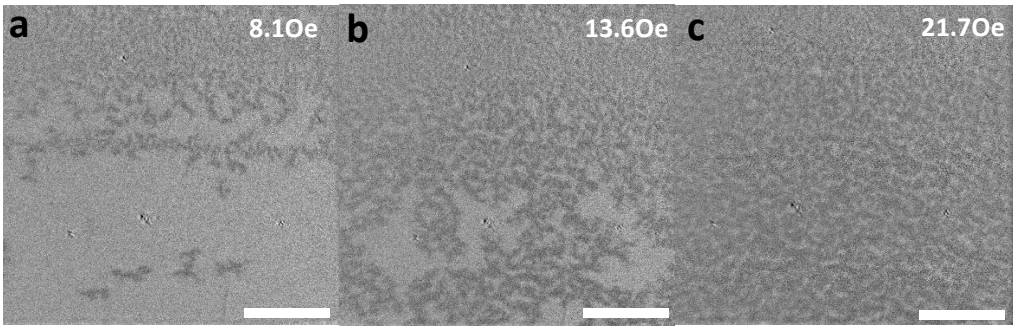

Figure 5.15 Polar-MOKE images exhibit the magnetization reversal process for CoFeB with the thickness of 1.3 nm thin film under temperature gradient. The scale bar is 20μm.

The distribution of magnetization and domain width under the temperature gradient proves the existence of magnetic anisotropy gradient. According to the variable temperature VSM experiments, the effect of temperature rise on magnetic anisotropy is greater than that of temperature decrease. Thus, the specific temperature gradient is

very important for inducing of magnetic anisotropy gradient.

5.4 Summary and discussion

In this chapter, we investigate the magnetic properties affected by the temperature via variable VSM and MOKE. The results indicate that as the Ms and H_k both exhibit a monotonic reduction tendency with temperature, the K_{eff} is also show the temperature dependence reduction. The effect of hotter on magnetic anisotropy is greater than that of cooler condition. The changes of magnetic properties and anisotropy gradient induced of the CoFeB thin film caused by temperature gradient are proposed in this chapter.

In general, we introduce a method to induce magnetic anisotropy gradient via temperature gradient. This innovative method will invigorate spintronics research. To further understand the changes of magnetic properties in sample induced by temperature gradient, we need to improve our sample stage to increase the temperature difference between the hot and cold sides. Furthermore, the Seebeck effect caused by the temperature gradient is one of important spin injection methods which has been investigated for decades[86, 155-157].

In the future research, the perpendicular magnetic anisotropy gradient induced by the temperature gradient would be an important research direction. The thermal gradient creation and manipulation of skyrmion has been proposed and achieved most recently[88]. The temperature gradient or thermal pulses can realize skyrmion or domain driven as same as the function of current pulse which provide another method to achieve skyrmion motion. The skyrmion generation in the inhomogeneous CoFeB has been studied in the previous chapter. We can use the characteristics of this sample, which large energy barrier distribution, combined with the temperature gradient, to achieve low power consumption of thermally driven spintronic devices.

Chapter 6-Paradigm of magnetic domain wall based In-memory computing

6.1 Introduction

While the conventional microelectronic integrated circuits based on the electron charge are approaching to the theoretical limitation in foreseeable future, next generation nonvolatile logic units based on electron spin have potential to build logic networks of low-power consumption. Central to this spin based architecture is to develop a paradigm for in-memory computing with magnetic logic units. Based on the previously chapter, the sample fabrication guidance and magnetic properties corresponding to memory performance of the soft magnetic material has been investigated. In this chapter, we are going to from studying effects of memory performance to designing practicable device based on soft magnetic material which realize a new memory functions. Therefore, we demonstrate the basic function of a transistor logic unit with patterned Y-shaped NiFe nanowires by gate-controlling domain wall pinning and depinning. This spin based architecture possesses the critical functionalities of transistors and can achieve a programmable logic gate by using only one Y-shaped nanostructure, which represents a universal design currently lacking for in-memory computing[158].

All the nanofabrication mentioned in this chapter were done by Dr. Li Chen in Leeds University. All the simulation results mentioned in this chapter were done by Dr. Junlin Wang in University of York.

6.2 The design and working principle of Y-shaped In-memory computing

Central to this work is presenting a phenomenon in specific design of DWL based on Y-shaped magnetic nanostructure which shows the similar function of a transistor in the circuit. The transistor inside the CMOS ALU (arithmetic logic unit) has a ‘Gate’ terminal which determines the conductivity of this device (as shown in Figure 6.1a and b). The Memory and CPU units in conventional CMOS-Based logic as shown in the figure 6.1(a) are designed to be separated. The arithmetic process within the logic must experience read and write procedures which costs time. For the Spin-Based logic (showing in the figure 6.1c), however, the MRAM can arithmetic itself so that breaks the memory wall and save the time.

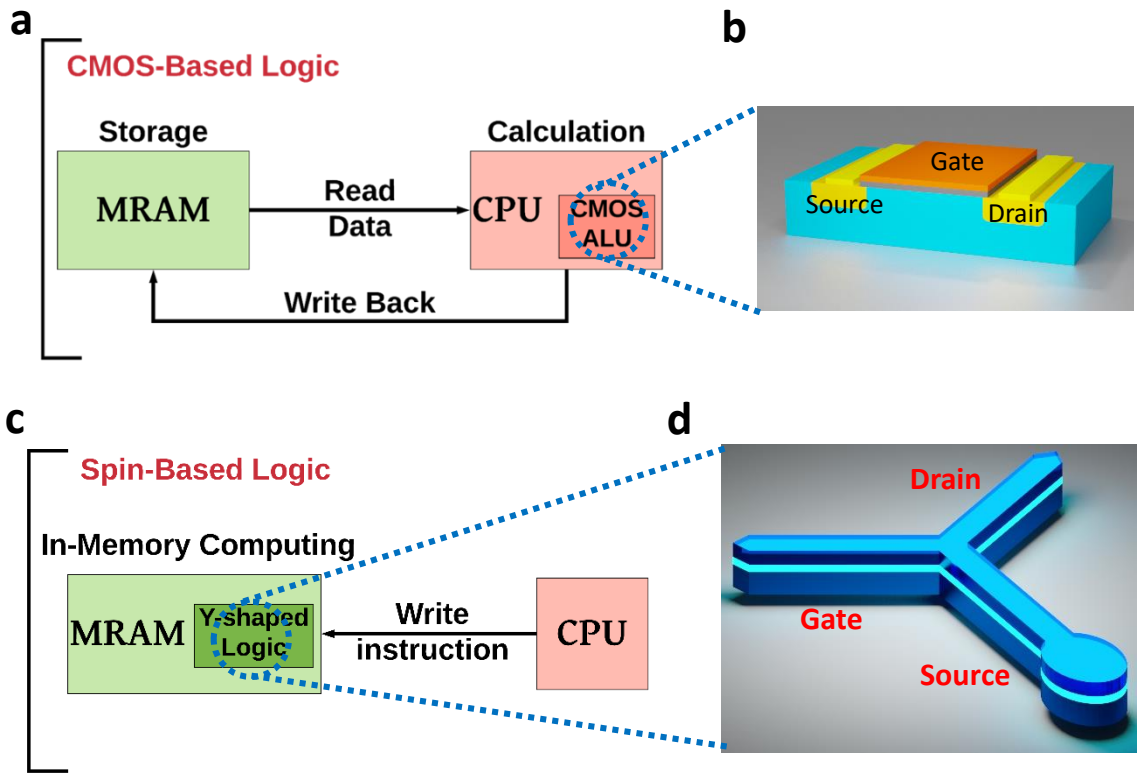

Figure 6.1 (a) Schematic diagram of conventional CMOS-Based architecture. (b) The conventional transistor used in integrated circuits. (c) The new design of spin-Based In-memory computing implemented Y-shaped logic can be stored and calculated with only one write instruction. (d) Schematic diagram of transistor-like permalloy Y-shaped nanowire with one nucleation pad. Three arms correspond to the 'Drain', 'Source' and 'Gate' of conventional transistor. The red arrows showing at right top indicate the external in-plane magnetic field directions of H_{sat} *and* H_a*.[158]*

Inspired by this, we have designed a Y-shaped nanowire (as shown in Figure 6.1d) to implement the function similar to that of a conventional semiconductor transistor. The 'Gate' arm has the same effect as the 'insulated gate' in the transistor. The magnetization direction of this 'Gate' arm (restricted arm) controls the domain propagation process of the 'Drain' and 'Source' arm (switching arms)[159]. The domain wall pinning and depinning state in Y junction correspond to 'gate on' and 'gate off', respectively, at the same input condition (as shown in Figure 6.2).

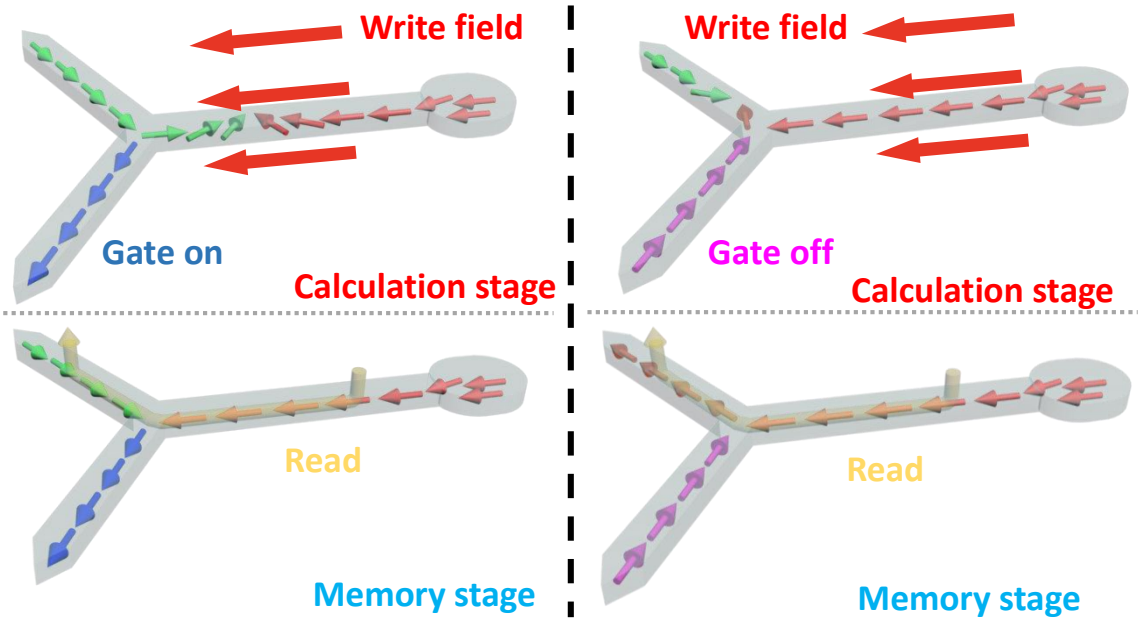

Figure 6.2 Schematic diagrams of operation to a Y-shaped nanowire both in calculation stage and memory stage. Left diagrams illustrate that when the 'Gate on', the domain wall pinned at the joint during write field, and the read process will detect a higher conductive at memory state. Conversely, lower conductive will be detected by the read current at same write field due to the 'Gate off' showing on the right diagrams.[158]

By controlling different magnetization states of three arms, several basic Boolean logic functions can feasibly perform under two input signals. Based on this phenomenon, a programmable logic gate with functions including OR/NAND/XOR is achieved within only one nanostructure. Furthermore, comparing with the conventional CMOS-Based computer architecture (as shown in Figure 6.1a), this DWL can either process input signals or store output results that breaks the physical separation between the memory and computing. Instead of reading data and writing back process, spin-based logic is stored and operated in memory with a single writing instruction (as shown in Figure 6.1c). After receiving the instruction, a series of input signals will change the spin state of three arms, which is called the calculation stage. Subsequently, at the memory stage, the spin state is stored in two switching arms. There are two different spin states, namely "head to head" (domain wall exists) and "head to tail" to yield different outputs [119, 160, 161] (operations are illustrated in Figure 6.2). This architecture, which combines ease of fabrication and integration for in-memory computing, fills the gap in the simplification of complex logic gates either in a conventional integrated circuit or the previously proposed DWL[43, 45, 46, 162].

6.3 Experiment and simulation results

6.3.1 Design and fabrication of Y-shaped nanostructure

The design of Y-shaped nanostructures were done via AutoCAD by myself. The idea of this special nanostructure is based on the transistor and magnetization interact with near constructer. The specific designs of Y-shaped nanostructures with numeric annotation are showing in the figure 6.3. The angle between the three arms of Y-shaped nanowire are equal to 120°. This angle design, which is symmetrical to the central axis, allows each arm to be subjected to the same effect under the external magnetic field. The different length of 'source' and 'drain' arm can let us to investigate the influence of magnetization caused by the length difference.

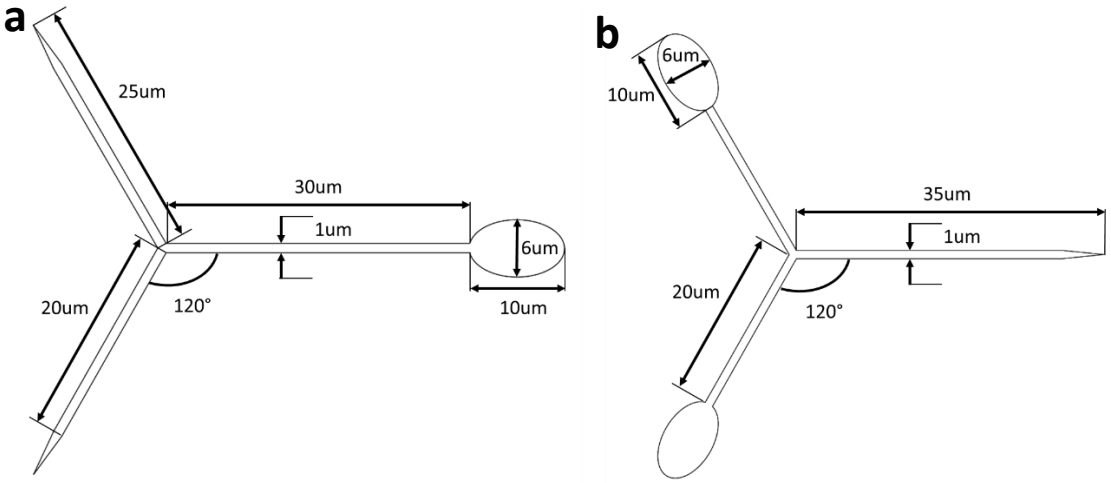

Figure 6.3 Design diagrams of Y-shaped nanowire with one and two nucleation pads for a, b respectively.

The undoped Si wafer was cleaned and coated with PMMA e-beam resist. Exposure doses were carefully adjusted to achieve the fine structures using e-beam lithography. Metal deposition was then done with permalloy $Fe_{20}Ni_{80}$ (30nm-thick) and Au (5nm-thick) as capping layer. This was followed by lift off process to complete the sample fabrication.

6.3.2 Experimental section

The Y-shaped nanowires were made from the magnetically soft Permalloy ($Ni_{80}Fe_{20}$) by e-beam lithography. Magnetization analysis was performed with a magneto-optical Kerr effect (MOKE) image system[163]. The successive images were taken at each applied in-plane sweep magnetic field in 1.44mT steps. The MOKE result was extracted from the average of 5 times full loop sweep signal. Same experiment was repeated for

three times. Figure 6.1(d) shows a SEM image of Y-shaped nanostructure with one nucleation pad (maximum width 6μm, maximum length 10μm). The angle between the three arms of Y-shaped nanowire are equal to 120°. 'Drain' arm and 'Gate' arm are 1μm width, 25μm length (from joint to the tail), and 'Source' arm is 1μm width, 30μm length. For the nanowire design, the large ratio of length to width can yield strong shape anisotropy enough to overcome the driven magnetic field to ensure the functionality of nanowire device. H_{sat} (±350mT) indicates initial applied saturated field along 'Gate' arm ($x - \theta'$ ($\theta' = 60°$)) and an orthogonal external field H_a (the range of change is -350mT to 350mT) is then exerted along the $x + \theta$ where θ is 30°.

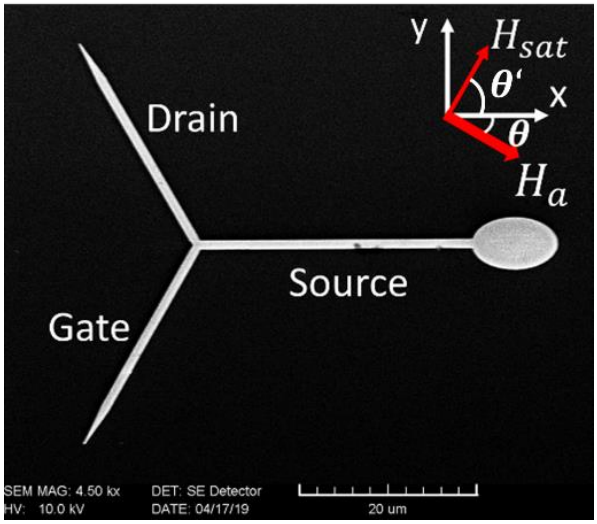

Figure 6.4 SEM image of transistor-like permalloy Y-shaped nanowire with one nucleation pad. Three arms correspond to the 'Drain', 'Source' and 'Gate' of conventional transistor. The red arrows showing at right top indicate the external in-plane magnetic field directions of H_{sat} and H_a.

In addition to one nucleation pad Y-shaped nanostructure, we design another similar design of Y-shaped nanostructure with two nucleation pads which aimed to reduce the magnetic field required for gate reversal. The Scanning electron microscope (SEM) image is shown in Figure 6.4. The three angles between the arms, which have the same definition as 'Source' and 'Drain' and 'Gate', are equal to 120°. 'Source' and 'Gate' arms are 1μm width, 25μm length, and 'Drain' arm is 1μm width, 30μm length. The two nucleation pads are the same size with the maximum width of 6μm and maximum height of 10μm.

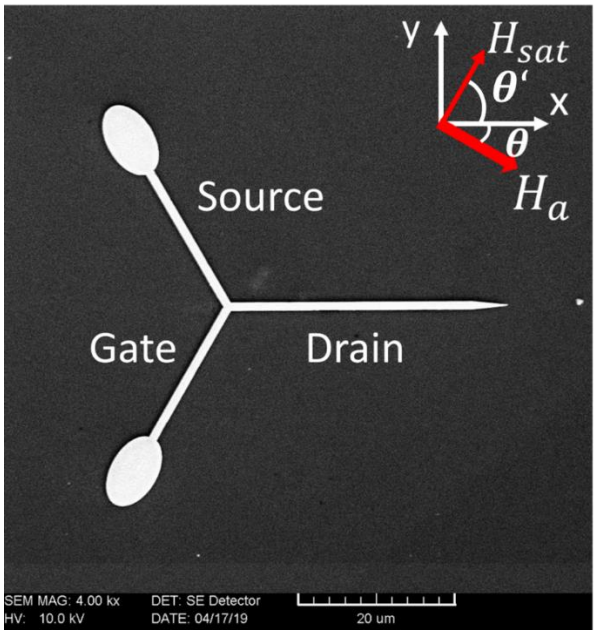

Figure 6.5 SEM image of Y-shaped permalloy nanowire structure with two nucleation pads. 'Source' and 'Drain' and 'Gate' on the wires indicate the positions of sampling area for measurement of longitudinal Kerr effect. The red arrows indicate the external in-plane magnetic field directions of H_{sat} *and* H_a.

6.3.3 Experiment and simulation results

Figure 6.6 represent the Kerr contrast images and continuous magnetization progress within the structure. Before the Kerr imaging, the sample was first saturated at magnetic field H_{sat} as an initial state. The Gate arm controlled by the Y_{input} along the H_{sat} $(x - \theta'$ $(\theta' = 60°))$ which saturates the 'Gate' arm and controls its magnetization direction, also influences the magnetization of the 'Source' and 'Drain' arms. The nucleation pad's magnetization was firstly reversed and pushed the domain wall along the 'Source' arm to be pinned at the junction. After that, the magnetization of 'Gate' arm reversed, and eventually the 'Drain' arm magnetization switched. The result, as shown in Figure 6.6, indicates that the domain wall propagation needs less energy than magnetization process along the easy axis. This result also indicates that the Y_{input} should be the first input to set the nanostructure at the initial state otherwise it will impact the other two switching arms.

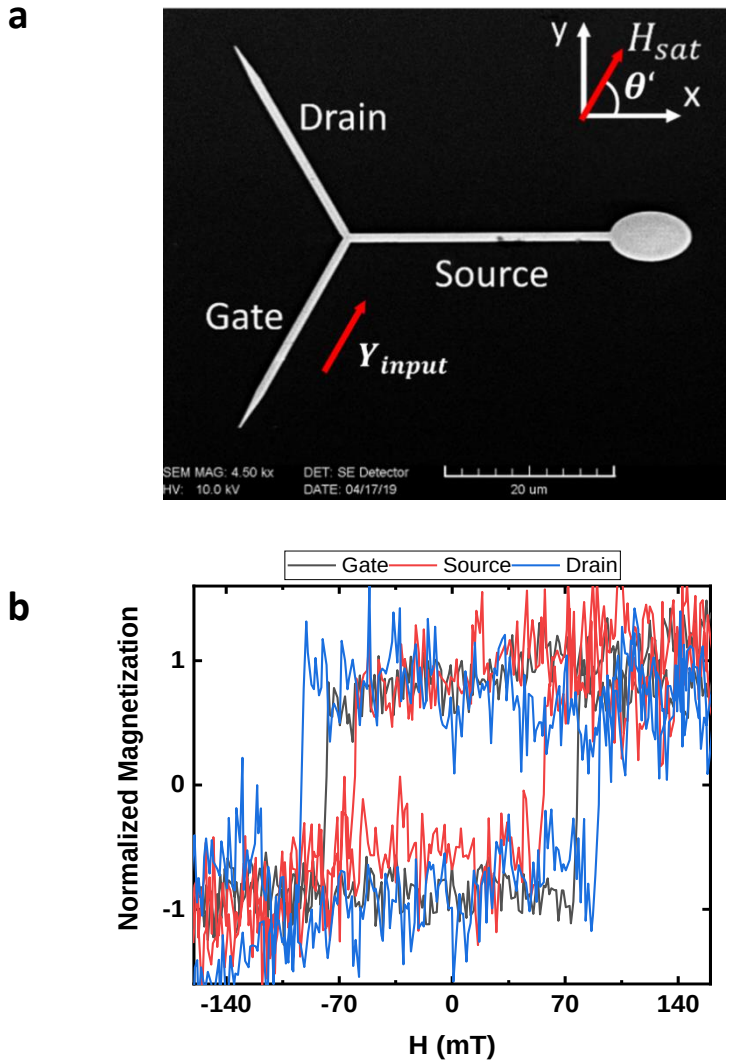

Figure 6.6 (a) SEM image shows the nanostructure with one nucleation pad and applied in-plane magnetic field direction Y_{input} (same with H_{sat}) represented by red arrow. (b) Hysteresis loop taken from three arms represent different coercivity. The external magnetic fields were swept in 1.44 mT steps from negative saturation (-350 mT) to positive saturation (350 mT) and return.

Subsequently a continuous sweeping magnetic field H_a is applied to the sample along $(x + \theta)$. Under the sweeping magnetic field which started from negative to positive and sweeping back, the magnetization state of entire device is changing via applied external field. Four Kerr images (Figure 6.7a to d) experiencing different applied field were picked up from the whole process.

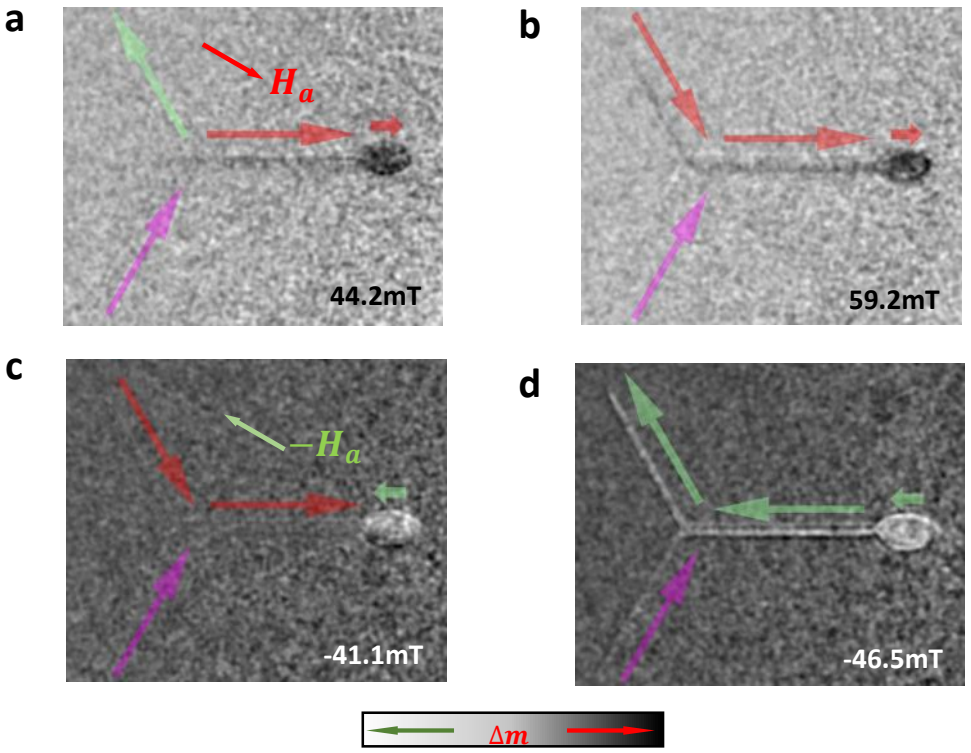

Figure 6.7 Contrast images show two opposite magnetization processes of Y-shaped nanowire with one nucleation pad at one of Gate states (a to d). Contrast here was generated by dividing the two different initial state image (m_1) by the specific image (m_x) resulting in a magnetization distribution $\Delta m = m_1/m_x$. Various colour arrows represent the magnetization direction along the three arms and nucleation pad that assist the reader's interpretation of the contrast. The magnetization of 'source' and 'drain' arm under H_a and $-H_a$ sweeping external field are exhibited in a and b, c and d respectively.[158]

The magnetization reversal first occurs at nucleation pad and then the domain wall formed between the arm and the nucleation pad is pushed along the 'Source' arm (Figure 6.7a). The domain wall passes the joint after depinning and subsequently moves to the terminal of 'Drain' arm (Figure 6.7b), leading to a magnetization direction reversal of the 'Drain' arm. Due to the strong magnetic shape anisotropy in narrow FM (ferromagnetic) wire, the magnetization direction (magenta arrow shown in Figure 6.7a to d) of the 'Gate' arm is restricted to be directed parallel to the wire axis under orthogonal magnetic field H_a. Two switching arms experience different magnetization process under magnetic field sweep back from positive to negative (as shown in Figure. 6.7c and b). After the domain wall leaves the nucleation pad, it propagates from 'Source' arm to 'Drain' arm without pinning, meanwhile 'Gate' arm remains its magnetization direction pointing from the terminal to joint.

For ease of observation, we combine the hysteresis loops taken from 'Source' arm and 'Drain' arm under sweeping magnetic field showing in Figure 6.8. A significant different coercivity (approximately 15mT) of the 'Source' and 'Drain' arm can be clearly observed from Figure 6.8 under a positive magnetic field. This coercivity bias

indicates asymmetric magnetization of the 'Drain' and 'Source' arm.

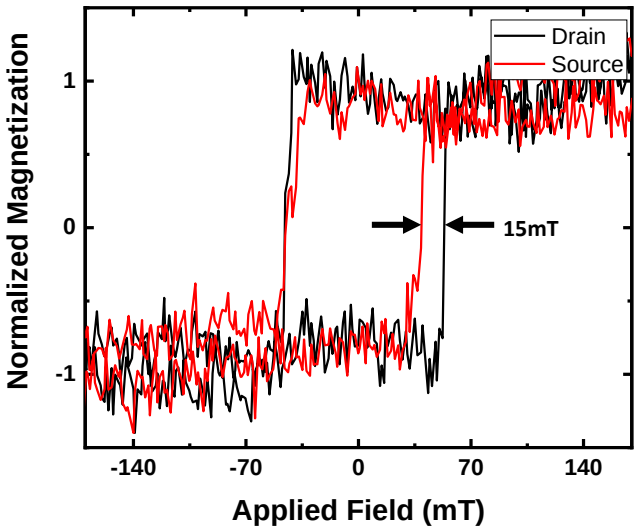

Figure 6.8 Longitudinal MOKE signal taken from 'Drain' arm and 'Source' arm corresponding to black and red hysteresis loop show an asymmetric magnetization process. Approximately 15mT pinning field occurred during the process of the sweep field from negative to positive.

In the opposite spin state (blue arrow in Figure 6.9a to d) of the 'Gate' arm, the 'Drain' arm and 'Source' arm exhibit opposite magnetization processes at the same experimental method. The domain propagates from 'Source' arm to 'Drain' arm without pinning appearing during negative to positive field reversal (Figure 6.9a and b). Domain wall pinning occurred during positive to negative field (Figure 6.9c and d).

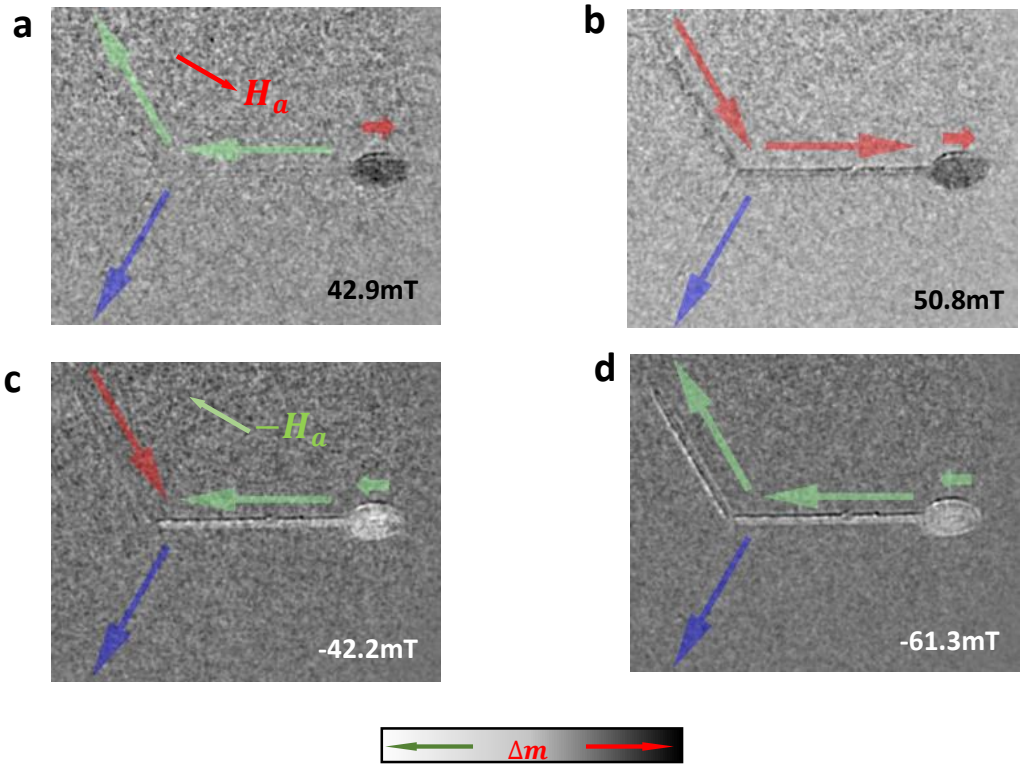

Figure 6.9 Contrast images show two opposite magnetization process of Y-shaped nanowire with one nucleation pad at one of another Gate states (a to d). Contrast here was generated by dividing the two different initial state image (m_1) by the specific image (m_x) resulting in a magnetization distribution $\Delta m = m_1/m_x$. Various colour arrows represent the magnetization direction along the three arms and nucleation pad to assist the reader's interpretation of the contrast. The magnetization of 'source' and 'drain' arm under H_a and $-H_a$ sweeping external field are exhibited in a and b, c and d respectively.[158]

Comparing with Figure 6.8, an opposite offset coercivity around 19mT can be observed under a negative external field at the opposite spin state of 'Gate' arm as shown in Figure 6.10. This asymmetric magnetization process shows that the spin state of the 'Gate' arm determined by the external magnetic field can control the magnetization of the 'Drain' arm, which has the similar function of a transistor in the conventional circuit.

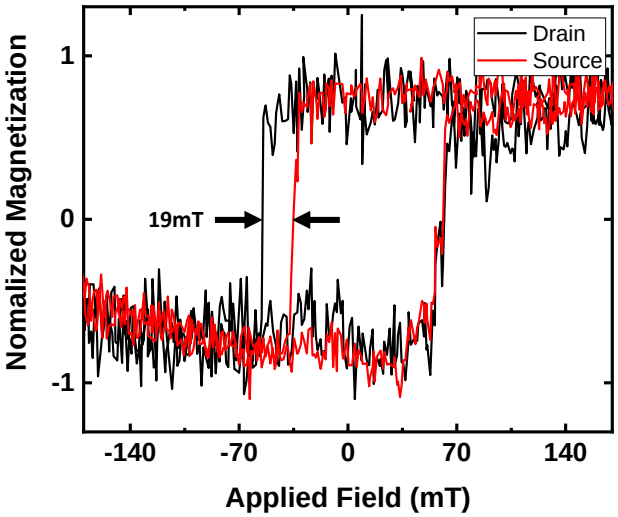

Figure 6.10 Longitudinal MOKE signal taken from 'Drain' arm and 'Source' arm corresponding to black and red hysteresis loop show an asymmetric magnetization process. Approximately 19mT pinning field occurred during the process of the sweep field from positive to negative.

To gain understanding of the domain-wall motion within the nanowire in detail, we performed quasi-static micromagnetic simulations of the Y-shaped nanostructure with one nucleation pad showing in Figure 6.11. The micromagnetic simulations are performed by Mumax3 simulation package[133]. The parameters of the device material in the micromagnetic simulation are given as blow, the exchange stiffness $A_{ex} = 13 \times 10^{-12} j/m$, the crystalline anisotropy constant $\mathrm{K} = 0 j/m^3$, saturation magnetization $M_s = 8.6 \times 10^5 A/m$ and for the quasi-static simulations the Gilbert damping constant $\alpha = 0.5$. The cell size for the 2D micromagnetic simulation is $5\mathrm{nm} \times 5\mathrm{nm} \times 20\mathrm{nm}$.

The simulation results showed that the domain switching process is similar to the

function of the transistor. For the domain-wall pinning situation (Figure 6.11a), there is a transverse domain-wall generated at the junctions showing in the enlarge image. Meanwhile, the magnetizations along the 'Gate' to 'Drain' arm and 'Gate' to 'Source' arm are the head-to-tail. Thus, the domain depinning needs to overcome an energy barrier. Further increasing the applied field, the transverse domain-wall overcomes the barrier and propagates to 'Drain' arm (Figure 6.11b). Under opposite magnetic field, three arms appeared to have head-to-head domain configurations with the domain-wall approaching to the junction. This led the domain wall to propagate directly along an easy magnetization direction to 'Source' arm, where 'Gate' arm is a hard magnetization axis along the external field due to strong shape anisotropy (Figure 6.11c and d). Since the device was applied sweeping magnetic field, the initial and final magnetization state are totally same (as shown in Figure 6.11d). Moreover, the reduced size simulation results indicate that the performance of device can be maintained by scaling down to nanometer, which provides a theoretical basis for the future high-density in-memory computing network.

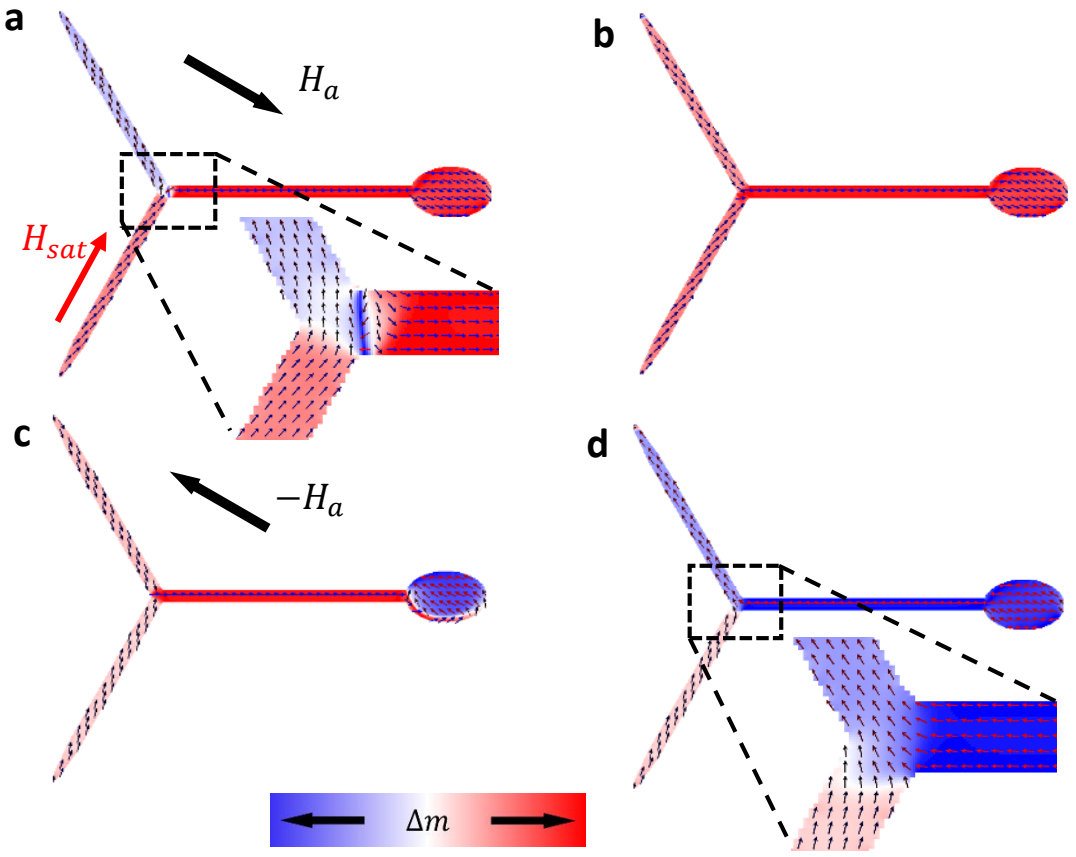

Figure 6.11 A series of simulation results (a) to (d) showing the detail of magnetization process for Y-shaped nanowire at initial saturated field along $y + \theta$ for H_{sat}. The enlarge figures of simulation results indicate more details of magnetization direction inside the junction.

The hysteresis loops for X-axis magnetization from one pixel state at two arms (Figure 6.12) are a red square loop ('Source' arm, parallel to the X-axis) and a gray

oblique loop ('Drain' arm, an $60°$ angle with X-axis). This result indicates that an asymmetric magnetization process takes place on the 'Drain' arm, which is exactly the same as the experimental observation.

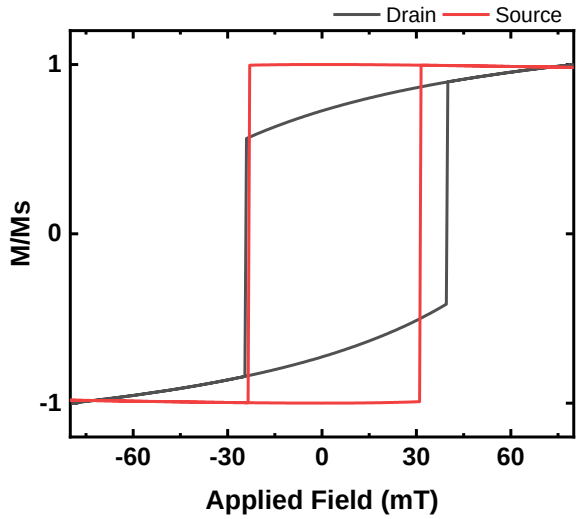

Figure 6.12 Hysteresis loop taken from two pixels at 'Drain' arm and 'Source' arm corresponding to H_{sat}.

Instead of applying H_{sat} as an initialization in the simulation, opposite magnetic field $-H_{sat}$ was also applied to set up the initial state. As external field $-H_{sat}$ applied along the 'Gate' arm, the magnetization direction along this arm is from joint to the terminal which shows the blue background in Figure 6.13. The same sweeping magnetic field was applied to this simulation, however, the direct propagation process appeared first (Figure 6.13a and b) and subsequently domain-wall pinning state (Figure 6.13c and d) occurred under reversed field condition.

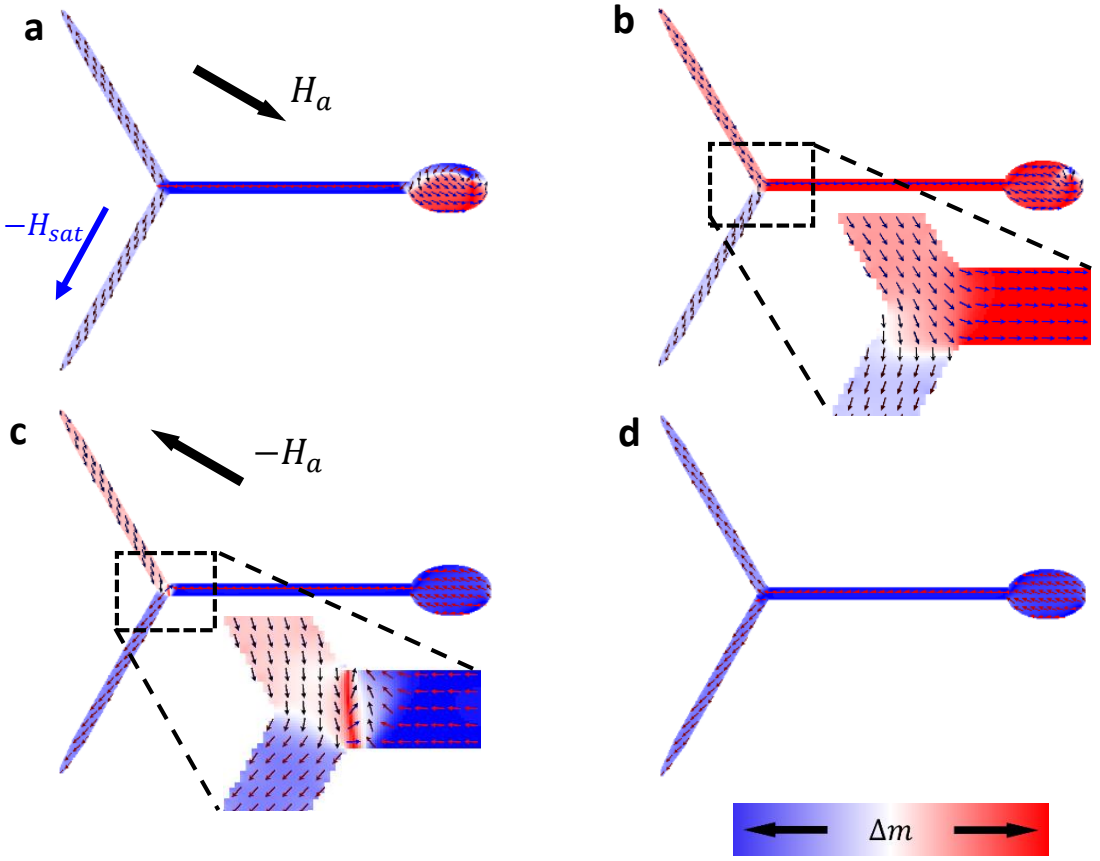

Figure 6.13 (a) to (d) represent magnetization process under same sweeping magnetic field condition at opposite $-H_{sat}$ saturated field as initialization. The enlarge figures of simulation results indicate more details of magnetization direction inside the junction.[158]

Comparing with pervious simulation hysteresis loop (Figure 6.12), Figure 6.14 represents the opposite asymmetric magnetization process due to a reversed initial spin state of 'Gate' arm. All the simulation results are in good agreement with the experiment.

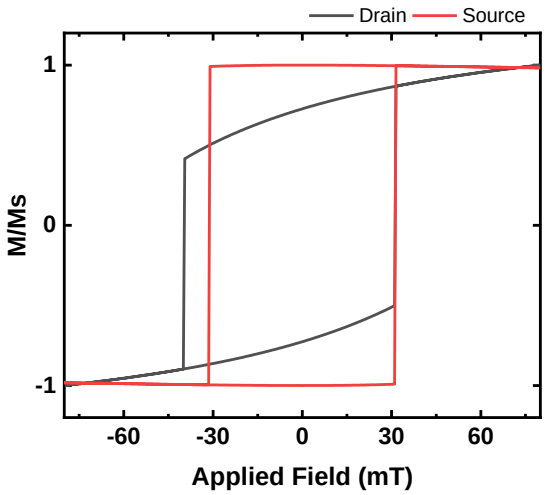

Figure 6.14 Hysteresis loop taken from two pixels at 'Drain' arm and 'Source' arm corresponding to $-H_{sat}$ saturated field.

According to these simulation and experiment result, the magnetization direction of 'Gate' arm and the 'Source' arm, which is directly connected with nucleation pad, plays a decisive role in this transistor-like magnetic nanostructure. Our simulation results (figure 6.11 and 6.13) indicate that the gate arm magnetization impacted by the external magnetic field and it's not exactly along the arm axis. This switching behavior of 'Gate' arm is attributed to the result of both external magnetic field and shape anisotropy. Since the asymmetric results mainly come from the along or opposite magnetization directions of the 'Source' and 'Gate' arm (such as head-to-tail or head-to-head), therefore, a slightly changes in the direction of the 'Gate' arm magnetization will not significantly affect the functions. The simulation results represent agreements to the experimental phenomenon under large amount of repeated experiment summarized. This Y-shaped nanostructure with the required functionality observed reliably shows the feasibility to develop logic unit or integrated logic networks.

In addition, another design of Y-shaped nanostructure with two nucleation pads (as shown in the figure 6.5) which has been investigated by the same method. In order to investigate the influence of magnetization along the 'Source' and 'Drain' arms when Y_{input} applied along the H_{sat} $(\mathrm{x}-\theta'$ $(\theta'=60°))$ as an initial input, the same experiment operation proceeded on the Y-shaped nanowire with two nucleation pads. Due to the external field along the 'Gate' arm easy magnetization axis, the spin state reversal process firstly occurred on the attached nucleation pad and push domain wall along the 'Gate' arm among the three arms. And subsequently the domain-wall propagation took place from another nucleation pad to 'Source' arm. Finally, the 'Drain' arm reversed. The result, as shown in Figure 6.15, exhibits advantage over the nanostructure with one nucleation pad in term of low energy consumption due to the weaker saturated field needed along the 'Gate' arm attached with a nucleation pad. Comparing with Figure 6.6, the saturation field of the gate arm is reduced from 77mT to 35mT.

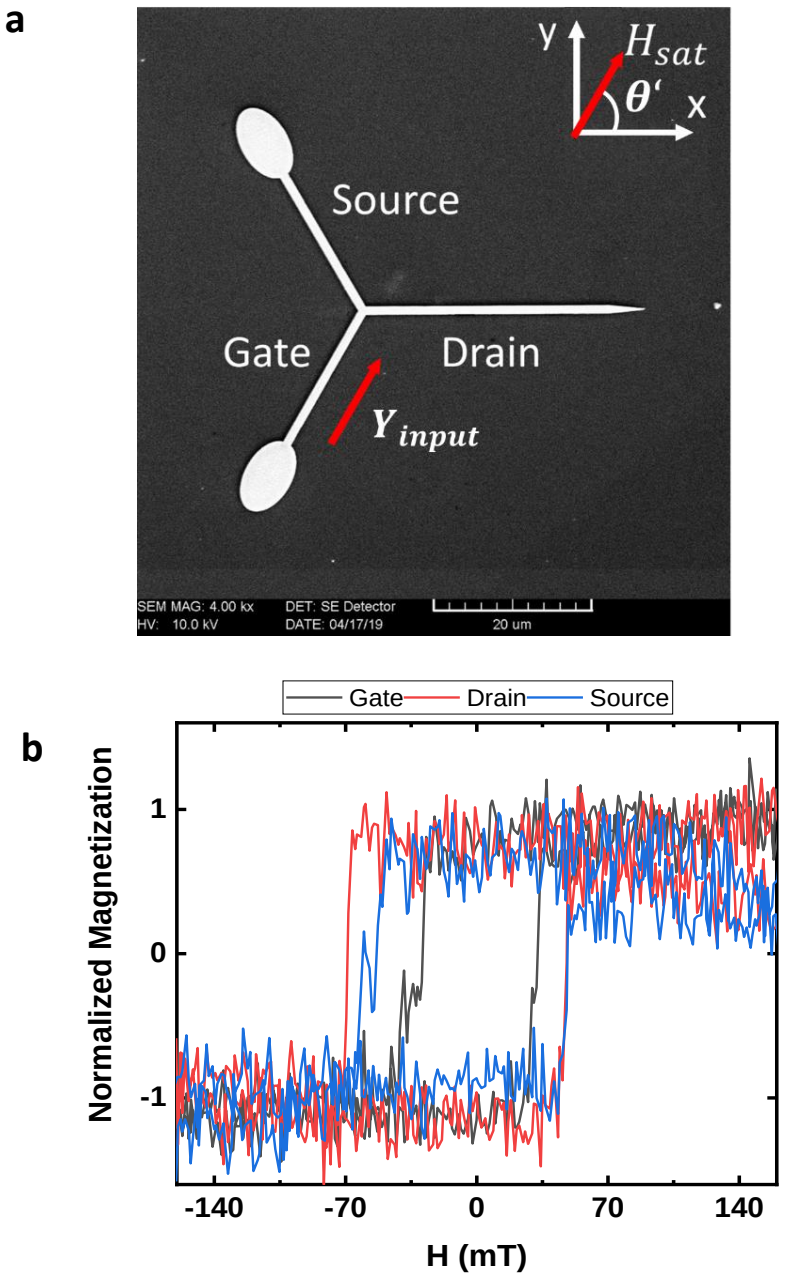

Figure 6.15 (a) SEM image shows the nanostructure with two nucleation pads and applied in-plane magnetic field direction Y_{input} (same with H_{sat}) represented by red arrow. (b) Hysteresis loops taken from three arms show different coercivities. The external magnetic fields were swept in 1.44 mT steps from negative saturation (-350 mT) to positive saturation (350 mT) and then returned.

Same experiment operation applies on this nanostructure. Although the nucleation pad connected with 'Gate' arm's magnetization switched under sweeping applied field, the 'Gate' arm still maintained its initial spin state (magenta arrow shown in Figure 6.16). This shows that the energy of propagation cannot overcome the energy barrier of shape anisotropy.

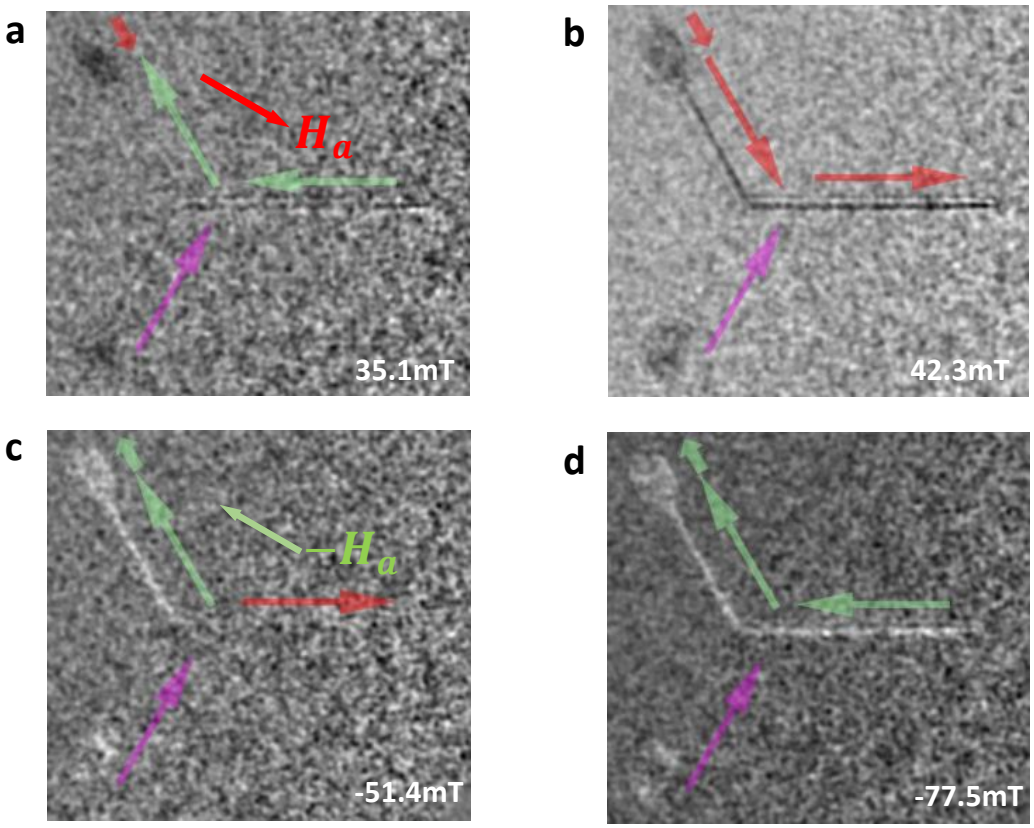

Figure 6.16 Contrast images show two opposite magnetization processes of Y-shaped nanowire with two nucleation pads at one of Gate states (a to d). Contrast here was generated by dividing the two different initial state image (m_1) by the specific image (m_x) resulting in a magnetization distribution $\Delta m = m_1/m_x$. Various colour arrows represent the magnetization direction along the three arms and nucleation pad that assist the reader's interpretation of the contrast. The magnetization of 'source' and 'drain' arm under H_a and $-H_a$ sweeping external field are exhibited in a and b, c and d respectively.[158]

A combination of the hysteresis loops taken from 'Source' arm and 'Drain' arm under sweeping magnetic field is showing in Figure 6.17. A significant different coercivity (approximately 25mT) of the 'Source' and 'Drain' arm can be clearly observed from Figure 6.17 under a positive magnetic field. This coercivity bias indicates asymmetric magnetization of the 'Drain' and 'Source' arm.

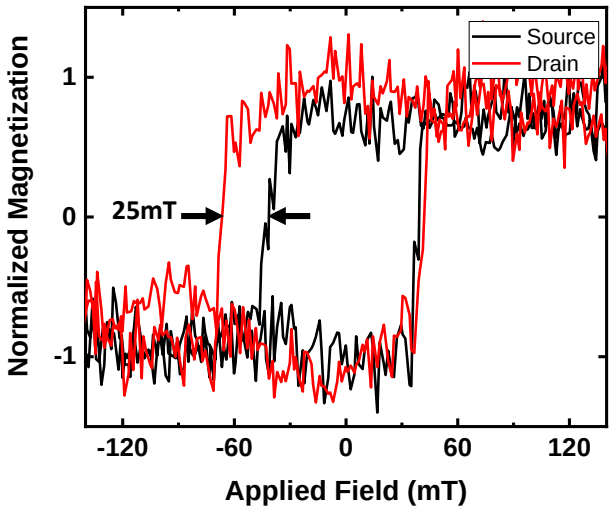

Figure 6.17 Longitudinal MOKE signal taken from 'Drain' arm and 'Source' arm corresponding to red and black hysteresis loop show an asymmetric magnetization process. Approximately 25mT pinning field occurred during the process of the sweep field from negative to positive.

In the opposite spin state (blue arrow shown in Figure 6.18a to d) of the 'Gate' arm, the 'Drain' arm and 'Source' arm exhibit opposite magnetization process at the same experimental method. The magnetization of two nucleation pads presents the same phenomenon of one nucleation pad nanostructure.

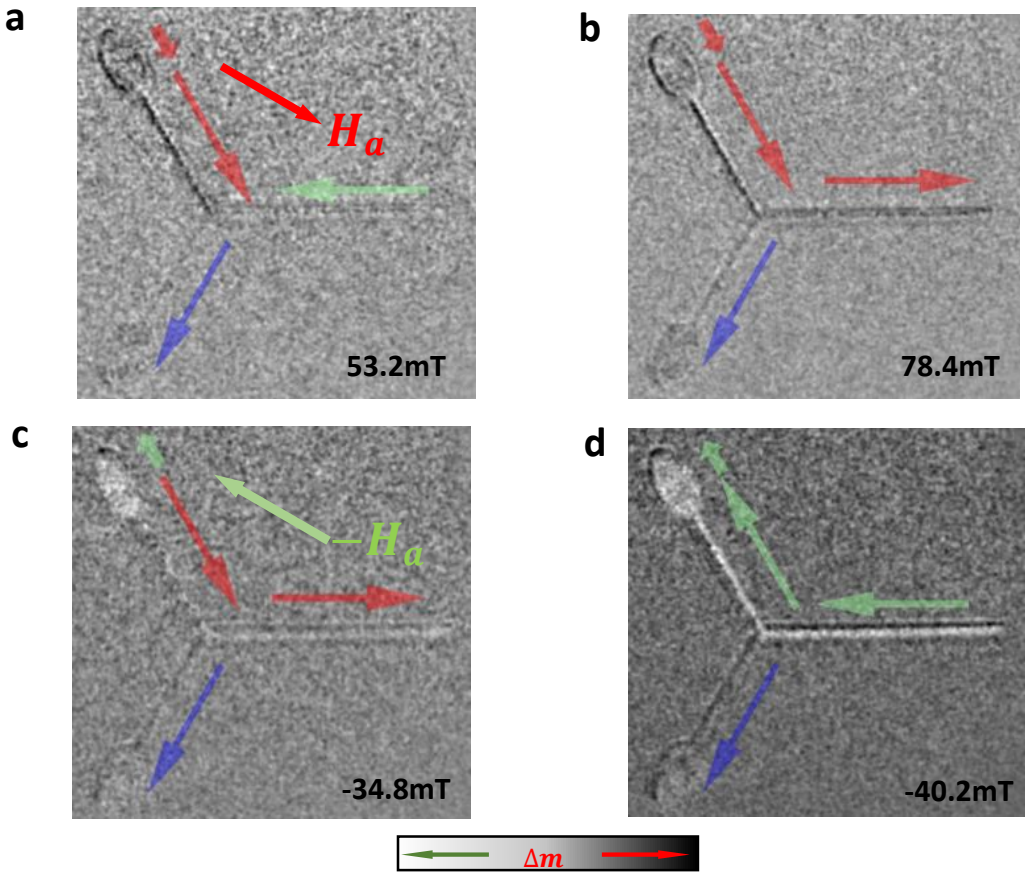

Figure 6.18 Contrast images show two opposite magnetization processes of Y-shaped nanowire with two nucleation pads at another of Gate states (a to d). Contrast here was generated by dividing the two different initial state image (m_1) by the specific image (m_x) resulting in a magnetization distribution $\Delta m = m_1/m_x$. Various colour arrows represent the magnetization direction along the three arms and nucleation pad that assist the reader's interpretation of the contrast. The magnetization of 'source' and 'drain' arm under H_a and $-H_a$ sweeping external field are exhibited in a and b, c and d respectively.[158]

Comparing with Figure 6.17, an opposite offset coercivity around 24mT can be observed under a negative external field at the opposite spin state of 'Gate' arm as shown in Figure 6.19.

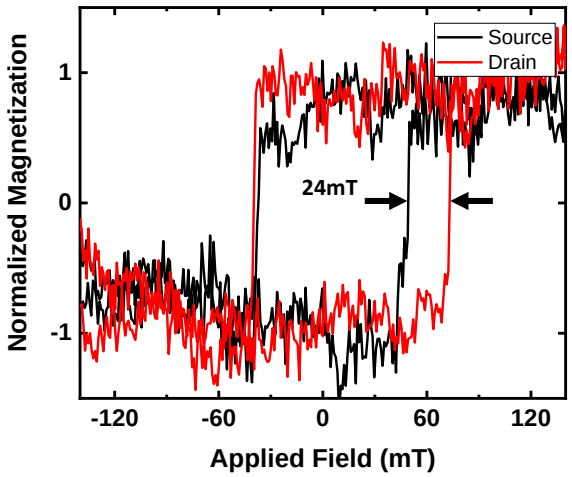

Figure 6.19 Longitudinal MOKE signal taken from 'Drain' arm and 'Source' arm corresponding to red and black hysteresis loop show an asymmetric magnetization process. Approximately 24mT pinning field occurred during the process of the sweep field from positive to negative.

This comparison of experiment shows that the length of two switching arms does not impact this asymmetric magnetization process, but the magnitude of coercivity bias (25mT) can be affected by the length of 'Source' and 'Drain' arm. When the 'Source' arm is shorter than the 'Drain' arm, this coercivity offset will be larger (comparing Figure 6.8 and 6.10 with Figure 6.17 and 6.19).

To gain understanding of opposite asymmetric magnetization that occurred with different design of two nanostructures, same simulation method was applied to the Y-shaped nanostructure with two nucleation pads, and the results are shown in Figure 6.20. The simulation results showed that the domain switching process is same to experimental result. The main difference between one nucleation pad and two nucleation pads nanostructures is that the additional pad attached with Gate arm change its magnetization under sweeping magnetic field. The Gate arm, however, still almost remain the magnetization but slightly change direction.

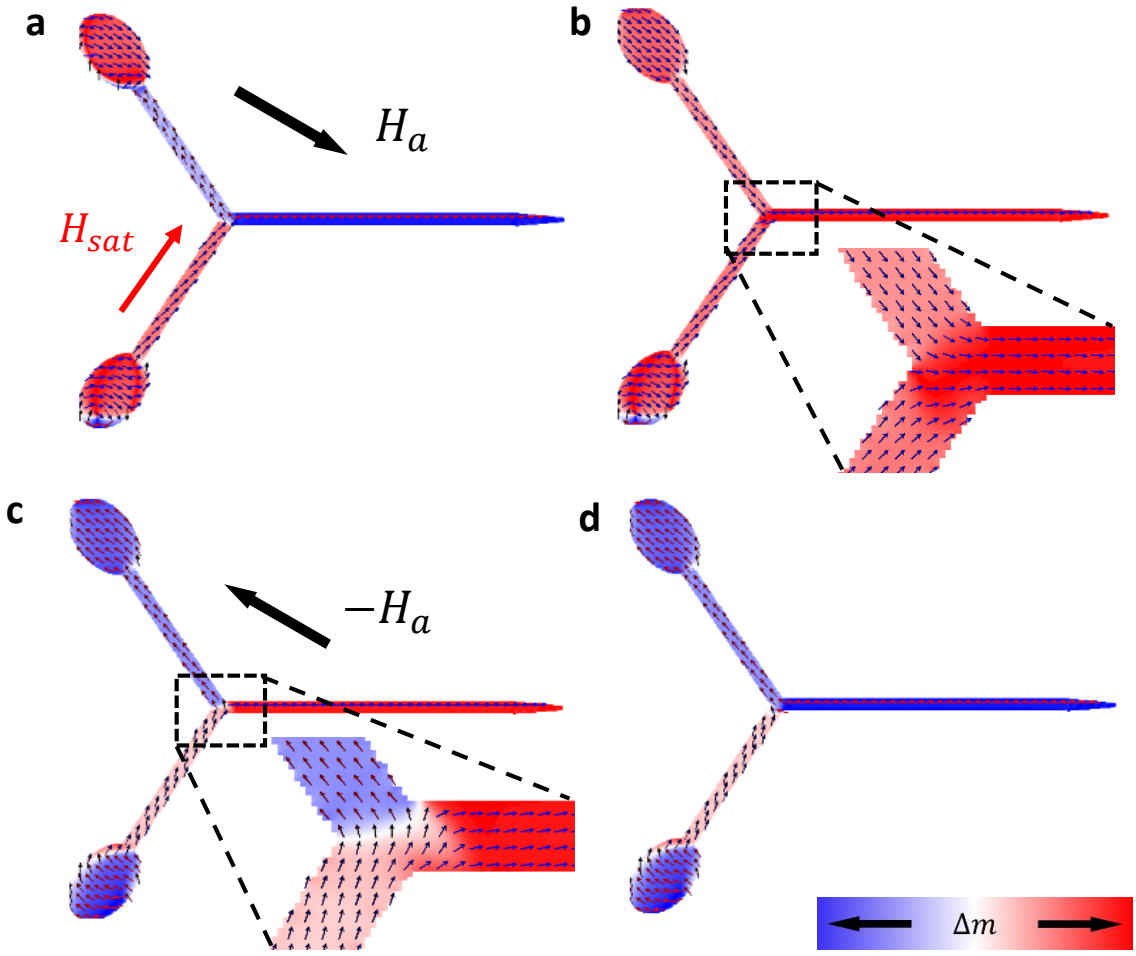

Figure 6.20 A series of simulation results (a) to (d) showing the detail of magnetization process for Y-shaped nanowire at initial saturated field along $y + \theta$ *for* H_{sat}*. The enlarge figures of simulation results indicate more details of magnetization direction inside the junction.*

The hysteresis loops for X-axis magnetization from one pixel state at two arms (Figure 6.21) are a red square loop ('Drain' arm, parallel to the X-axis) and a gray oblique loop ('Source' arm, an $60°$ angle with X-axis).

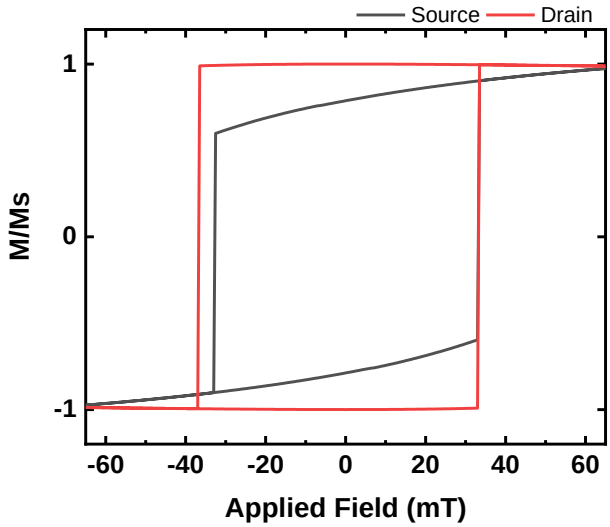

Figure 6.21 Hysteresis loop taken from two pixels at arm 'Source' and 'Drain'.

Instead of applying H_{sat} as an initialization in the simulation, opposite magnetic field $-H_{sat}$ was also applied to set up the initial state. As external field $-H_{sat}$ applied along the 'Gate' arm, the magnetization direction along this arm is from joint to the terminal which shows the blue background in Figure 6.22. The same sweeping magnetic field was applied to this simulation.

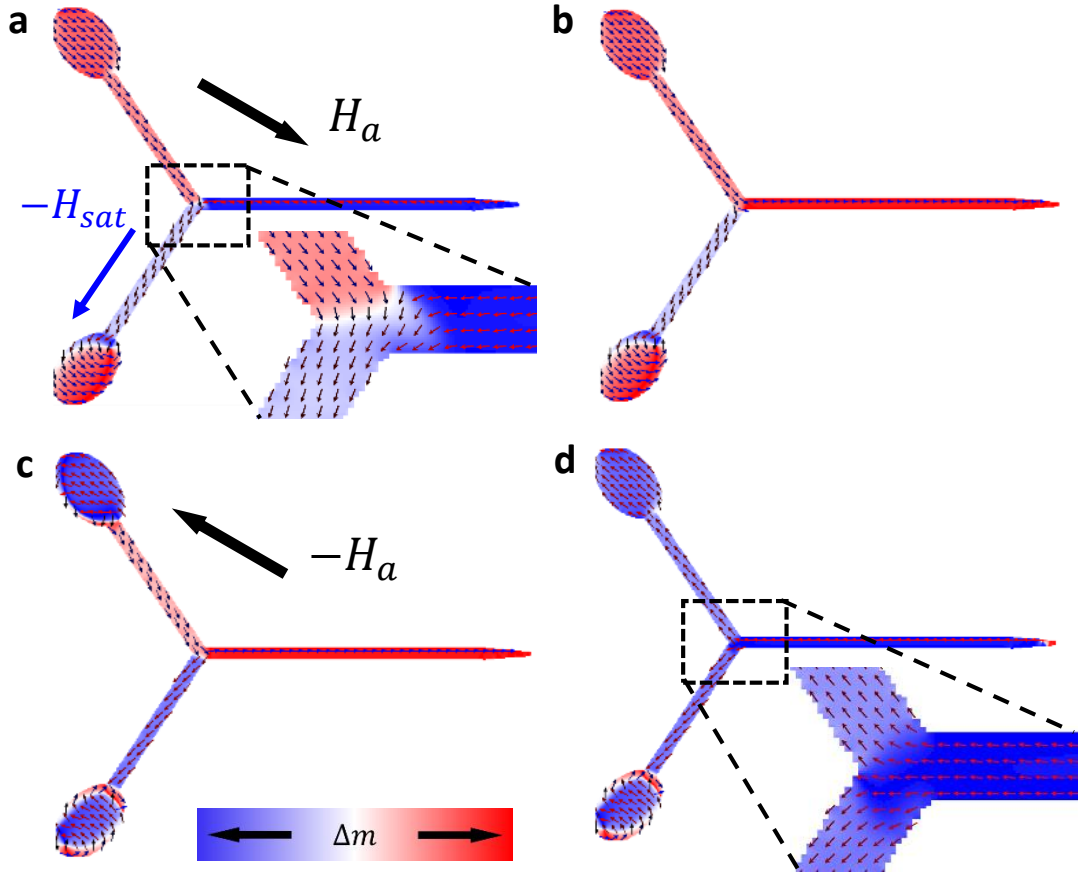

Figure 6.22 (a) to (d) represent magnetization process under same sweeping magnetic field condition at opposite $-H_{sat}$ saturated field as initialization. The enlarge figures of simulation results indicate more details of magnetization direction inside the junction.

Comparing with pervious simulation hysteresis loop (Figure 6.21), Figure 6.23 represents the opposite asymmetric magnetization process due to a reversed initial spin state of 'Gate' arm. All the simulation results are in good agreement with the experiment.

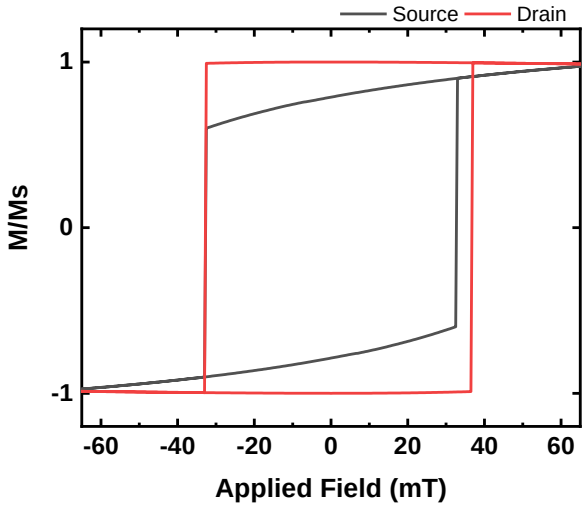

Figure 6.23 Hysteresis loop taken from two pixels at arm 'Source' and 'Drain'.

These simulation results provide further evidence that the gate arm's magnetization direction can control the pinning or depinning process of domain wall motion along the arm 'Source' and 'Drain'. Moreover, this restricted arm is very stable under the orthogonally applied field, which indicates the stability for spin logic applications.

6.3.4 Programmable logic gate based on Y-shaped nanostructure

Based on the observed transistor-like phenomenon, we propose a feasible programmable logic gate, where a universal design based on just one nanostructure is still lacking. The operating principles of magnetic programmable logic gate are illustrated in Figure 6.24 to 6.26. The key characteristic is that the output exhibits two different conductivity states for high ('1') or low ('-1') under two input external fields, where the two arms have different spin states due to the asymmetric magnetization process within the nanowire[158]. The differential conductivity of two different spin states when the current flow through has been reported by previous research[119, 122]. The input signal Y_{input} (same with H_{sat}), along the $x - \theta'$ ($\theta' = 60°$) which should be the first input, saturates the 'Gate' arm and controls its magnetization direction (H_{sat} refer to '1' and $-H_{sat}$ refer to '-1'). Subsequently, a set saturated field X_{set} that set to '1' $(x + \theta)$ or '-1' $(-(x + \theta))$, which initializes the magnetization of arm 'Source' and 'Drain' to same direction (head to tail magnetization state), can be used to control

the logic gate selection. Finally, a X_{input} along the $(x + \theta)$ or $(-(x + \theta))$ with '1/2' magnitude (the specific value depends on the specific structure) apply to this DWL. Here we illustrate three different logic gates function within one nanostructure.

OR GATE. We select the saturated field X_{set} to '+1' to implement the OR logic gate (Figure 6.24a to d). Noticeably, Y_{input} should be the first input to this nanostructure, otherwise it will impact the magnetization of other two arms. Each time after the Y_{input} applied, the saturated field X_{set} sets the 'Drain' arm and 'Source' arm to the same state. Subsequently X_{input} is applied to complete a cycle of logic calculation. Detecting the conductivity between the 'Drain' arm and 'Source' arm, we get the same function of OR gate representing in the Table 6.1. Due to the asymmetric magnetization process, the domain wall (Tail-to-Tail) is pinned at the junction (Figure 6.24a) under both 'high' input of X and Y, which represents low conductivity. Same direction of X_{input} and X_{set} cause no changing of two arms' magnetization (Head-to-Tail) (Figure 6.24b and d) which exhibit high conductivity. Figure 6.24c indicates the fast propagation process when 'low' Y_{input} and 'high' X_{input} are applied, and same magnetization direction along the 'Drain' arm and 'Source' arm. In summary, only 'low' input of both X, Y can yield 'low' output under the 'low' X_{set} setting saturated field.

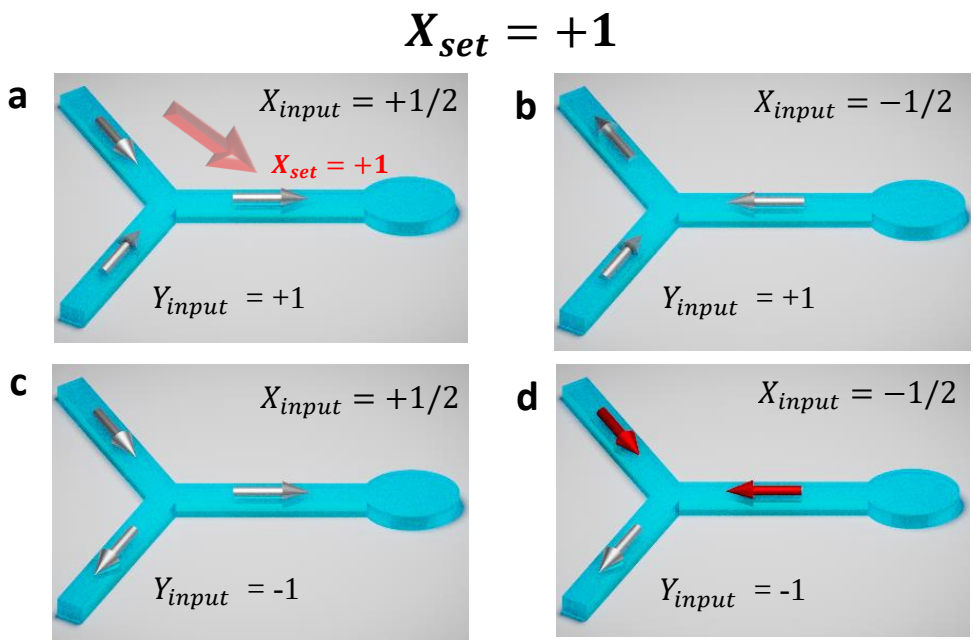

Table 6.1 OR GATE

$X_{set} = +1$		
X_{input}	Y_{input}	output
+1/2	+1	+1
-1/2	+1	+1
+1/2	-1	+1
-1/2	-1	-1

Figure 6.24 (a) to (d) exhibit the operation principle of OR gate. Under the '+1' X_{set} saturated field, the output represents low when only both low inputs come, and Table 6.1 illustrates the true table of this magnetic OR gate.[158]

NAND GATE. When '-1' of X_{set} setting saturated field was selected, this programmable magnetic logic gate switches to the NAND function (Figure 6.25a to d). With the same input signal applied to this nanostructure, we can only get the 'low' output under both 'high' input of X, Y. This function represents the same logic of NAND gate and true table shows in Table 6.2.

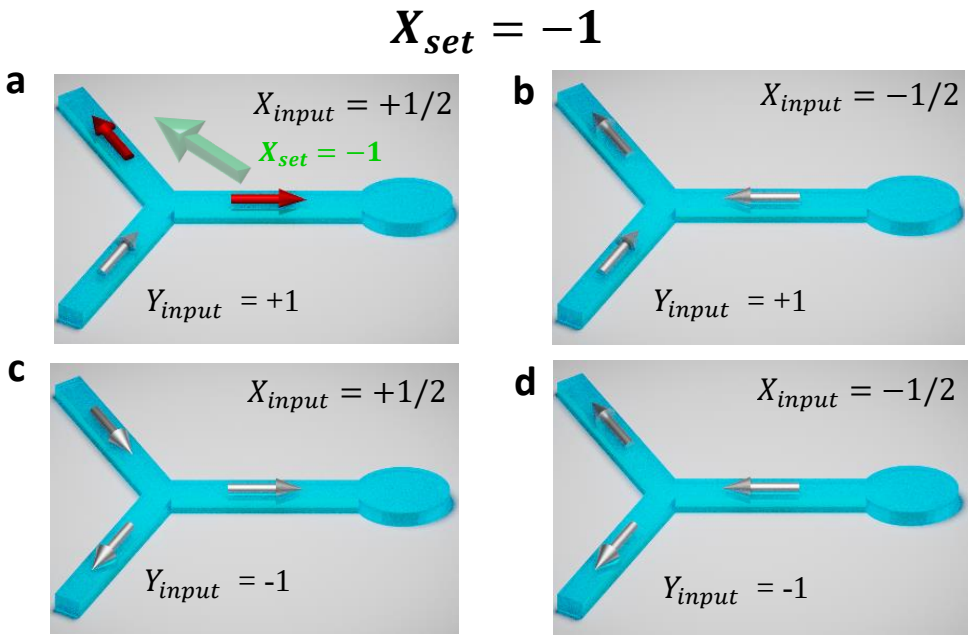

Table 6.2 NAND GATE

$X_{set} = -1$		
X_{input}	Y_{input}	output
+1/2	+1	-1
-1/2	+1	+1
+1/2	-1	+1
-1/2	-1	+1

Figure 6.25 (a) to (d) illustrate the operation principle of NAND gate. A low output yield when the both high inputs apply under '-1' X_{set} saturated field. The functions show in the Table. 2.[158]

XOR GATE. Different in the previous logic gate, the XOR function can be implemented under two opposite X_{set} setting saturated fields (shown as Figure 6.26a to d). The Y_{input} can trigger the direction of X_{set}. A corresponding opposite setting saturated field should be activated when Y_{input} is 'high' or 'low'. Due to the asymmetric magnetization, the output represents the same function of XOR gate that

gives a true (high) output when the number of true inputs is odd. And true table exhibits in Table 6.3. This XOR gate is a combination of part of OR gate and NAND gate. As shown in the Table. 3, the X_{set} and Y_{input} are bound, which means the X_{set} only related to Y_{input} in XOR gate state. In the real operation, the X_{set} and Y_{input} are executed by a same field driver which means a single input but control by opposite applied magnetic field directions.

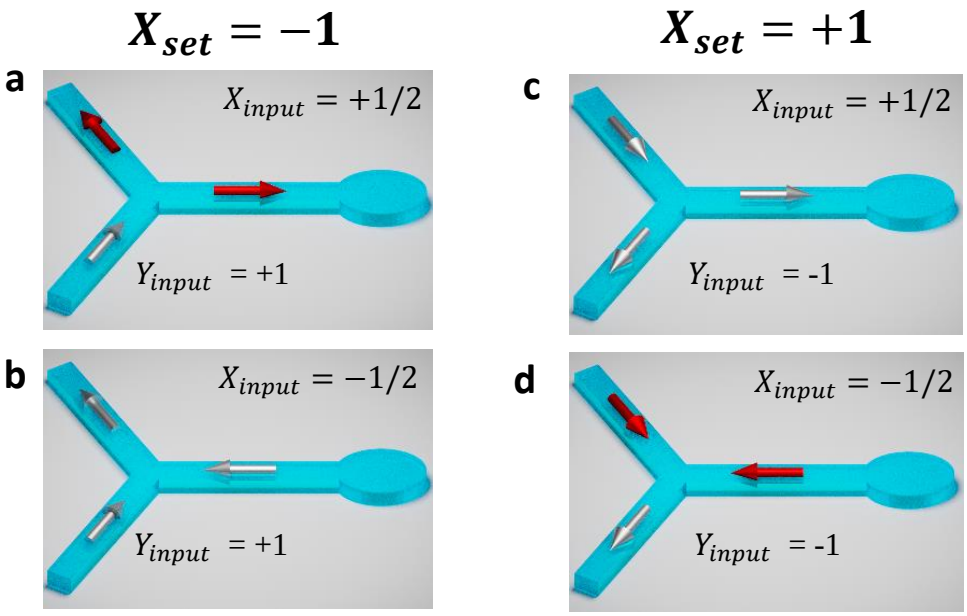

Table 6.3 XOR GATE

$X_{set} = -1$		
X_{input}	Y_{input}	output
+1/2	+1	-1
-1/2	+1	+1
$X_{set} = +1$		
+1/2	-1	+1
-1/2	-1	-1

Figure 6.26 (a) to (d) represent the operation principle of XOR gate. Y_{input} trigger the different X_{set} saturated field state. Output gives high when the number of true inputs is odd which exhibit in the Table 6.3.[158]

Furthermore, if we detect the resistance state of two arms rather than the conductivity, the relatively 'high' and 'low' value will be reversed. And this programmable logic could be extended three more logic functions. When '+1' of saturated field X_{set} is selected, the OR gate becomes AND gate due to the fact that all high inputs yield high output. And NAND gate is transferred to NOR because all low inputs yield high output under '-1' setting field X_{set}. Due to the opposite function, the XOR becomes NXOR where the same inputs yield high output. For translating the input signal to magnetic field, the extra field drivers are necessary. The value of '1' or '1/2'

refer to the magnitude of external field and they are fixed by each field driver. When the Y-shaped nanostructure is running, the driver switches the direction of the magnetic field according to the input digital signal 0 or 1 (- or +). Therefore, swapping the inputs will not violate the truth table and keep output value correct which satisfy the two inputs should be equivalent and commutable.

6.4 Summary and discussion

In this chapter, we report a transistor-like phenomenon occurred in Y-shaped magnetic nanostructure and demonstrate its functions by MOKE imaging and micromagnetic simulations. Based on the asymmetric magnetization process, we propose a feasible paradigm for in-memory computing programmable logic gate, which can significantly reduce the complexity and area of conventional logic circuits. Utilizing the characteristic of DWL for both storage and calculation, in-memory computing can be implemented more efficiently and directly. In general, this novel nanostructure can implement various Boolean logic functions and thus a real feasible spintronic programmable logic unit could be achieved. In this research, the external magnetic field and MOKE signal detection are the main investigation method. Further improvements could be achieved by patterned electrical contacts nanowire as an input pulse source[46, 164, 165]and patterned electrical pads as a detector of domain-wall electrical resistance[119, 122, 160].

Comparing with others implementation method of domain-wall based spintronic logic, such as Hiroyuki A et al[166], and Khalid A et al[116] which only can realize the calculation function, The key advantage of our design is that we can get the result from this device at the memory stage at any time. Our device calculation is dynamic, while the memory is static, which means that the data is saved in entire device operation.

To further implement the paradigm of the magnetic domain wall based in-memory computing, one may need to combine with one of these newly developed memory techniques including chirality-encoded DWL[46], STT-MRAM[16], Magnon-driven spintronic devices[167]. This Y-shaped nanostructure has a possibility to be cascaded with MTJs and construct in-memory computing network. In addition to domain-wall based logic unit, we can also use skyrmion to implement in memory computing construction. According to the previous chapter result, this Y-shaped nanostructure could apply to the CoFeB soft magnetic material system with skyrmion which can realize many kinds of logic functions. Moreover, the thermal gradient studied in the chapter 5 would be a good source for driven skyrmion motion in new design of logic unit for in-memory computing or neural network. While the gating-controlled operation of the Y-shaped magnetic nanostructure as demonstrated in this work provides an underlying framework for the in-memory computing architecture, significant efforts are still needed to address the interdisciplinary challenge of integrating spintronic ALU for calculating data and memory for storing data to achieve the practical in-memory computing.

Part 3 Conclusions and future work

7.1 Conclusions

In this thesis, I have studied the soft magnetic thin films and patterned devices with MOKE imaging technique. The spintronics based on magnetic skyrmion have potential usage in future digital computing devices. The thermal stability of CoFeB based MTJ structure play an important role in applications. The new concept of in-memory computing provides a straightforward advantage by eliminating the latency and energy burdens of memory wall. My work in this thesis is focused on these three topics which are summarized as the following

Defect-Correlated Skyrmions and Controllable Generation in Perpendicularly Magnetized CoFeB Ultrathin Films (chapter 4)

This work introduced different density of defects by inversing the growth order. Here, the defects represent the inhomogeneous anisotropic caused by sputtering. Then a STEM investigation is used to confirm the difference of defect density and the theoretical models is established. Based on this analysis, we made an experimental comparison of magnetic properties via MOKE imaging (square loop or curved loop). Through more experimental observations, we observed that skyrmion was generated in the more defects samples (curved loop), and found that skyrmion favor generation in certain specific locations. We thus proposed this phenomenon is defect-correlated skyrmions generation. We prepared two series of samples, proved different defect density in them, investigated the skyrmion generation rule, and proposed models to interpret it.

Therefore, this work establishes the intrinsic relationship between fabrication, microstructures, magnetization and the skyrmion generation in the MgO/CoFeB/Ta ultrathin films via the experiment and atomistic spin simulation. Those relationships have not been clarified in the previously works. The relationship between disorder and magnetic skyrmions has been a significant area of interest within the field of spintronics, and this work makes a strong attempt at improving the understanding of this field. The contribution of this work is to explain the relationship between disorder induced by fabrication and skyrmion generation through comparative experiments and atomics simulation modelling. This work enables to establish guidance from sample preparation to skyrmion generation and control.

The skyrmion generation and density control, which has not been systemically investigated, were proposed in this work via FORC technique. Different from other FORC experiments (based on VSM and MFM), the FOCR technique based on MOKE in this work reflects precisely the images corresponding with data. The fulfilled hysteresis loop via FORC can precisely exhibit the skyrmion generation and density

change versus external magnetic field. The stable skyrmion zone that outlined by FORC gives a guidance range and method of adjusting skyrmion with magnetic field.

Study on temperature dependent magnetic properties and perpendicular magnetic anisotropic gradients observed via temperature gradients induced (chapter 5)

The thermal stability is one of the most important indexes to measure the performance of the spintronics. It determines the retention time of magnetization state and threshold current for spin-transfer-torque magnetization switching. The thermal effect on soft magnetic materials is worth to study.

In this work, the CoFeB thin film was first measured under variable temperature via VSM. The saturation magnetization and effective perpendicular anisotropy field are monotonic reduction with increasing temperature, which indicates the effective perpendicular anisotropy energy also decay with rising temperature. At high temperature, the perpendicular anisotropy decreases rapidly and tends to become in-plane anisotropy.

Subsequently, the temperature dependent magnetic properties of CoFeB thin film have been investigated by MOKE imaging. The coercivity exhibits monotonic reduction with increasing temperature. The domain structure evolved shows significant change at different temperature. The domain width decreases with the increasing of temperature. This result can guide the design of spintronics in the future.

According to the characteristic of temperature dependent magnetic properties in CoFeB thin film, we designed a temperature gradient induced sample stage. The magnetic anisotropy gradient caused by in-plane temperature gradient was observed by MOKE microscopy. The domain width distribution indicates that the existence of magnetic anisotropy gradient. The method of magnetic anisotropy induced by temperature gradient has contribution to the study of materials' magnetic properties and applications in the future.

Paradigm of magnetic domain wall based In-memory computing (chapter 6)

Instead of re-optimizing conventional integrated circuits, in-memory computing, which is a new revolutionary concept, aims to subvert the von Neumann architecture by *in-situ* calculations, where the data are located. The DWL based on soft magnetic material such as Permalloy (NiFe) has been investigated for decades which has a strong potential to replace present logic gate. Motived by the conventional transistor, we proposed a new design with patterned Y-shaped NiFe nanowires by gate-controlling domain wall pinning and depinning.

Due to the strong shape anisotropy which can maintain the magnetization against external field, we set the three arms of this Y-shaped nanowire to source, drain and gate consistence with the concept of conventional transistor. Asymmetric magnetization could be obtained under different initial magnetization state of gate arm.

To further understand the principle of the mechanic for this device, we performed

quasi-static micromagnetic simulations of the Y-shaped nanostructure with one nucleation pad. The details of magnetization reversal and domain motion reveal that the spin direction along with or against between the two arms deterministically this asymmetric magnetization phenomenon.

In addition, another design of Y-shaped nanostructure with two nucleation pads which has been investigated by the same method. The results of experiment and simulation consistence with principle of transistor-like spintronics. The two nucleation pads nanostructure exhibits advantage over the nanostructure with one nucleation pad in term of low energy consumption due to the weaker saturated field needed along the 'Gate' arm attached with a nucleation pad.

Based on the observed transistor-like phenomenon, we propose a feasible programmable logic gate with functions including OR/NAND/XOR achieved within only one nanostructure, where a universal design based on just one nanostructure is still lacking. We demonstrated how this programmable logic gate works. This device preforms three different logic functions under different input set and the true table has been given.

In general, this thesis studies the soft magnetic material using the MOKE microscopy. From the study of soft magnetic material preparation to nanostructure fabrication and test, this study provides a complete investigation of soft magnetic material from the fundamental study to application. This study fills the gap of research between the magnetic properties and sample preparation. We solve the complexity of magnetic anisotropy gradient induced. Eventually, a feasible in-memory computing unit has been achieved based on soft magnetic material.

7.2 Future work

For further research purposes, it is suggested that the following ideas could be considered.

Skyrmion based Y-shaped nanostructure logic unit

The topological structure skyrmion can be created and driven by current pulses and has already been studied[26, 27]. Reliable and feasible skyrmion based memory or logic devices will be the focus of future research. The Y-shaped skyrmion based logic unit has been investigated theoretically[168]. The simulation results proposed in their article proved the feasibility of new type skyrmion based logic gate including OR and AND gate. Based on our study of Y-shaped nanostructure and skyrmion generation in CoFeB ultrathin film, realizing spintronic logic unit based on the skyrmion in CoFeB material system is practicable. When width of the racetrack is less than $10\mu m$, the Hall effect of skyrmion can be eliminated[27]. Therefore, the design of Y-shaped device with width less than $10\mu m$ can trap skyrmion to the racetrack without annihilation. The Y-shaped nanostructure can achieve 2 in 1 logic gate by pushing the skyrmion within racetrack. In additional, 1 in 2 path selector based on Y-shaped device can be realized by adding

reverse different bias. The skyrmion can move up (down) by adding up (down) bias.

This skyrmion based logic gate, which has advantages of stability and low power consumption, can cascade with skyrmion racetrack memory to achieve the in-memory computing or neural network[27, 169]. Therefore, it is worth to study the skyrmion based Y-shaped nanostructure logic unit.

Cascade of Y-shaped nanostructure in-memory computing network

The direct external magnetic field input is not very suitable for cascading multiple logic gates. The current induced in-memory computing is closer to the practical applications. By fabricating the MTJ onto each arm of Y-shaped nanostructure, the current input and read out could be achieved avoid external magnetic field. The spin polarized current can be generated by the large write current crossing through MTJ and then inject into arm. The magnetization of arm can be reversed by spin polarized current and realize calculation functions. For the memory stage, a small read out current can detect the magnetization state through two MTJs integrated in the ‘Source’ and ‘Drain’ arms. By rotating 45 degrees of the Y-shaped nanostructure with each other and integral two of ‘Gate’ arm with one MTJs, the single Y-shaped nanostructure unit can be cascaded together and finally realized in-memory computing network. Expect the NiFe, many other magnetic materials, such as CoFeB, can be used to fabricate the in-memory computing which has advantages on stability and low power consumption.

List of Abbreviations

Integrated circuits	ICs
Complementary metal-oxide-semiconductor	CMOS
Giant magnetoresistance	GMR
Hard disk drive	HDD
Magnetic tunnel junctions	MTJs
Tunnel magnetoresistance	TMR
Static random-access memories	SRAM
Dynamic random-access memories	DRAM
Magnetoresistive Random Access Memory	MRAM
Spin-transfer torque	STT
Spin–orbit torque	SOT
Spin-transfer-torque magnetic random access memories	STT-MRAM
Thermal assistance	TAS
Heavy metal	HM
Ferromagnetic material	FM
Resistance switching RAM	RRAM
Phase change memory	PCM
Ferroelectric RAM	FeRAM
Domain-wall logic	DWL
Scanning transmission electron microscopy	STEM
First order reversal curves	FORC
Magneto-optical Kerr effect	MOKE
Perpendicular magnetic anisotropy	PMA
Transition metal	TM
Magnetoelectric RAM	MeRAM

Voltage control of magnetic anisotropy	VCMA
Domain wall	DW
Dzyaloshinskii–Moriya interaction	DMI
Spin–orbit coupling	SOC
Focused ion beam	FIB
Magnetic Transmission X-ray Microscopy	MTXM
Clockwise	CW
Anticlockwise	ACW
Vortex domain wall	VDW
Physical vapor deposition	PVD
Direct current	DC
Radio frequency	RF
Vibrating Sample Magnetometer	VSM
Scanning electron microscope	SEM
Time-resolved MOKE	TR-MOKE
Electron Beam Lithography	EBL
Transmission electron microscopy	TEM
Magnetic Force Microscopy	MFM
Atomic Force Microscopy	AFM
Density functional theory	DFT
Heat-assisted magnetic recording	HAMR
Spin-Seebeck effect	SSE
Arithmetic logic unit	ALU

References

[1] "Beyond CMOS," International Technology Roadmap for Semiconductors 2.0 (2015 ed.).

[2] M. N. Baibich *et al.*, "Giant magnetoresistance of (001)Fe/(001)Cr magnetic superlattices," *Phys Rev Lett,* vol. 61, no. 21, pp. 2472-2475, Nov 21 1988, doi: 10.1103/PhysRevLett.61.2472.

[3] T. Miyazaki and N. Tezuka, "Giant magnetic tunneling effect in Fe/Al2O3/Fe junction," *Journal of Magnetism and Magnetic Materials,* vol. 139, no. 3, pp. L231-L234, 1995, doi: 10.1016/0304-8853(95)90001-2.

[4] J. S. Moodera, L. R. Kinder, T. M. Wong, and R. Meservey, "Large magnetoresistance at room temperature in ferromagnetic thin film tunnel junctions," *Phys Rev Lett,* vol. 74, no. 16, pp. 3273-3276, Apr 17 1995, doi: 10.1103/PhysRevLett.74.3273.

[5] M. Julliere, "Tunneling between ferromagnetic films," *Physics Letters A,* vol. 54, no. 3, pp. 225-226, 1975, doi: 10.1016/0375-9601(75)90174-7.

[6] S. Maekawa and U. Gafvert, "Electron tunneling between ferromagnetic films," *IEEE Transactions on Magnetics,* vol. 18, no. 2, pp. 707-708, 1982, doi: 10.1109/tmag.1982.1061834.

[7] G. E. Moore, "Cramming more components onto integrated circuits, Reprinted from Electronics, volume 38, number 8, April 19, 1965, pp.114 ff," *IEEE Solid-State Circuits Society Newsletter,* vol. 11, no. 3, pp. 33-35, 2006, doi: 10.1109/n-ssc.2006.4785860.

[8] K. L. Wang, J. G. Alzate, and P. Khalili Amiri, "Low-power non-volatile spintronic memory: STT-RAM and beyond," *Journal of Physics D: Applied Physics,* vol. 46, no. 7, p. 074003, 2013, doi: 10.1088/0022-3727/46/7/074003.

[9] S. Assefa *et al.*, "Fabrication and characterization of MgO-based magnetic tunnel junctions for spin momentum transfer switching," *Journal of Applied Physics,* vol. 102, no. 6, p. 063901, 2007, doi: 10.1063/1.2781321.

[10] S. H. K. C.J. Lin, Y.J. Wang, K. Lee, X. Zhu, W.C. Chen, X. Li, W.N. Hsu,Y.C. Kao, M.T. Liu, W.C. Chen, YiChing Lin, M. Nowak, and N. Yu , Luan Tran, "45nm Low Power CMOS Logic Compatible Embedded STT MRAM Utilizing a Reverse-Connection 1T/1MTJ Cell," *IEEE International Electron Devices Meeting,* 2009, doi: 10.1109/IEDM.2009.5424368.

[11] Y. Huai, F. Albert, P. Nguyen, M. Pakala, and T. Valet, "Observation of spin-transfer switching in deep submicron-sized and low-resistance magnetic tunnel junctions," *Applied Physics Letters,* vol. 84, no. 16, pp. 3118-3120, 2004, doi: 10.1063/1.1707228.

[12] E. Chen *et al.*, "Advances and Future Prospects of Spin-Transfer Torque Random Access Memory," *IEEE Transactions on Magnetics,* vol. 46, no. 6, pp. 1873-1878, 2010, doi: 10.1109/tmag.2010.2042041.

[13] J. A. Katine, F. J. Albert, R. A. Buhrman, E. B. Myers, and D. C. Ralph, "Current-driven magnetization reversal and spin-wave excitations in Co /Cu /Co pillars," *Phys Rev Lett,* vol. 84, no. 14, pp. 3149-52, Apr 3 2000, doi: 10.1103/PhysRevLett.84.3149.

[14] S. S. Parkin *et al.*, "Giant tunnelling magnetoresistance at room temperature with MgO (100) tunnel barriers," *Nat Mater,* vol. 3, no. 12, pp. 862-7, Dec 2004, doi: 10.1038/nmat1256.

[15] J. I. Raffel and T. S. Crowther, "A Proposal for an Associative Memory Using Magnetic Films," *IEEE Transactions on Electronic Computers,* vol. EC-13, no. 5, pp. 611-611, 1964, doi: 10.1109/pgec.1964.263736.

[16] S. Ikeda *et al.*, "A perpendicular-anisotropy CoFeB-MgO magnetic tunnel junction," *Nat Mater,*

vol. 9, no. 9, pp. 721-4, Sep 2010, doi: 10.1038/nmat2804.

[17] R. L. Stamps *et al.*, "The 2014 Magnetism Roadmap," (in English), *J Phys D Appl Phys,* vol. 47, no. 33, Aug 20 2014, doi: Artn 333001
10.1088/0022-3727/47/33/333001.

[18] O. R. Bernard Dieny, "Magnetic tunnel junction, magnetic device, memory and writing and reading methods using said devices," Patent US 6,950,335 B2 Patent Appl. 10/495,637, 2001.

[19] I. L. Prejbeanu *et al.*, "Thermally assisted MRAM," *Journal of Physics: Condensed Matter,* vol. 19, no. 16, p. 165218, 2007, doi: 10.1088/0953-8984/19/16/165218.

[20] K. Lee and S. H. Kang, "Development of Embedded STT-MRAM for Mobile System-on-Chips," *IEEE Transactions on Magnetics,* vol. 47, no. 1, pp. 131-136, 2011, doi: 10.1109/tmag.2010.2075920.

[21] J. Sinova, S. O. Valenzuela, J. Wunderlich, C. H. Back, and T. Jungwirth, "Spin Hall effects," *Rev Mod Phys,* vol. 87, no. 4, pp. 1213-1260, 2015, doi: 10.1103/RevModPhys.87.1213.

[22] G. Prenat *et al.*, "Ultra-Fast and High-Reliability SOT-MRAM: From Cache Replacement to Normally-Off Computing," *IEEE Transactions on Multi-Scale Computing Systems,* vol. 2, no. 1, pp. 49-60, 2016, doi: 10.1109/tmscs.2015.2509963.

[23] S. Heinze *et al.*, "Spontaneous atomic-scale magnetic skyrmion lattice in two dimensions," *Nature Physics,* vol. 7, no. 9, pp. 713-718, 2011, doi: 10.1038/nphys2045.

[24] G. Chen, A. Mascaraque, A. T. N'Diaye, and A. K. Schmid, "Room temperature skyrmion ground state stabilized through interlayer exchange coupling," *Applied Physics Letters,* vol. 106, no. 24, 2015, doi: 10.1063/1.4922726.

[25] B. Schulz and K. Baberschke, "Crossover from in-plane to perpendicular magnetization in ultrathin Ni/Cu(001) films," *Physical Review B,* vol. 50, no. 18, pp. 13467-13471, 1994, doi: 10.1103/PhysRevB.50.13467.

[26] W. Jiang *et al.*, "Magnetism. Blowing magnetic skyrmion bubbles," *Science,* vol. 349, no. 6245, pp. 283-6, Jul 17 2015, doi: 10.1126/science.aaa1442.

[27] G. Yu *et al.*, "Room-Temperature Skyrmion Shift Device for Memory Application," *Nano Lett,* vol. 17, no. 1, pp. 261-268, Jan 11 2017, doi: 10.1021/acs.nanolett.6b04010.

[28] D. Ielmini and H. S. P. Wong, "In-memory computing with resistive switching devices," *Nature Electronics,* vol. 1, no. 6, pp. 333-343, 2018, doi: 10.1038/s41928-018-0092-2.

[29] M. Di Ventra and Y. V. Pershin, "The parallel approach," *Nature Physics,* vol. 9, no. 4, pp. 200-202, 2013, doi: 10.1038/nphys2566.

[30] G. Indiveri and S.-C. Liu, "Memory and Information Processing in Neuromorphic Systems," *Proceedings of the IEEE,* vol. 103, no. 8, pp. 1379-1397, 2015, doi: 10.1109/jproc.2015.2444094.

[31] R. Waser and M. Aono, "Nanoionics-based resistive switching memories," *Nat Mater,* vol. 6, no. 11, pp. 833-40, Nov 2007, doi: 10.1038/nmat2023.

[32] S. Raoux, W. Welnic, and D. Ielmini, "Phase change materials and their application to nonvolatile memories," *Chem Rev,* vol. 110, no. 1, pp. 240-67, Jan 2010, doi: 10.1021/cr900040x.

[33] A. D. Kent and D. C. Worledge, "A new spin on magnetic memories," *Nat Nanotechnol,* vol. 10, no. 3, pp. 187-91, Mar 2015, doi: 10.1038/nnano.2015.24.

[34] T. Mikolajick *et al.*, "FeRAM technology for high density applications," (in English), *Microelectron Reliab,* vol. 41, no. 7, pp. 947-950, Jul 2001, doi: Doi 10.1016/S0026-2714(01)00049-X.

[35] H. S. Wong and S. Salahuddin, "Memory leads the way to better computing," *Nat Nanotechnol,* vol. 10, no. 3, pp. 191-4, Mar 2015, doi: 10.1038/nnano.2015.29.

[36] E. Linn, R. Rosezin, S. Tappertzhofen, U. Bottger, and R. Waser, "Beyond von Neumann--logic operations in passive crossbar arrays alongside memory operations," *Nanotechnology,* vol. 23, no. 30, p. 305205, Aug 3 2012, doi: 10.1088/0957-4484/23/30/305205.

[37] M. T. Niemier *et al.*, "Nanomagnet logic: progress toward system-level integration," *J Phys Condens Matter,* vol. 23, no. 49, p. 493202, Dec 14 2011, doi: 10.1088/0953-8984/23/49/493202.

[38] R. P. Cowburn and M. E. Welland, "Room temperature magnetic quantum cellular automata," *Science,* vol. 287, no. 5457, pp. 1466-8, Feb 25 2000. [Online]. Available: https://www.ncbi.nlm.nih.gov/pubmed/10688790.

[39] A. Imre, G. Csaba, L. Ji, A. Orlov, G. H. Bernstein, and W. Porod, "Majority logic gate for magnetic quantum-dot cellular automata," *Science,* vol. 311, no. 5758, pp. 205-8, Jan 13 2006, doi: 10.1126/science.1120506.

[40] M. Gavagnin, H. D. Wanzenboeck, D. Belic, and E. Bertagnolli, "Synthesis of individually tuned nanomagnets for Nanomagnet Logic by direct write focused electron beam induced deposition," *ACS Nano,* vol. 7, no. 1, pp. 777-84, Jan 22 2013, doi: 10.1021/nn305079a.

[41] S. H. Jo, K. H. Kim, and W. Lu, "High-density crossbar arrays based on a Si memristive system," *Nano Lett,* vol. 9, no. 2, pp. 870-4, Feb 2009, doi: 10.1021/nl8037689.

[42] D. Kau *et al.*, "A stackable cross point phase change memory," (in English), *Int El Devices Meet,* pp. 617-20, 2009. [Online]. Available: <Go to ISI>://WOS:000279343900148.

[43] D. A. Allwood, "Submicrometer Ferromagnetic NOT Gate and Shift Register," *Science,* pp. 2003-6, 2002.

[44] D. Atkinson, D. A. Allwood, G. Xiong, M. D. Cooke, C. C. Faulkner, and R. P. Cowburn, "Magnetic domain-wall dynamics in a submicrometre ferromagnetic structure," *Nat Mater,* vol. 2, no. 2, pp. 85-7, Feb 2003, doi: 10.1038/nmat803.

[45] T. Hesjedal and T. Phung, "Magnetic logic element based on an S-shaped Permalloy structure," *Applied Physics Letters,* vol. 96, no. 7, pp. 072501-1-3, 2010, doi: 10.1063/1.3314301.

[46] K. A. Omari *et al.*, "Toward Chirality‐Encoded Domain Wall Logic," *Advanced Functional Materials,* vol. 29, no. 10, pp. 1807282-1-9, 2019, doi: 10.1002/adfm.201807282.

[47] C. D. G. B. D. CULLITY, *Introduction to magnetic materials*. John Wiley & Sons, 2011.

[48] J. A. C. B. B. Heinrich, *Ultrathin Magnetic Structures I & II* (Springer Science & Business Media). 2006.

[49] S. Woo *et al.*, "Observation of room-temperature magnetic skyrmions and their current-driven dynamics in ultrathin metallic ferromagnets," *Nat Mater,* vol. 15, no. 5, pp. 501-6, May 2016, doi: 10.1038/nmat4593.

[50] Q. Yang *et al.*, "Voltage Control of Skyrmion Bubbles for Topological Flexible Spintronic Devices," *Advanced Electronic Materials,* vol. 6, no. 8, 2020, doi: 10.1002/aelm.202000246.

[51] R. Schafer, "Investigation of Domains and Dynamics of Domain Walls by the Magneto-optical Kerr-effect," Handbook of magnetism and advanced magnetic materials, 2007.

[52] S. Monso *et al.*, "Crossover from in-plane to perpendicular anisotropy in Pt/CoFe/AlOx sandwiches as a function of Al oxidation: A very accurate control of the oxidation of tunnel barriers," *Applied Physics Letters,* vol. 80, no. 22, pp. 4157-4159, 2002, doi: 10.1063/1.1483122.

[53] G. H. O. Daalderop, P. J. Kelly, and M. F. H. Schuurmans, "Magnetocrystalline anisotropy and

orbital moments in transition-metal compounds," *Physical Review B,* vol. 44, no. 21, pp. 12054-12057, 1991, doi: 10.1103/PhysRevB.44.12054.

[54] D. C. Worledge, "Seed layer and free magnetic layer for perpindicular anisotropy in a spin-torque magnetic random access memory," Patent US 8,536,668 B2 Patent Appl. 13/570,375, 2013.

[55] D. C. Worledge, G. Hu, D. W. Abraham, P. L. Trouilloud, and S. Brown, "Development of perpendicularly magnetized Ta|CoFeB|MgO-based tunnel junctions at IBM (invited)," *Journal of Applied Physics,* vol. 115, no. 17, 2014, doi: 10.1063/1.4870169.

[56] R. Wiesendanger, "Nanoscale magnetic skyrmions in metallic films and multilayers: a new twist for spintronics," *Nature Reviews Materials,* vol. 1, no. 7, 2016, doi: 10.1038/natrevmats.2016.44.

[57] W. Kang, Y. Huang, X. Zhang, Y. Zhou, and W. Zhao, "Skyrmion-Electronics: An Overview and Outlook," *Proceedings of the IEEE,* vol. 104, no. 10, pp. 2040-2061, 2016, doi: 10.1109/jproc.2016.2591578.

[58] Bogdanov, "Thermodynamically stable "vortices" in magnetically ordered crystals. The mixed state of magnets," *Sov. Phys. JETP,* vol. 66, pp. 178-182, 1989.

[59] A. Bogdanov and A. Hubert, "Thermodynamically Stable Magnetic Vortex States in Magnetic Crystals," (in English), *Journal of Magnetism and Magnetic Materials,* vol. 138, no. 3, pp. 255-269, Dec 1994, doi: Doi 10.1016/0304-8853(94)90046-9.

[60] G. Yu *et al.*, "Room-Temperature Creation and Spin-Orbit Torque Manipulation of Skyrmions in Thin Films with Engineered Asymmetry," *Nano Lett,* vol. 16, no. 3, pp. 1981-8, Mar 9 2016, doi: 10.1021/acs.nanolett.5b05257.

[61] W. C. Tsai *et al.*, "Investigation of perpendicular magnetic anisotropy of CoFeB by x-ray magnetic circular dichroism," *Applied Physics Letters,* vol. 100, no. 17, 2012, doi: 10.1063/1.4707380.

[62] Y.-W. Oh, K.-D. Lee, J.-R. Jeong, and B.-G. Park, "Interfacial perpendicular magnetic anisotropy in CoFeB/MgO structure with various underlayers," *Journal of Applied Physics,* vol. 115, no. 17, 2014, doi: 10.1063/1.4864047.

[63] H. X. Yang, M. Chshiev, B. Dieny, J. H. Lee, A. Manchon, and K. H. Shin, "First-principles investigation of the very large perpendicular magnetic anisotropy at Fe|MgO and Co|MgO interfaces," *Physical Review B,* vol. 84, no. 5, 2011, doi: 10.1103/PhysRevB.84.054401.

[64] S. Yakata *et al.*, "Influence of perpendicular magnetic anisotropy on spin-transfer switching current in CoFeB ⁄ MgO ⁄ CoFeB magnetic tunnel junctions," *Journal of Applied Physics,* vol. 105, no. 7, 2009, doi: 10.1063/1.3057974.

[65] T. Liu, J. W. Cai, and L. Sun, "Large enhanced perpendicular magnetic anisotropy in CoFeB/MgO system with the typical Ta buffer replaced by an Hf layer," *AIP Advances,* vol. 2, no. 3, p. 032151, 2012, doi: 10.1063/1.4748337.

[66] T. Liu, Y. Zhang, J. W. Cai, and H. Y. Pan, "Thermally robust Mo/CoFeB/MgO trilayers with strong perpendicular magnetic anisotropy," *Sci Rep,* vol. 4, p. 5895, Jul 31 2014, doi: 10.1038/srep05895.

[67] S. Yang, J. Lee, G. An, J. Kim, W. Chung, and J. Hong, "Thermally stable perpendicular magnetic anisotropy features of Ta/TaOx/Ta/CoFeB/MgO/W stacks via TaOx underlayer insertion," *Journal of Applied Physics,* vol. 116, no. 11, p. 113902, 2014, doi: 10.1063/1.4895709.

[68] A. Natarajarathinam, Z. R. Tadisina, T. Mewes, S. Watts, E. Chen, and S. Gupta, "Influence of

capping layers on CoFeB anisotropy and damping," *Journal of Applied Physics,* vol. 112, no. 5, p. 053909, 2012, doi: 10.1063/1.4749412.

[69] H. Kubota *et al.*, "Enhancement of perpendicular magnetic anisotropy in FeB free layers using a thin MgO cap layer," *Journal of Applied Physics,* vol. 111, no. 7, p. 07C723, 2012, doi: 10.1063/1.3679393.

[70] C. Scheck, L. Cheng, I. Barsukov, Z. Frait, and W. E. Bailey, "Low relaxation rate in epitaxial vanadium-doped ultrathin iron films," *Phys Rev Lett,* vol. 98, no. 11, p. 117601, Mar 16 2007, doi: 10.1103/PhysRevLett.98.117601.

[71] S. Ikeda *et al.*, "Magnetic Tunnel Junctions for Spintronic Memories and Beyond," *IEEE Transactions on Electron Devices,* vol. 54, no. 5, pp. 991-1002, 2007, doi: 10.1109/ted.2007.894617.

[72] J. C. Slonczewski, "Current-driven excitation of magnetic multilayers," *Journal of Magnetism and Magnetic Materials,* vol. 159, no. 1-2, pp. L1-L7, 1996, doi: 10.1016/0304-8853(96)00062-5.

[73] L. Berger, "Emission of spin waves by a magnetic multilayer traversed by a current," *Phys Rev B Condens Matter,* vol. 54, no. 13, pp. 9353-9358, Oct 1 1996. [Online]. Available: https://www.ncbi.nlm.nih.gov/pubmed/9984672.

[74] Y. Takeuchi, H. Sato, S. Fukami, F. Matsukura, and H. Ohno, "Temperature dependence of energy barrier in CoFeB-MgO magnetic tunnel junctions with perpendicular easy axis," *Applied Physics Letters,* vol. 107, no. 15, 2015, doi: 10.1063/1.4933256.

[75] H. Sato, P. Chureemart, F. Matsukura, R. W. Chantrell, H. Ohno, and R. F. L. Evans, "Temperature-dependent properties of CoFeB/MgO thin films: Experiments versus simulations," *Physical Review B,* vol. 98, no. 21, 2018, doi: 10.1103/PhysRevB.98.214428.

[76] T. Rausch, E. Gage, and J. Dykes, "Heat Assisted Magnetic Recording," in *Ultrafast Magnetism I*, vol. 159, (Springer Proceedings in Physics: Springer, Cham, 2015, ch. Chapter 63, pp. 200-202.

[77] R. E. Rottmayer *et al.*, "Heat-Assisted Magnetic Recording," *IEEE Transactions on Magnetics,* vol. 42, no. 10, pp. 2417-2421, 2006, doi: 10.1109/tmag.2006.879572.

[78] G. Ju *et al.*, "High Density Heat-Assisted Magnetic Recording Media and Advanced Characterization—Progress and Challenges," *IEEE Transactions on Magnetics,* vol. 51, no. 11, pp. 1-9, 2015, doi: 10.1109/tmag.2015.2439690.

[79] G. E. Bauer, E. Saitoh, and B. J. van Wees, "Spin caloritronics," *Nat Mater,* vol. 11, no. 5, pp. 391-9, Apr 23 2012, doi: 10.1038/nmat3301.

[80] A. D. Avery, M. R. Pufall, and B. L. Zink, "Determining the planar Nernst effect from magnetic-field-dependent thermopower and resistance in nickel and permalloy thin films," *Physical Review B,* vol. 86, no. 18, 2012, doi: 10.1103/PhysRevB.86.184408.

[81] T. Böhnert, V. Vega, A.-K. Michel, V. M. Prida, and K. Nielsch, "Magneto-thermopower and magnetoresistance of single Co-Ni alloy nanowires," *Applied Physics Letters,* vol. 103, no. 9, 2013, doi: 10.1063/1.4819949.

[82] S. S. P. P. b. Jing Shi a, L. Xing a and M.B. Salamon a, "Giant magnetoresistance and magnetothermopower in Co/Cu multilayers," *J. Magn. Magn. Mater.,* vol. 125, pp. 251-6, 1993.

[83] T. Böhnert *et al.*, "Magnetothermopower and magnetoresistance of single Co-Ni/Cu multilayered nanowires," *Physical Review B,* vol. 90, no. 16, 2014, doi: 10.1103/PhysRevB.90.165416.

[84] S. Yuasa, T. Nagahama, A. Fukushima, Y. Suzuki, and K. Ando, "Giant room-temperature

magnetoresistance in single-crystal Fe/MgO/Fe magnetic tunnel junctions," *Nat Mater,* vol. 3, no. 12, pp. 868-71, Dec 2004, doi: 10.1038/nmat1257.

[85] T. Bohnert, S. Serrano-Guisan, E. Paz, B. Lacoste, R. Ferreira, and P. P. Freitas, "Magnetic tunnel junctions with integrated thermometers for magnetothermopower measurements," *J Phys Condens Matter,* vol. 29, no. 18, p. 185303, May 10 2017, doi: 10.1088/1361-648X/aa63ab.

[86] K. Uchida *et al.*, "Observation of the spin Seebeck effect," *Nature,* vol. 455, no. 7214, pp. 778-81, Oct 9 2008, doi: 10.1038/nature07321.

[87] D. Meier *et al.*, "Longitudinal spin Seebeck effect contribution in transverse spin Seebeck effect experiments in Pt/YIG and Pt/NFO," *Nat Commun,* vol. 6, p. 8211, Sep 23 2015, doi: 10.1038/ncomms9211.

[88] Z. Wang *et al.*, "Thermal generation, manipulation and thermoelectric detection of skyrmions," *Nature Electronics,* vol. 3, no. 11, pp. 672-679, 2020, doi: 10.1038/s41928-020-00489-2.

[89] L. You *et al.*, "Switching of perpendicularly polarized nanomagnets with spin orbit torque without an external magnetic field by engineering a tilted anisotropy," *Proc Natl Acad Sci U S A,* vol. 112, no. 33, pp. 10310-5, Aug 18 2015, doi: 10.1073/pnas.1507474112.

[90] T. Schulz *et al.*, "Emergent electrodynamics of skyrmions in a chiral magnet," *Nat Phys,* vol. 8, p. 301, 02/19/online 2012, doi: 10.1038/nphys2231
https://www.nature.com/articles/nphys2231#supplementary-information.

[91] W. J. Jiang *et al.*, "Direct observation of the skyrmion Hall effect," *Nat Phys,* vol. 13, no. 2, pp. 162-169, Feb 2017, doi: 10.1038/nphys3883.

[92] K. Litzius *et al.*, "Skyrmion Hall effect revealed by direct time-resolved X-ray microscopy," *Nat Phys,* vol. 13, no. 2, pp. 170-175, Feb 2017, doi: 10.1038/nphys4000.

[93] S. Mühlbauer *et al.*, "Skyrmion Lattice in a Chiral Magnet," *Science,* vol. 323, no. 5916, pp. 915-919, 2009, doi: 10.1126/science.1166767.

[94] A. Neubauer *et al.*, "Topological Hall effect in the *A* phase of MnSi," *Phys Rev Lett,* vol. 102, no. 18, p. 186602, 05/04/ 2009, doi: 10.1103/PhysRevLett.102.186602.

[95] C. Pappas *et al.*, "Chiral paramagnetic skyrmion-like phase in MnSi," *Phys Rev Lett,* vol. 102, no. 19, p. 197202, 05/15/ 2009, doi: 10.1103/PhysRevLett.102.197202.

[96] X. Z. Yu *et al.*, "Real-space observation of a two-dimensional skyrmion crystal," *Nature,* vol. 465, no. 7300, pp. 901-904, Jun 2010, doi: 10.1038/nature09124.

[97] N. Nagaosa and Y. Tokura, "Topological properties and dynamics of magnetic skyrmions," *Nat Nanotechnol,* Review Article vol. 8, p. 899, 2013, doi: 10.1038/nnano.2013.243.

[98] C. Moreau Luchaire *et al.*, "Additive interfacial chiral interaction in multilayers for stabilization of small individual skyrmions at room temperature," *Nat Nanotechnol,* Article vol. 11, no. 5, pp. 444-448, 2016, doi: 10.1038/nnano.2015.313
http://www.nature.com/nnano/journal/v11/n5/abs/nnano.2015.313.html#supplementary-information.

[99] W. J. Jiang *et al.*, "Blowing magnetic skyrmion bubbles," *Science,* vol. 349, no. 6245, pp. 283-286, Jul 2015, doi: 10.1126/science.aaa1442.

[100] S. Woo *et al.*, "Observation of room-temperature magnetic skyrmions and their current-driven dynamics in ultrathin metallic ferromagnets," *Nat Mater,* Letter vol. 15, no. 5, pp. 501-506, 2016, doi: 10.1038/nmat4593
http://www.nature.com/nmat/journal/v15/n5/abs/nmat4593.html#supplementary-information.

[101] O. Boulle *et al.*, "Room-temperature chiral magnetic skyrmions in ultrathin magnetic

nanostructures," *Nat Nanotechnol,* Article vol. 11, no. 5, pp. 449-454, 2016, doi: 10.1038/nnano.2015.315
http://www.nature.com/nnano/journal/v11/n5/abs/nnano.2015.315.html#supplementary-information.

[102] L. Zhou *et al.*, "Strength and directionality of surface Ruderman–Kittel–Kasuya–Yosida interaction mapped on the atomic scale," *Nature Physics,* vol. 6, no. 3, pp. 187-191, 2010, doi: 10.1038/nphys1514.

[103] I. Kezsmarki *et al.*, "Neel-type skyrmion lattice with confined orientation in the polar magnetic semiconductor GaV4S8," *Nat Mater,* vol. 14, no. 11, pp. 1116-22, Nov 2015, doi: 10.1038/nmat4402.

[104] G. Q. Yu *et al.*, "Room-Temperature Skyrmion Shift Device for Memory Application," *Nano Lett,* vol. 17, no. 1, pp. 261-268, Jan 2017, doi: 10.1021/acs.nanolett.6b04010.

[105] F. Büttner *et al.*, "Field-free deterministic ultrafast creation of magnetic skyrmions by spin–orbit torques," *Nat Nanotechnol,* vol. 12, no. 11, pp. 1040-1044, 2017/11/01 2017, doi: 10.1038/nnano.2017.178.

[106] J. Zazvorka *et al.*, "Thermal skyrmion diffusion used in a reshuffler device," *Nat Nanotechnol,* Apr 22 2019, doi: 10.1038/s41565-019-0436-8.

[107] N. Romming *et al.*, "Writing and deleting single magnetic skyrmions," *Science,* vol. 341, no. 6146, pp. 636-9, Aug 9 2013, doi: 10.1126/science.1240573.

[108] K. Fallon *et al.*, "Controlled Individual Skyrmion Nucleation at Artificial Defects Formed by Ion Irradiation," *Small,* vol. 16, no. 13, p. e1907450, Apr 2020, doi: 10.1002/smll.201907450.

[109] R. Juge *et al.*, "Helium Ions Put Magnetic Skyrmions on the Track," *Nano Lett,* vol. 21, no. 7, pp. 2989-2996, Apr 14 2021, doi: 10.1021/acs.nanolett.1c00136.

[110] I. Lima Fernandes, J. Bouaziz, S. Blügel, and S. Lounis, "Universality of defect-skyrmion interaction profiles," *Nature Communications,* vol. 9, no. 1, 2018, doi: 10.1038/s41467-018-06827-5.

[111] G. Yu *et al.*, "Room-Temperature Creation and Spin–Orbit Torque Manipulation of Skyrmions in Thin Films with Engineered Asymmetry," *Nano Lett,* vol. 16, no. 3, pp. 1981-1988, 2016/03/09 2016, doi: 10.1021/acs.nanolett.5b05257.

[112] H. Soon Park *et al.*, "Observation of the magnetic flux and three-dimensional structure of skyrmion lattices by electron holography," *Nat Nanotechnol,* vol. 9, no. 5, pp. 337-342, May 2014. [Online]. Available: <Go to ISI>://WOS:000336235800008.

[113] A. Soumyanarayanan *et al.*, "Tunable room-temperature magnetic skyrmions in Ir/Fe/Co/Pt multilayers," *Nat Mater,* Article vol. 16, p. 898, 07/17/online 2017, doi: 10.1038/nmat4934
https://www.nature.com/articles/nmat4934#supplementary-information.

[114] W. Legrand *et al.*, "Room-Temperature Current-Induced Generation and Motion of sub-100 nm Skyrmions," *Nano Lett,* vol. 17, no. 4, pp. 2703-2712, 2017/04/12 2017, doi: 10.1021/acs.nanolett.7b00649.

[115] R. Juge *et al.*, "Helium Ions Put Magnetic Skyrmions on the Track," *Nano Lett,* vol. 21, no. 7, pp. 2989-2996, 2021/04/14 2021, doi: 10.1021/acs.nanolett.1c00136.

[116] K. A. Omari, "Toward Chirality-Encoded Domain Wall Logic," *advanced Functional Materials,* 2019, doi: 10.1002/adfm.201807282.

[117] A. Hirohata, C. C. Yao, H. T. Leung, Y. B. Xu, C. M. Guertler, and J. A. C. Bland, "Magnetic domain studies of permalloy wire-based structures with junctions," *IEEE Transactions on Magnetics,*

vol. 36, no. 5, pp. 3068-3070, 2000, doi: 10.1109/20.908682.

[118] D. A. Allwood *et al.*, "Submicrometer ferromagnetic NOT gate and shift register," *Science,* vol. 296, no. 5575, pp. 2003-6, Jun 14 2002, doi: 10.1126/science.1070595.

[119] S. Lepadatu and Y. B. Xu, "Direct observation of domain wall scattering in patterned Ni80Fe20 and Ni nanowires by current-voltage measurements," *Phys Rev Lett,* vol. 92, no. 12, p. 127201, Mar 26 2004, doi: 10.1103/PhysRevLett.92.127201.

[120] M. Hayashi, L. Thomas, C. Rettner, R. Moriya, X. Jiang, and S. S. Parkin, "Dependence of current and field driven depinning of domain walls on their structure and chirality in permalloy nanowires," *Phys Rev Lett,* vol. 97, no. 20, p. 207205, Nov 17 2006, doi: 10.1103/PhysRevLett.97.207205.

[121] T. Ono, H. Miyajima, K. Shigeto, K. Mibu, N. Hosoito, and T. Shinjo, "Propagation of a magnetic domain wall in a submicrometer magnetic wire," (in English), *Science,* vol. 284, no. 5413, pp. 468-470, Apr 16 1999, doi: DOI 10.1126/science.284.5413.468.

[122] P. Xu, K. Xia, C. Gu, L. Tang, H. Yang, and J. Li, "An all-metallic logic gate based on current-driven domain wall motion," *Nat Nanotechnol,* vol. 3, no. 2, pp. 97-100, Feb 2008, doi: 10.1038/nnano.2008.1.

[123] D. A. Allwood, G. Xiong, C. C. Faulkner, D. Atkinson, D. Petit, and R. P. Cowburn, "Magnetic domain-wall logic," (in English), *Science,* vol. 309, no. 5741, pp. 1688-1692, Sep 9 2005, doi: 10.1126/science.1108813.

[124] P. Chapon. *GDOES, the analytical companion tool for magnetron sputtering deposition*. HORIBA Scientific.

[125] S. Foner, "Versatile and Sensitive Vibrating‐Sample Magnetometer," *Review of Scientific Instruments,* vol. 30, no. 7, pp. 548-557, 1959, doi: 10.1063/1.1716679.

[126] Wikipedia. "Transmission Electron Microscopy." https://en.wikipedia.org/wiki/Transmission_electron_microscopy. (accessed.

[127] S. R. Yadhuraj, G. Satheesh Babu, and M. Uttara Kumari, "Measurement of thickness and roughness using gwyddion," presented at the 2016 3rd International Conference on Advanced Computing and Communication Systems (ICACCS), 2016.

[128] J. Zázvorka *et al.*, "Thermal skyrmion diffusion used in a reshuffler device," *Nat Nanotechnol,* vol. 14, pp. 658–661, 2019/04/22 2019, doi: 10.1038/s41565-019-0436-8.

[129] J. D. Burton, S. S. Jaswal, E. Y. Tsymbal, O. N. Mryasov, and O. G. Heinonen, "Atomic and electronic structure of the CoFeB / MgO interface from first principles," *Appl Phys Lett,* vol. 89, no. 14, p. 142507, 2006, doi: 10.1063/1.2360189.

[130] K. Y. Yu *et al.*, "Removal of stacking-fault tetrahedra by twin boundaries in nanotwinned metals," *Nat Commun,* Article vol. 4, p. 1377, 01/22/online 2013, doi: 10.1038/ncomms2382 https://www.nature.com/articles/ncomms2382#supplementary-information.

[131] A. Casiraghi *et al.*, "Individual skyrmion manipulation by local magnetic field gradients," *Communications Physics,* vol. 2, no. 1, p. 145, 2019/11/15 2019, doi: 10.1038/s42005-019-0242-5.

[132] H. J. Hug *et al.*, "Quantitative magnetic force microscopy on perpendicularly magnetized samples," *J Appl Phys,* vol. 83, no. 11, pp. 5609-5620, 1998, doi: 10.1063/1.367412.

[133] A. Vansteenkiste, J. Leliaert, M. Dvornik, M. Helsen, F. Garcia-Sanchez, and B. Van Waeyenberge, "The design and verification of MuMax3," *AIP Advances,* vol. 4, no. 10, pp. 107133-1-22, 2014, doi: 10.1063/1.4899186.

[134] S. Ikeda *et al.*, "A perpendicular-anisotropy CoFeB–MgO magnetic tunnel junction," *Nat Mater,* vol. 9, p. 721, 07/11/online 2010, doi: 10.1038/nmat2804.

[135] S. V. Karthik, Y. K. Takahashi, T. Ohkubo, K. Hono, S. Ikeda, and H. Ohno, "Transmission electron microscopy investigation of CoFeB/MgO/CoFeB pseudospin valves annealed at different temperatures," *J Appl Phys,* vol. 106, no. 2, p. 023920, 2009, doi: 10.1063/1.3182817.

[136] R. F. L. Evans, W. J. Fan, P. Chureemart, T. A. Ostler, M. O. A. Ellis, and R. W. Chantrell, "Atomistic spin model simulations of magnetic nanomaterials," *J Phys: Condens. Matter.,* vol. 26, no. 10, p. 103202, 2014/02/19 2014, doi: 10.1088/0953-8984/26/10/103202.

[137] R. Shimabukuro, K. Nakamura, T. Akiyama, and T. Ito, "Electric field effects on magnetocrystalline anisotropy in ferromagnetic Fe monolayers," *Physica E: Low-dimensional Systems and Nanostructures,* vol. 42, no. 4, pp. 1014-1017, 2010, doi: 10.1016/j.physe.2009.11.110.

[138] I. Turek, S. Blügel, G. Bihlmayer, and P. Weinberger, "Exchange Interactions at Surfaces of Fe, Co, and Gd," *Czech J Phys,* journal article vol. 53, no. 1, pp. 81-88, January 01 2003, doi: 10.1023/a:1022363806047.

[139] H. Yang, M. Chshiev, B. Dieny, J. Lee, A. Manchon, and K. Shin, "First-principles investigation of the very large Perpendicular Magnetic Anisotropy at Fe|MgO Interfaces," *Phys Rev B,* vol. 84, p. 054401, 08/01 2011, doi: 10.1103/PhysRevB.84.054401.

[140] H. Sato, P. Chureemart, F. Matsukura, R. Chantrell, H. Ohno, and R. Evans, "Temperature-dependent properties of CoFeB/MgO thin films: Experiments versus simulations," *Phys Rev B,* vol. 98, p. 214428, 12/14 2018, doi: 10.1103/PhysRevB.98.214428.

[141] P. Asselin *et al.*, "Constrained Monte Carlo method and calculation of the temperature dependence of magnetic anisotropy," *Phys Rev B,* vol. 82, no. 5, p. 054415, 08/11/ 2010, doi: 10.1103/PhysRevB.82.054415.

[142] R. F. L. Evans, U. Atxitia, and R. W. Chantrell, "Quantitative simulation of temperature-dependent magnetization dynamics and equilibrium properties of elemental ferromagnets," *Phys Rev B,* vol. 91, no. 14, p. 144425, 04/30/ 2015, doi: 10.1103/PhysRevB.91.144425.

[143] C. Moreau Luchaire *et al.*, "Additive interfacial chiral interaction in multilayers for stabilization of small individual skyrmions at room temperature," *Nat Nanotechnol,* Article vol. 11, no. 5, pp. 444-448, 2016, doi: 10.1038/nnano.2015.313

http://www.nature.com/nnano/journal/v11/n5/abs/nnano.2015.313.html#supplementary-information.

[144] J. E. Davies, O. Hellwig, E. E. Fullerton, G. Denbeaux, J. B. Kortright, and K. Liu, "Magnetization reversal of Co/Pt multilayers: Microscopic origin of high-field magnetic irreversibility," (in English), *Phys Rev B,* Article vol. 70, no. 22, p. 8, Dec 2004, Art no. 224434, doi: 10.1103/PhysRevB.70.224434.

[145] R. Morgunov *et al.*, "Magnetic aftereffects in CoFeB/Ta/CoFeB spin valves of large area," *Physical Review B,* vol. 96, no. 5, 2017, doi: 10.1103/PhysRevB.96.054421.

[146] J. L. C. B. Fuentes, N. Bochud, A. M. Gomez and A. M. Peinado, "Model-based cepstral analysis for ultrasonic non-destructive evaluation of composites," presented at the 2012 IEEE International Conference on Acoustics, Speech and Signal Processing (ICASSP), 2012.

[147] G. Y. T. A Sophian, D Taylor and J Rudlin, "Electromagnetic and eddy current NDT: a review," *ELECTROMAGNETIC NDT,* vol. 43, pp. 302-306, 2001.

[148] J. Liu, G. Y. Tian, B. Gao, W. Ren, and J. S. Meng, "Investigation of thermal imaging sampling

frequency for eddy current pulsed thermography," *NDT & E International,* vol. 62, pp. 85-92, 2014, doi: 10.1016/j.ndteint.2013.11.009.

[149] M. C. Teague, T. Rodgers, S. Grutzik, and S. Meserole, "Characterization and modeling of microstructural stresses in alumina," *Journal of the American Ceramic Society,* vol. 101, no. 5, pp. 2155-2161, 2018, doi: 10.1111/jace.15369.

[150] *Microstat-family-of-cryostats*. Oxford Instruments.

[151] A. Vindigni, N. Saratz, O. Portmann, D. Pescia, and P. Politi, "Stripe width and nonlocal domain walls in the two-dimensional dipolar frustrated Ising ferromagnet," *Physical Review B,* vol. 77, no. 9, 2008, doi: 10.1103/PhysRevB.77.092414.

[152] O. Portmann, A. Vaterlaus, and D. Pescia, "Observation of stripe mobility in a dipolar frustrated ferromagnet," *Phys Rev Lett,* vol. 96, no. 4, p. 047212, Feb 3 2006, doi: 10.1103/PhysRevLett.96.047212.

[153] N. Saratz, U. Ramsperger, A. Vindigni, and D. Pescia, "Irreversibility, reversibility, and thermal equilibrium in domain patterns of Fe films with perpendicular magnetization," *Physical Review B,* vol. 82, no. 18, 2010, doi: 10.1103/PhysRevB.82.184416.

[154] J. Liu, G. Y. Tian, B. Gao, K. Zeng, Y. Zheng, and J. Chen, "Micro-macro characteristics between domain wall motion and magnetic Barkhausen noise under tensile stress," *Journal of Magnetism and Magnetic Materials,* vol. 493, 2020, doi: 10.1016/j.jmmm.2019.165719.

[155] K.-i. Uchida, H. Adachi, T. Ota, H. Nakayama, S. Maekawa, and E. Saitoh, "Observation of longitudinal spin-Seebeck effect in magnetic insulators," *Applied Physics Letters,* vol. 97, no. 17, 2010, doi: 10.1063/1.3507386.

[156] K. Uchida *et al.*, "Phenomenological analysis for spin-Seebeck effect in metallic magnets," *Journal of Applied Physics,* vol. 105, no. 7, 2009, doi: 10.1063/1.3056581.

[157] C. M. Jaworski, J. Yang, S. Mack, D. D. Awschalom, J. P. Heremans, and R. C. Myers, "Observation of the spin-Seebeck effect in a ferromagnetic semiconductor," *Nat Mater,* vol. 9, no. 11, pp. 898-903, Nov 2010, doi: 10.1038/nmat2860.

[158] X. Zheng *et al.*, "Paradigm of Magnetic Domain Wall-Based In-Memory Computing," *ACS Applied Electronic Materials,* vol. 2, no. 8, pp. 2375-2382, 2020, doi: 10.1021/acsaelm.0c00318.

[159] S. M. Ahn, K. W. Moon, C. G. Cho, and S. B. Choe, "Control of domain wall pinning in ferromagnetic nanowires by magnetic stray fields," *Nanotechnology,* vol. 22, no. 8, p. 085201, Feb 25 2011, doi: 10.1088/0957-4484/22/8/085201.

[160] S. Lepadatu, A. Vanhaverbeke, D. Atkinson, R. Allenspach, and C. H. Marrows, "Dependence of domain-wall depinning threshold current on pinning profile," *Phys Rev Lett,* vol. 102, no. 12, p. 127203, Mar 27 2009, doi: 10.1103/PhysRevLett.102.127203.

[161] L. Berger, "Analysis of measured transport properties of domain walls in magnetic nanowires and films," *Physical Review B,* vol. 73, no. 1, pp. 014407-1-5, 2006, doi: 10.1103/PhysRevB.73.014407.

[162] D. Atkinson, D. S. Eastwood, and L. K. Bogart, "Controlling domain wall pinning in planar nanowires by selecting domain wall type and its application in a memory concept," *Applied Physics Letters,* vol. 92, no. 2, pp. 022510-1-3, 2008, doi: 10.1063/1.2832771.

[163] R. Schafer, "Investigation of Domains and Dynamics of Domain Walls by the Magneto-optical Kerr-effect," pp. 1-29, 2007.

[164] M. Hayashi, L. Thomas, C. Rettner, R. Moriya, and S. S. P. Parkin, "Direct observation of the coherent precession of magnetic domain walls propagating along permalloy nanowires,"

Nature Physics, vol. 3, no. 1, pp. 21-25, 2006, doi: 10.1038/nphys464.

[165] M. Hayashi *et al.*, "Influence of current on field-driven domain wall motion in permalloy nanowires from time resolved measurements of anisotropic magnetoresistance," *Phys Rev Lett,* vol. 96, no. 19, pp. 197207-1-4, May 19 2006, doi: 10.1103/PhysRevLett.96.197207.

[166] H. Awano, "Investigation of domain wall motion in RE-TM magnetic wire towards a current driven memory and logic," *Journal of Magnetism and Magnetic Materials,* vol. 383, pp. 50-55, 2015, doi: 10.1016/j.jmmm.2014.12.081.

[167] Y. Wang *et al.*, "Magnetization switching by magnon-mediated spin torque through an antiferromagnetic insulator," *Science,* pp. 1125-1128, 2019.

[168] X. Zhang, M. Ezawa, and Y. Zhou, "Magnetic skyrmion logic gates: conversion, duplication and merging of skyrmions," *Sci Rep,* vol. 5, p. 9400, Mar 24 2015, doi: 10.1038/srep09400.

[169] M. A. Zidan, J. P. Strachan, and W. D. Lu, "The future of electronics based on memristive systems," *Nature Electronics,* vol. 1, no. 1, pp. 22-29, 2018, doi: 10.1038/s41928-017-0006-8.